NASA/TP-1999-209093

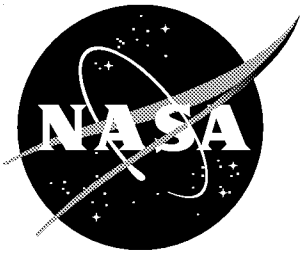

Effects of Convoluted Divergent Flap Contouring on the Performance of a Fixed-Geometry Nonaxisymmetric Exhaust Nozzle

Scott C. Asbury and Craig A. Hunter
Langley Research Center, Hampton, Virginia

February 1999

The NASA STI Program Office ... in Profile

Since its founding, NASA has been dedicated to the advancement of aeronautics and space science. The NASA Scientific and Technical Information (STI) Program Office plays a key part in helping NASA maintain this important role.

The NASA STI Program Office is operated by Langley Research Center, the lead center for NASA's scientific and technical information. The NASA STI Program Office provides access to the NASA STI Database, the largest collection of aeronautical and space science STI in the world. The Program Office is also NASA's institutional mechanism for disseminating the results of its research and development activities. These results are published by NASA in the NASA STI Report Series, which includes the following report types:

- TECHNICAL PUBLICATION. Reports of completed research or a major significant phase of research that present the results of NASA programs and include extensive data or theoretical analysis. Includes compilations of significant scientific and technical data and information deemed to be of continuing reference value. NASA counterpart of peer-reviewed formal professional papers, but having less stringent limitations on manuscript length and extent of graphic presentations.

- TECHNICAL MEMORANDUM. Scientific and technical findings that are preliminary or of specialized interest, e.g., quick release reports, working papers, and bibliographies that contain minimal annotation. Does not contain extensive analysis.

- CONTRACTOR REPORT. Scientific and technical findings by NASA-sponsored contractors and grantees.

- CONFERENCE PUBLICATION. Collected papers from scientific and technical conferences, symposia, seminars, or other meetings sponsored or co-sponsored by NASA.

- SPECIAL PUBLICATION. Scientific, technical, or historical information from NASA programs, projects, and missions, often concerned with subjects having substantial public interest.

- TECHNICAL TRANSLATION. English-language translations of foreign scientific and technical material pertinent to NASA's mission.

Specialized services that complement the STI Program Office's diverse offerings include creating custom thesauri, building customized databases, organizing and publishing research results ... even providing videos.

For more information about the NASA STI Program Office, see the following:

- Access the NASA STI Program Home Page at *http://www.sti.nasa.gov*

- E-mail your question via the Internet to help@sti.nasa.gov

- Fax your question to the NASA STI Help Desk at (301) 621-0134

- Phone the NASA STI Help Desk at (301) 621-0390

- Write to:
  NASA STI Help Desk
  NASA Center for AeroSpace Information
  7121 Standard Drive
  Hanover, MD 21076-1320

NASA/TP-1999-209093

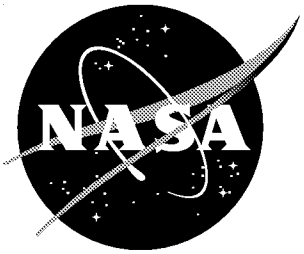

Effects of Convoluted Divergent Flap Contouring on the Performance of a Fixed-Geometry Nonaxisymmetric Exhaust Nozzle

Scott C. Asbury and Craig A. Hunter
Langley Research Center, Hampton, Virginia

National Aeronautics and
Space Administration

Langley Research Center
Hampton, Virginia 23681-2199

February 1999

Available from:

NASA Center for AeroSpace Information (CASI)
7121 Standard Drive
Hanover, MD 21076-1320
(301) 621-0390

National Technical Information Service (NTIS)
5285 Port Royal Road
Springfield, VA 22161-2171
(703) 605-6000

Summary

An investigation was conducted in the model preparation area of the Langley 16-Foot Transonic Tunnel to determine the effects of convoluted divergent-flap contouring on the internal performance of a fixed-geometry exhaust nozzle. Testing was conducted at static conditions using a sub-scale, nonaxisymmetric, convergent-divergent nozzle model designed with interchangeable divergent flap inserts. Force, moment, and pressure measurements were taken and internal focusing schlieren flow visualization was obtained for one baseline and four convoluted configurations. All tests were conducted with no external flow at nozzle pressure ratios from 1.25 to approximately 9.50.

Results indicate that baseline nozzle performance was dominated by unstable, shock-induced, boundary-layer separation at overexpanded (below the design nozzle pressure ratio) conditions, which came about through the natural tendency of overexpanded exhaust flow to satisfy conservation requirements by detaching from the nozzle divergent flaps. Convoluted configurations were found to significantly reduce, and in some cases totally alleviate, shock-induced, boundary-layer separation at overexpanded conditions. This result was attributed to the ability of convoluted contouring to energize and improve the condition of the nozzle boundary layer. Separation alleviation resulted in off-design nozzle thrust ratio penalties that ranged from 3.6% to 6.4% below the fully separated baseline configuration; thus, imposing a tradeoff between separation alleviation and nozzle thrust ratio which may be acceptable in some applications. Separation alleviation offers potential for installed nozzle aeropropulsive (thrust-minus-drag) performance benefits by reducing drag at forward flight speeds, even though this may reduce nozzle thrust ratio at off-design conditions. At on-design conditions, nozzle thrust ratio for the convoluted configurations ranged from 1% to 2.9% below the baseline configuration; this was a result of increased skin friction and oblique shock losses inside the nozzle.

Introduction

Supersonic cruise transport aircraft and modern military aircraft with supersonic cruise or dash capabilities utilize variable-geometry exhaust nozzles to ensure efficient aeropropulsive (thrust-minus-drag) performance across a wide speed range. A variable-geometry nozzle functions by adjusting throat area and expansion ratio to provide the optimum nozzle configuration for each engine throttle setting and flight condition. Independent throat area (A_t) control is necessary to satisfy engine afterburning requirements, and separate control of the exit area (A_e) provides the proper nozzle expansion ratio (A_e/A_t) at each flight condition (ref. 1). For example, a typical fighter aircraft might have a low nozzle pressure ratio of about 3.0 at takeoff, requiring a nozzle expansion ratio of about 1.1 for optimum nozzle performance. During a supersonic dash to Mach 2.0, nozzle pressure ratio increases to approximately 10.0, and a nozzle expansion ratio of 1.9 is required for optimum nozzle performance. Figure 1 illustrates a typical variable-geometry nozzle at several operating conditions.

Nozzle geometry variation is achieved using actuators and movable nozzle flaps as shown in figure 2. While effective, these systems can be heavy, mechanically complex, and prone to fatigue through thermal, aerodynamic, and aeroacoustic loading. In addition, variable-geometry mechanisms are inherently difficult to integrate into fighter aircraft afterbodies and can be a primary cause of afterbody drag. Additional requirements such as multiaxis thrust vectoring (ref. 2), thrust reversing (ref. 3), low observability (ref. 4), and noise suppression (ref. 5) further complicate the propulsion-airframe integration of variable-geometry nozzle systems.

The capabilities of future high performance military aircraft will be critically dependent on the development of simple, lightweight exhaust systems that are aerodynamically efficient, compact, and low observable. Supersonic transport aircraft will rely heavily on efficient nozzle performance for extended cruise at high

supersonic speeds where the ratio of lift to drag is low and fuel consumption is high. There is tremendous incentive to improve both military and transport aircraft performance by reducing the complexity of exhaust nozzles.

The desire for reduced weight and complexity in exhaust systems has led designers to consider reducing, or even eliminating, the need for variable-geometry mechanisms in exhaust nozzles. The fundamental problem with this solution is that a fixed-geometry nozzle will only operate efficiently at the flight condition for which it is designed. When operated away from the design point (which may be common if a supersonic aircraft is expected to cruise subsonically, loiter, or divert to alternate airports), a fixed-geometry nozzle suffers large off-design performance penalties. For example, if the fighter aircraft mentioned previously were to operate with a fixed-geometry, 1.9 expansion ratio nozzle at the takeoff condition, a 20-percent loss in thrust ratio would result from nozzle overexpansion effects (ref. 1). Large performance penalties such as this would be unacceptable in most applications.

The successful utilization of fixed-geometry nozzles in most aircraft applications will require improvements in off-design performance. At highly overexpanded conditions, exhaust flow separation results from the natural tendency of overexpanded exhaust flow to satisfy conservation requirements by separating from the nozzle divergent flaps. This increases off-design performance by allowing the nozzle to effectively "adjust" to a shorter nozzle with a lower expansion ratio. At forward flight speeds, however, external flow can aspirate the separated portion of the divergent flaps, causing increased drag (ref. 6). In some instances, separation alleviation may be necessary to ensure efficient aeropropulsive performance, even if losses in thrust ratio result from increased exhaust flow overexpansion. A detailed study would be required to determine the conditions at which separation alleviation is beneficial to nozzle aeropropulsive performance.

Numerous research programs have shown that three-dimensional convoluted contouring can enhance multistream mixing and reduce subsonic boundary-layer separation in various applications (refs. 7 through 10). The objective of the research described in this report was to determine the effects of convoluted divergent-flap contouring on the internal performance of a fixed-geometry exhaust nozzle. Testing was conducted at static conditions in the model preparation area of the Langley 16-Foot Transonic Tunnel using a sub-scale, nonaxisymmetric, convergent-divergent nozzle model designed with interchangeable divergent flap inserts. The nozzle model had an expansion ratio of 1.797 and a design nozzle pressure ratio of 8.78. Force, moment, and pressure measurements were taken and internal focusing schlieren flow visualization was obtained for one baseline and four convoluted configurations. All tests were conducted with no external flow and high-pressure air was used to simulate jet-exhaust flow at nozzle pressure ratios ranging from 1.25 to approximately 9.50.

Symbols

All forces and moments are referred to the model centerline (body axis). The model (balance) moment reference center was located at station 29.39. A discussion of the data reduction procedure, definitions of force and moment terms and propulsion relationships used herein can be found in reference 11. All pressures presented are absolute unless otherwise noted.

A_e	nozzle exit area, 7.758 in^2
A_t	nozzle throat area, 4.317 in^2
F	measured thrust along body axis, positive in forward direction, lbf
F_i	ideal isentropic thrust, lbf
F/F_i	nozzle thrust ratio
$(F/F_i)_{peak}$	peak nozzle thrust ratio

g	acceleration due to gravity, 32.174 ft/sec^2
M	Mach number
NPR	nozzle pressure ratio, p_{t_j}/p_a
NPR_d	design nozzle pressure ratio (NPR for fully expanded flow at the nozzle exit)
p	local static pressure, psi
p_a	ambient pressure, psi
p_{t_j}	average jet-total pressure, psi
R_j	gas constant (for γ=1.3997), 1716 ft^2/sec^2-°R
T_{t_j}	average jet-total temperature, °R
w_p	measured weight-flow rate, lbf/sec
x	linear dimension measured along model centerline from nozzle connect station (Sta. 41.13), positive downstream (see figs. 8, 9, and 13), in.
x_t	distance between nozzle connect station (Sta. 41.13) and nozzle throat, measured along model centerline, positive downstream (see fig. 13), 2.275 in.
y	vertical distance measured from model centerline, positive upwards (see figs. 8 and 9), in.
z	lateral distance measured from model centerline, positive to right when looking upstream (see figs. 8 and 13), in.
$\Delta(F/F_i)_f$	skin friction thrust ratio penalty
α	nozzle divergence half angle, 11.01 deg
β	oblique shock-wave inclination angle, measured from upstream flow direction, deg
γ	ratio of specific heats, 1.3997 for air
θ	angle of flow direction across an oblique shock wave, measured from upstream flow direction, deg

Subscripts:

1	conditions just upstream of a shock wave
2	conditions just downstream of a shock wave

Abbreviations:

C-D	convergent-divergent
Hz	Hertz
NPAC	Nozzle Performance Analysis Code
R	radius, in.
Sta.	model station, in.

Apparatus and Procedures

Test Facility

This investigation was conducted in the model preparation area of the Langley 16-Foot Transonic Tunnel. Although this facility is normally used for setup and calibration of wind-tunnel models, it can also be used for nozzle internal performance testing at static (no external flow) conditions. Testing is conducted in a 10 x 29-foot chamber where a cold-flow ($T_{t_j} \approx 540$°R) jet from a single-engine propulsion simulation system exhausts to the atmosphere through an acoustically treated exhaust passage. A control room is adjacent to the test chamber, and offers access through a sound-proof door and observation window. The model preparation area shares a high-pressure air system with the 16-Foot Transonic Tunnel that includes valving, filters, and a heat exchanger to provide a continuous flow of clean, dry air to the propulsion simulation

system for jet-exhaust simulation. A complete description of the test facility is provided in reference 12.

Single-Engine Propulsion Simulation System

The single-engine propulsion simulation system used in this investigation is shown in detail in figure 3. High-pressure air supplied to the propulsion simulation system was varied from atmosphere up to about 140 psi total pressure in the instrumentation section at a constant stagnation temperature of approximately 540°R. As shown in figure 3(b), the high-pressure air was delivered by six air lines through a support strut into a annular high-pressure plenum. The air was then discharged radially into a low-pressure plenum through eight equally spaced, multiholed sonic nozzles. This flow transfer system was designed to minimize any forces imposed by the transfer of axial momentum as the air passed from the non-metric high-pressure plenum to the metric (attached to the balance) low-pressure plenum. Two flexible metal bellows functioned as seals between the non-metric and metric portions of the model and compensated for axial forces caused by pressurization. The air then passed through a circular-to-rectangular transition section, a rectangular choke plate (primarily used for flow straightening), a rectangular instrumentation section, and then through the nozzle, which exhausted to atmospheric back pressure. The instrumentation section had a ratio of flow path width to height of 1.437 and was identical in geometry to the nozzle airflow entrance (nozzle connect station). All nozzle configurations tested were attached to the downstream end of instrumentation section at model station 41.13.

Nozzle Concept

A fixed-geometry, nonaxisymmetric, C-D nozzle was designed with symmetric pairs (upper and lower) of convergent and divergent flaps and flat (internally) sidewalls to contain the exhaust flow in the lateral direction. The nozzle was based on a previous design described in reference 13. In an effort to improve off-design performance, the nozzle divergent flap surfaces were modified with three-dimensional convoluted contouring.

Convoluted contouring. Numerous research programs have shown that three-dimensional convoluted contouring can enhance multistream mixing and reduce subsonic boundary-layer separation in various applications (refs. 7 through 10). The most familiar application of convoluted contouring is the turbofan forced mixer shown in figure 4, which efficiently mixes engine-core and fan exhaust flow in mixed-flow, long-duct, turbofan nacelles by generating streamwise vorticity as shown in figure 5 (ref. 14). In addition, convoluted contouring has proven successful in alleviating boundary-layer separation on fighter aircraft afterbodies (ref. 9) and airfoil trailing edges (ref. 7). Part of this separation alleviation is due to energization of the boundary layer from vorticity generated by the convoluted contours, but research has shown that the contouring can also delay separation in the convoluted section itself (refs. 7 to 10).

The "bump" type convoluted contouring used in this investigation is depicted in figure 6. This contouring generates multi-dimensional pressure gradients and inviscid secondary flows in a normally two-dimensional onset flow, providing three-dimensional relief for the onset boundary layer as it approaches an adverse pressure gradient. As boundary-layer flow nears the convolutions, it receives additional freedom of movement in the lateral direction, which reduces the tendency for two-dimensional separation to occur. In addition, the convolutions generate secondary flows in the form of horseshoe vortices due to the inviscid turning and stretching of vortex filaments as they pass over the contours. These vortical secondary flows can trail downstream 5 to 10 convolution heights before breaking down, continuously energizing the boundary layer in that region (ref. 9).

Nozzle Models

The model used in this investigation was a sub-scale, nonaxisymmetric, C-D nozzle with an

expansion ratio A_e/A_t of 1.797 (NPR_d=8.78), a nominal throat area A_t of 4.317 in^2, and a constant flow path width of 3.990 in. The model was composed of upper and lower nozzle flap assemblies, (each equipped with interchangeable divergent flap inserts) and two sidewall assemblies (each equipped with optical quality boro-silicate crown glass windows to permit internal focusing schlieren flow visualization). A photograph, sketch, and geometric details of the nozzle model with baseline (no convolutions) divergent flap inserts installed are presented in figures 7, 8, and 9, respectively. The four convoluted geometries investigated consisted of a fine configuration (fig. 10(a)), a medium configuration (fig. 10(b)), a medium-long configuration (fig. 10(c)), and a coarse configuration (fig. 10(d)). Photographs of the convoluted flap insert pairs and a typical convoluted nozzle configuration are presented in figures 11 and 12, respectively.

Design of the convoluted configurations was based on guidance from prior research (refs. 7 to 10). Convolution length-to-height scaling was varied by testing aggressive contours, in which the convolution rose to its maximum amplitude in a short distance (0.5 in. for the fine, medium, and coarse convoluted configurations), and a more gentle contour, in which the convolution rose to its maximum amplitude over a longer distance (0.875 in. for the medium-long convoluted configuration). The fine, medium, and coarse convoluted configurations had approximately the same wetted area, while their geometry varied in maximum amplitude. Engineering judgment was used to pick a maximum amplitude of 0.0998 inches for the medium convoluted configuration; the fine and coarse convoluted configurations had maximum amplitudes that were one half and twice that of the medium convoluted configuration, respectively. All convoluted contours had parallel lobe walls, a lobe height to width aspect ratio of 2.0, and semi-circular lobe hills and valleys. Longitudinal and streamwise convolution profiles were composed of symmetric, tangent arcs such that the convolutions rose from zero height to their maximum amplitude in a smooth, continuous fashion. The length of the convoluted run was 1.00 inch for the fine, medium, and coarse convoluted configurations and 1.75 inches for the medium-long convoluted configuration.

Instrumentation

Weight-flow rate of high-pressure air supplied to the nozzle was calculated from pressures and temperatures measured in a calibrated multiple-critical venturi system located upstream of the propulsion simulation system. This venturi system is the same airflow-measurement system used in the 16-Foot Transonic Tunnel, and is rated to be 99.9% accurate in weight-flow measurements. Forces and moments were measured by a six-component strain-gauge balance located on the centerline of the propulsion simulation system. Jet total pressure was measured at a fixed station in the instrumentation section with a four-probe rake through the upper surface and a three-probe rake through the corner as shown in figure 3(b). Two iron-constantan thermocouples in the instrumentation section measured jet total temperature.

Static pressures were measured inside the nozzle for each configuration using 0.020-inch diameter static pressure orifices as shown in figure 13. There were six static pressure orifices in the nozzle convergent section and one orifice at the geometric throat (fig. 13(a)), located on the nozzle centerline (z=0.000 in.). The flap inserts were equipped with a row of centerline and sideline (0.400 inches from the sidewall) pressure orifices, each containing 21 static pressure orifices spaced 0.100 inches apart. Unique to the convoluted configurations was an row of ten static pressure orifices in the lobe valley (z=0.1995 in.), adjacent to the centerline lobe hill, that were added to determine multi-dimensional effects of the convolutions.

Individual pressure transducers were used to measure pressures in the air supply system, multiple-critical venturi, instrumentation section, and nozzle convergent section. The transducers were selected and sized to allow the highest accuracy over each required measurement range.

Divergent flap pressures were measured by two electronically scanning pressure modules located in the model preparation area test chamber in an acoustically shielded cabinet.

Data Reduction

Each data point is the average steady-state value computed from 50 frames of data taken at a rate of 10 frames per second. All data were taken with ascending NPR. A detailed description of the procedures used for data reduction in this investigation can be found in reference 11.

Balance corrections. Each of the six measured balance components were initially corrected for model weight tares and isolated balance component interactions. Although the bellows arrangement in the air pressurization system was designed to minimize forces on the balance caused by pressurization, small bellows tares on the six-component balance still existed. These tares resulted from small pressure differences between the ends of the bellows when air system internal velocities were high and from small differences in the spring constant of the forward and aft bellows when the bellows were pressurized. Bellows tares were determined by testing Stratford choke calibration nozzles with known performance over a range of expected internal pressure and external forces and moments. The resulting tares were then applied to the six-component balance data to obtain corrected balance measurements. Balance axial force obtained in this manner is a direct measurement of the nozzle thrust along the body axis, F. The procedure used for computing bellows tares is discussed in detail in reference 15.

Calculations. Jet total pressure was measured from four center rake and three corner rake total pressure probes located in the instrumentation section. Nozzle pressure ratio (NPR) is the average jet total pressure $p_{t,j}$ measured in the instrumentation section divided by ambient pressure p_a; NPR was varied in this investigation from 1.25 to approximately 9.50. Jet total temperature $T_{t,j}$ was obtained from two total temperature probes located in the instrumentation section. The average jet total pressure and jet total temperature are computed as the arithmetic mean of the individual measurements.

Nozzle thrust ratio F/F_i is the ratio of measured thrust along the body axis F to the computed ideal isentropic thrust F. The measured weight-flow rate w_p, which is determined by using a multiple-critical venturi system, is used to determine ideal isentropic thrust from the following equation:

$$F_i = w_p \sqrt{\frac{R_j T_{t,j}}{g^2} \frac{2\gamma}{\gamma - 1} \left[1 - \left(\frac{1}{\mathrm{NPR}} \right)^{(\gamma-1)/\gamma} \right]}$$

Uncertainty Analysis

An uncertainty analysis of the results presented was performed based on a propagation of bias uncertainties of actual measurements through the data reduction equations. This analysis assumes that bias errors are dominant over precision errors and is based on the method presented in reference 16. This method uses the first order terms in a Taylor series expansion of the data reduction equations to estimate the uncertainty contributions of each measurement. With this technique, the contribution of each measurement would be the measurement uncertainty multiplied by the derivative of the data reduction equation with respect to that measurement. The total uncertainty of the final calculated result is estimated as the root-sum-square of the individual contributions with 95-percent confidence.

The analysis accounted for the uncertainties of the following measurements: jet total pressure, jet total temperature, atmospheric pressure, venturi weight-flow rate, and balance axial force. The analysis also accounted for the beneficial effect of averaging multiple measurements of the same quantity, such as the total pressure in the instrumentation section. This type of analysis is typical of that used for experimental static test programs and is credited to the work presented in reference 17.

The results of the analysis for the range of test conditions indicate that the uncertainty of NPR and p/p_{t_j} is approximately ±0.28 percent of measured value. The uncertainty of F/F_i is approximately ±0.004 and is essentially independent of NPR.

Focusing Schlieren Flow Visualization

A focusing schlieren flow visualization system was used during this investigation to visualize the nozzle internal (through glass sidewalls) and external exhaust flowfield. An optical description and schematic layout of the focusing schlieren system are presented in figure 14. The system was designed and built based on criterion reported in reference 18. The system is characterized by a 133 mm diameter field of view, a sensitivity of 17 arcsec, a resolution of 0.25 mm, a depth of sharp focus of 4.6 mm, and a depth of unsharp focus of 36 mm. The image was focused on the centerline of the nozzle.

The light source for the focusing schlieren system was a xenon strobe flash tube. A driving circuit picked up sync pulses generated by the recording video camera and triggered the flash at a 30 Hz rate with pulses of 0.6 µsec duration and 0.05 watt-sec power. A 720 x 480 pixel resolution color video camera and a 70 mm still camera recorded results.

The focusing schlieren system was assembled on a 44 x 66 inch table that mounted on a rigid platform equipped with casters and leveling screws. The platform was placed under the propulsion simulation system and jacked and leveled to the appropriate position. Flow visualization data were recorded simultaneously with other data acquisition.

Presentation of Results

Nozzle thrust ratio F/F_i and internal static pressure ratio p/p_{t_j} data for all nozzle configurations tested are tabulated in table 1 and tables 2 to 6, respectively. During the discussion of results, comparisons of nozzle thrust ratio F/F_i are made in terms of percentage change from ideal (F/F_i=1) isentropic conditions. Graphical presentation of basic and summary data are presented in figures 15 to 30.

Results and Discussion

On-Design Performance

Baseline configuration. Nozzle thrust ratio F/F_i performance for the baseline configuration is presented as a function of nozzle pressure ratio (NPR) in figure 15. Peak thrust ratio $(F/F_i)_{peak}$ for the baseline configuration is approximately 0.986 at the on-design condition (NPR_d=8.78), which is within the 0.985 to 0.990 range consistent with previous studies of nonaxisymmetric convergent-divergent nozzles (refs. 19 to 21). The approximate 1.4% loss in peak thrust ratio from ideal isentropic conditions at NPR_d can be attributed to exit flow angularity effects and friction drag inside the nozzle (ref. 22).

Convoluted configurations. When an exhaust nozzle is operating at the on-design condition, it is internally shock free, the flow is fully expanded, and peak thrust efficiency is produced. Therefore, the presence of convoluted contours in the divergent section of the nozzle would likely result in on-design performance penalties. Because convolutions would probably be present at all operating conditions, on-design performance penalties associated with the convoluted geometry must be minimized to ensure that the benefits of having the convolutions at off-design conditions are not outweighed by any on-design performance penalties.

Nozzle thrust ratio performance for baseline and convoluted configurations is presented as a function of NPR in figure 16. All convoluted configurations had $(F/F_i)_{peak}$ at NPR_d that were lower than the baseline value. This result is summarized in table 7. Losses in $(F/F_i)_{peak}$ due to the convolutions were 1% or less for the fine, medium, and medium-long convoluted configurations. The coarse convoluted configuration had a significantly larger 2.9% loss in $(F/F_i)_{peak}$ as a result of its more aggressive

convoluted geometry.

The convoluted configurations had a significant increase in wetted area over that of the baseline configuration. Consequently, increased skin friction losses were expected to impart a thrust ratio penalty. After calculating wetted area for each configuration, skin friction drag penalties $\Delta(F/F_i)_f$ were estimated and $(F/F_i)_{peak}$ values were predicted using the baseline nozzle pressure gradient as input to the nozzle internal performance prediction package NPAC described in reference 22. The results are summarized in table 8.

The increase in wetted area was 15% for the fine, medium, and coarse convoluted configurations and 26% for the medium-long convoluted configuration. Using NPAC, a skin friction drag penalty of 0.2% was estimated and peak thrust ratio of 0.984 was predicted for the coarse, medium, and fine convoluted configurations. A slightly higher skin friction drag penalty of 0.3% and slightly lower peak thrust ratio of 0.983 was predicted for the medium-long convoluted configuration. A comparison of NPAC predicted and experimentally measured peak thrust ratios for baseline and convoluted configurations is presented in figure 17. The fine and medium-long convoluted configurations had the highest thrust ratio performance of the convoluted configurations, which at $(F/F_i)_{peak}$=0.980, was only 0.6% lower than the baseline value. The medium and coarse convoluted configurations had peak thrust ratio performance that was 1.0% and 3.1% lower than the baseline value, respectively. Note that the medium-long convoluted configuration, with 11% more wetted area than the other convoluted configurations, had a higher $(F/F_i)_{peak}$ than the medium convoluted configuration. This result suggests that on-design thrust ratio penalties for convoluted configurations are only partially attributable to increased wetted area; e.g., they are related to some other phenomena as well.

Flow visualization at NPR=8.9, presented for baseline and convoluted configurations in figure 18, shows that the convoluted configurations generated intense supersonic wave radiation that coalesced into oblique shocks at certain points in the nozzle. The presence of oblique shocks reduces jet momentum in the nozzle, which explains the additional peak thrust ratio penalties imposed by the convolutions. The medium-long convoluted configuration (fig. 18(d)) appears to have generated less supersonic wave radiation than the other convoluted configurations, explaining the aforementioned lower losses in $(F/F_i)_{peak}$ for this configuration.

A comparison of baseline and convoluted internal static pressure ratio distributions (plotted against nondimensionalized streamwise location relative to the nozzle throat x/x_t) is presented in figure 19 at NPR=8.9. In each convoluted configuration, pressures upstream and downstream of the convolution run were not greatly affected by the convolutions. Flow over the fine (fig. 19(a)) and medium-long (fig. 19(c)) convolution runs was characterized by weak compressions (locally increasing p/p_{t_j}) at the leading and trailing edges of the convolution hill and a stronger compression midway in the convolution valley. Similar behavior occurred for the medium (fig. 19(b)) and coarse (fig. 19(d)) convoluted configurations except that compressions were much stronger and were separated by regions of rapid expansion (locally decreasing p/p_{t_j}) for these configurations. This behavior may help explain why the medium convoluted configuration had stronger supersonic wave radiation and a lower $(F/F_i)_{peak}$ than the medium-long convoluted configuration. Like the coarse convoluted configuration, the medium convoluted configuration presented a much more aggressive streamwise convolution geometry than the medium-long or fine convoluted configurations, such that the flow had to turn more abruptly through the convolutions and a stronger compression/expansion mechanism was necessary. The convolution hill for the coarse convoluted configuration was aggressive enough to generate a strong shock (noted by a rapid compression) at the start of the convolution run, which explains the severe drop in $(F/F_i)_{peak}$ measured for that configuration.

Off-Design Performance

Baseline configuration. As shown in figure 15, nozzle thrust ratio decreased as NPR decreased below NPR_d; a result of exhaust flow overexpansion effects. Internal static pressure ratio distributions for the baseline configuration, presented in figure 20, are typical of convergent-divergent nozzle flow characteristics (ref. 23). For centerline pressures (z=0.00 in.), the first two curves at a NPR of 1.26 and 1.4 indicate choked ($p/p_{t,j} \leq 0.528$), internally overexpanded flow with a weak shock (noted by the significant increase in $p/p_{t,j}$ with x/x_t) present near the nozzle geometric throat (x/x_t=1.00). Flow downstream of the shock was subsonic ($p/p_{t,j} > 0.528$), remained attached to the divergent flap wall, and recovered to ambient pressure ($p/p_{t,j}$=1/NPR) in a smooth, continuous fashion. Flow visualization for the baseline configuration is shown in figure 21. At NPR=1.4 (fig. 21(a)), there was a weak, almost normal shock downstream of the throat with little or no lambda foot structure evident. This behavior is characteristic of a weak shock, with a flow Mach number of approximately 1.2 just upstream of the shock (M_1), and a thin boundary layer inside the nozzle. Flow Mach number inside the nozzle was estimated from $p/p_{t,j}$ values using tables for compressible flow in reference 24.

As shown in figure 20, the discontinuous nature of the centerline pressure distribution at NPR=1.6 indicates that shock strength increased ($M_1 \approx 1.4$), and the inflection point in the pressure recovery downstream of the shock at $x/x_t \approx 1.28$ indicates that flow separation occurred on the divergent flaps, though it was not severe. The pressure distribution also indicates that the flow became subsonic downstream of $x/x_t \approx 1.55$ and flow reattachment to the flap is indicated by the smooth pressure recovery downstream of this point. By NPR=1.8, the upstream shock Mach number was $M_1 \approx 1.5$ and shock-induced, boundary-layer separation began to dominate nozzle flow characteristics. At NPR=1.8, there are strong signs of a separation bubble, with minimal pressure recovery indicated by a relatively flat pressure distribution from the shock location at $x/x_t \approx 1.35$ out to $x/x_t \approx 1.7$; however, full recovery to ambient pressure occurred over the remaining length of the nozzle. Flow visualization at NPR=1.8 in figure 21(b) shows the shock with a small lambda foot structure. The flow was also highly unstable; this phenomena was observed in the schlieren video recorded during the test and is indicated by the schlieren photograph, which captured an image of the shock in two positions over a 0.6 μsec duration. Because the image was focused on the centerline of the nozzle with a depth of sharp focus of 4.6 mm, the dual-shock nature of this photo should not be attributed to an alignment problem.

An increase in pressure ratio to NPR=2.0 did not significantly change shock location or strength, but did result in fully detached shock-induced separation with almost no pressure recovery downstream of the shock (fig. 20). Flow visualization at NPR=2.0 in figure 21(c) shows the shock with a pronounced lambda foot structure and a large separation region extending from the leading lambda foot downstream past the nozzle exit. The results discussed above indicate that the nozzle flow adjusted to exit conditions at NPR=2.0 simply by detaching from the divergent flaps, while normalized pressure (and thus Mach number) upstream of the shock matched those of the previous NPR. This behavior indicates that the onset of fully detached flow separation at NPR=2.0 was not the result of a stronger shock-boundary layer interaction, but instead came about through the natural tendency of overexpanded exhaust flow in a fixed-geometry nozzle to conserve mass, momentum, and energy by detaching from the divergent flaps and "adjusting" to an effectively shorter nozzle with a lower expansion ratio.

As shown in figure 15, the onset of fully-detached, shock-induced, boundary-layer separation at NPR=2.0 corresponds to a marked increase in nozzle thrust ratio. By providing an effectively lower nozzle expansion ratio, internal flow separation reduced overexpansion losses in the nozzle and increased nozzle thrust ratio. It should be noted that this beneficial effect may not exist at forward speeds where external flow could aspirate the separated portion of the divergent

flaps, causing increased drag. As a result, the ability to alleviate separation inside a fixed-geometry nozzle may be beneficial to overall aeropropulsive performance at forward speeds, even if small losses in nozzle thrust ratio occur as a result of the separation alleviation process. The information required to make the tradeoff between allowing separation to occur or alleviating separation is beyond the scope of this investigation.

As shown in figure 20, fully-detached flow separation occurred for all subsequent internally overexpanded NPRs above 2.0. As NPR was increased beyond 2.0, the leading lambda foot progressed downstream in the nozzle. Figure 21(d) shows the shock at NPR=2.4 with a well defined lambda foot structure and fully detached flow separation. By NPR=3.4 (fig. 21(e)), the lambda foot structure had grown significantly, such that the main shock and trailing lambda foot were outside the nozzle. At this NPR, flow inside the nozzle past the separation point showed strong resemblance to externally overexpanded exhaust flow; the jet plume necked down from the separation point at the leading lambda foot to the trailing lambda foot, and there was an expansion fan emanating from each trailing lambda foot. This behavior indicates that the separation point was behaving as if it were at the nozzle exit, and flow past this point was externally overexpanded. Static pressure ratio distributions in figure 20 indicate that the shock was positioned near the nozzle exit by NPR=5.0 and that the nozzle was shock free by NPR=5.4. At NPR≥5.4, all pressure distributions fell on the same curve, indicating that nozzle internal flow characteristics were independent of NPR beyond that point.

A comparison of sideline (z=1.595 in.) to centerline (z=0.000 in.) internal static pressure ratio distributions in figure 20 indicates noticeable differences below NPR=2.4. Differences between sideline and centerline pressure distributions in both shock location and pressure recovery past the shock indicate that flow inside the nozzle was three-dimensional and that the shock was non-planar. Sideline data at NPR of 1.26 and 1.4 show fully-detached flow separation and a shock location upstream of its centerline position. Sideline pressures near the nozzle exit are lower than centerline pressures, indicating that sideline flow was recompressing downstream of the nozzle exit.

Convoluted configurations. Individual comparisons of nozzle thrust ratio between baseline and convoluted configurations are presented in figure 22. At very low NPRs, the convoluted configurations exhibited performance characteristics that were similar to the baseline configuration. Static pressure ratio distributions presented for each convoluted configuration in figure 23 show overexpanded and separated flow at NPRs up to 2.0 in the fine convoluted configuration (fig. 23(a)), 1.8 in the medium convoluted configuration (fig. 23(b)), and 1.6 in the medium-long (fig. 23(c)) and coarse convoluted configurations (fig. 23(d)). Flow visualization at these NPRs, presented in figure 24, show various degrees of separation for each configuration. For all NPRs equal to or lower than the above noted values, figure 23 shows the shock positioned upstream of the convolution run and similar hill and valley pressure distributions, indicating that a multi-dimensional pressure gradient was not generated across the convolution run at these low NPR values.

When nozzle pressure ratio was increased above these low NPR values, figure 22 shows that there was a dramatic drop in F/F_i for each of the convoluted configurations. The drop in F/F_i occurred for the fine convoluted configuration (fig. 22(a)) at a NPR between 2.0 and 2.2, when the shock jumped from its position upstream of the convolution run at $x/x_t \approx 1.2$ to a position midway through the convolution run at $x/x_t \approx 1.6$ (fig. 23(a)). Flow visualization for the fine convoluted configuration in figure 25 shows a nearly normal shock at NPR=2.2 (fig. 25(a)) with a lambda foot structure significantly smaller than that of the baseline configuration (fig. 21(c)) at a similar NPR and shock location. With this "shock jump", flow over the convolution run was supersonic, a multi-dimensional pressure gradient was generated across the convolution run, and flow separation was almost completely alleviated.

As a result, nozzle internal flow could no longer adjust to exit conditions by detaching from the divergent flaps; thus, exhaust flow overexpansion losses increased (F/F_i decreased).

Above the "shock jump" NPR, F/F_i for the fine convoluted configuration increased continuously as overexpansion losses decreased (fig. 22(a)). Static pressure ratio distributions for the fine convoluted configuration in figure 23(a) indicate that the shock moved smoothly downstream with each subsequent increase in NPR. At each shock position, the pressure rise through the shock was gradual, the flow generally remained attached (local areas of separated flow are evident), and there was good pressure recovery downstream of the shock. A comparison of flow visualization for the fine convoluted configuration at NPRs of 2.2 and 2.6 in figure 25 shows a larger lambda foot structure and a more turbulent attached region downstream of the shock at the higher NPR value. As indicated in figure 23(a), the fine convoluted configuration was free of internal shocks at NPR>5.0. Losses in F/F_i due to the fine convolutions were as large as 6% at NPR=2.2, but decreased to less than 1% at NPR≥5.0 (see figure 22(a)).

The "shock jump" for the medium convoluted configuration occurred between NPRs of 1.8 and 2.0. The centerline static pressure distribution for the medium convoluted configuration (fig. 23(b)) at NPR=2.0 shows a gradual pressure rise through the shock and good downstream pressure recovery. Flow visualization for the medium convoluted configuration at NPR=2.0 (fig. 26(a)) shows turbulent, attached flow downstream of the shock, indicating that this configuration also provided good separation alleviation. However, F/F_i for the medium convoluted configuration (fig. 22(b)) was not continuous above the "shock jump" NPR (note discontinuity in F/F_i at 2.5<NPR<3.0). Static pressure ratio distributions for the medium convoluted configuration (fig. 23(b)) show that the main shock merged with the strong convolution valley oblique shock at a NPR between 2.0 and 2.6. A comparison of flow visualization for the medium convoluted configuration at NPRs of 2.0 and 2.6 in figure 26 indicates that the leading lambda foot remained in the same location while the main shock moved downstream and the lambda foot grew with increasing NPR. As this occurred, flow remained attached through the shock, and downstream pressure recovery was good.

As NPR was increased to 3.0, the shock once again jumped downstream, this time from $x/x_t \approx 1.6$ to a position near the nozzle exit at $x/x_t \approx 1.9$. As for the previous shock jump, there is a corresponding shift in nozzle thrust ratio (fig. 22(b)), though in this case the shift is more likely due to a loss effect than additional separation alleviation. As shown in figure 26(c), when the shock jumped downstream at NPR=3.0, it "uncovered" the valley oblique shock at the trailing edge of the convolution run such that loss effects of that shock could affect nozzle thrust ratio. Beyond NPR=3.0, the shock moved smoothly out of the nozzle, and the nozzle was shock free at NPR>4.6 (fig. 23(b)). The losses in F/F_i due to the medium convolutions were as large as 6.5% at NPR=2.0, but decreased to approximately 1% at NPR>4.6 (fig. 22(b)).

The "shock jump" for the medium-long convoluted configuration occurred between a NPR of 1.6 and 1.8 as indicated by the static pressure ratio distributions in figure 23(c). The centerline static pressure distribution at NPR=1.8 also indicates a double shock (one at $x/x_t \approx 1.45$ and one at $x/x_t \approx 1.6$) with a small separation bubble in between. Flow visualization for the medium-long convoluted configuration at NPR=1.8 (fig. 27(a)) shows the double shock with attached flow downstream of the second shock. Unlike the medium convoluted configuration, F/F_i for the medium-long convoluted configuration at NPR>2.0 was continuous (fig. 22(c)), and pressure distributions (fig. 23(c)) indicate that the shock moved smoothly downstream with each subsequent increase in NPR. At each shock position, the pressure rise through the shock was gradual, the internal flow remained attached, and there was strong pressure recovery downstream of the shock. Flow visualization for the medium-long convoluted configuration at NPR=2.6 (fig. 27(b))

shows a larger lambda foot structure and a more turbulent attached region downstream of the main shock than at the lower NPR. Static pressure ratio distributions (fig. 23(c)) indicate that the medium-long configuration was shock free at NPR>4.2.

As shown in figure 23(d), the "shock jump" for the coarse convoluted configuration occurred between a NPR of 1.6 and 1.8. For this configuration, the shock moved downstream after the initial "shock jump", but then merged with the valley oblique shock and remained in that position at $x/x_t \approx 1.6$ for NPRs between 2.2 and 3.8. A second jump in the shock position ($x/x_t \approx 1.6$ to $x/x_t \approx 1.75$) for the coarse convoluted configuration is evident in figure 23(d) at NPR=4.2, when the shock separated from the convolution valley oblique shock. This is observed in flow visualization photographs for the coarse convoluted configuration at NPRs of 3.8 and 4.2 in figure 28, which shows the shock structure further downstream at the higher NPR value. As was the case with the medium convoluted configuration, this jump coincided with a decrease in nozzle thrust ratio (note the change in slope of F/F_i at NPR≈4.0 in fig. 22(d)) when the valley oblique shock was uncovered and the loss effects of that shock were added. At NPR>4.2, the shock moved smoothly out of the nozzle, and the nozzle was shock free for NPR>5.4 as indicated by the pressure distributions of figure 23(d). The losses in F/F_i due to the coarse convolutions (fig. 22(d)) were as large as 8% at NPR=2.4, but decreased to approximately 2.6% near NPR_d.

The medium-long convoluted configuration provided the best combination of separation alleviation and continuous downstream shock movement (no shock jumps past the initial jump). Separation alleviation began at NPR=1.8 for this configuration, and the nozzle was shock free for NPR>4.2, which was a lower NPR than for any of the other convoluted configurations. The losses in F/F_i due to the medium-long convoluted geometry (fig. 22(c)) were as large as 7% at NPR=2.4, but decreased to less than 1% at NPR>5.0. At on-design conditions, the medium-long convoluted configuration suffered only a 0.6% loss in $(F/F_i)_{peak}$. This may be an acceptable on-design nozzle thrust ratio penalty given the excellent off-design flow separation alleviation capabilities of this configuration (assuming that external flow effects would cause additional drag when internal nozzle flow was separated).

Shock-Boundary Layer Interaction

Baseline configuration. Flow visualization at NPR=3.0 for the baseline configuration in figure 29 shows the shock with a large, well defined lambda foot structure and fully-detached flow separation beginning at the leading branch of the lambda foot and extending downstream. Shock angle measurements were made from figure 29, and were used in conjunction with oblique shock theory (ref. 24) in an effort to better describe the shock-boundary layer interaction as shown in figure 30.

Upstream of the leading lambda foot, flow was assumed to be locally parallel to the nozzle divergent flap and M_1 was calculated from $p/p_{t,j}$ values to be approximately 1.8. Flow decelerated across the leading lambda foot which, with an inclination angle β of approximately 52° from the nozzle divergent flap, resulted in a downstream Mach number M_2 of approximately 1.2. Using oblique shock theory, the flow turning angle θ across the leading lambda foot was calculated to be 15°. The leading lambda foot possessed the severity of a normal shock and was strong enough to completely detach nozzle flow from the divergent flaps. From the new flow direction, the trailing branch of the lambda foot had an inclination angle of $\beta \approx 63°$. For $M \approx 1.2$ approaching this shock, the corresponding flow turning angle of the trailing lambda foot was calculated to be $\theta \approx 3°$. This satisfied flow turning requirements of the fully detached flow separation region and resulted in nearly axial flow downstream of the trailing lambda foot.

In this shock-boundary layer interaction, it is apparent that the nozzle flap was steep enough and the remaining length of the nozzle past the flow separation point was short enough that reattachment would not occur, since the given shock structure resulted in nearly axial flow in the

nozzle. As a result, the free shear layer generated in the flow separation process became the actual exit shear layer of the nozzle and the flow separation point behaved as if it were the nozzle exit.

Convoluted configurations. Each convoluted configuration had dramatically different shock-boundary layer interaction characteristics than the baseline configuration. As indicated in figure 20, static pressure ratio distributions for the baseline configuration at NPR>1.41 were characterized by a single, sharp compression with subsequent shock-induced, boundary-layer separation. This behavior is illustrated by flow visualization in figure 21, which shows the baseline configuration with a large, well defined lambda foot structure, and fully detached flow downstream of the leading lambda foot.

Static pressure ratio distributions presented in figure 23 for the convoluted configurations indicate that the convoluted contouring significantly reduced, and in some cases totally alleviated, shock-induced boundary-layer separation. Pressure distributions indicate that a multi-dimensional pressure gradient was formed across the convolution run at all but the lowest NPRs. It is likely that the generation of streamwise vorticity energized the nozzle boundary layer upstream of the shock-boundary layer interaction region. The energized boundary layer was able to negotiate the severe adverse pressure gradient of the shock, thereby minimizing shock-induced boundary-layer interaction effects and alleviating flow separation.

Each convoluted configuration had a distinct shock-boundary layer interaction mechanism, undoubtedly due to the different contouring in each case. The fine convoluted configuration had the least aggressive contouring, resulting in shock-boundary layer interaction characteristics closest to the baseline nozzle. (Compare figures 20 and 23(a).) However, flow visualization for the fine convoluted configuration (fig. 25(a)) shows a noticeably smaller lambda foot structure than the baseline configuration and static pressure ratio distributions in figure 23(a) indicate that the fine convoluted contouring alleviated separation for all NPRs past the shock jump. The medium and medium-long convoluted configurations were designed with common spanwise profiles, but it appears that the slightly less aggressive streamwise run in the medium-long convoluted configuration provided the best off-design separation alleviation over the widest range of NPR with the lowest peak thrust ratio penalty. The coarse convoluted configuration also improved the shock-boundary layer interaction, but this configuration experienced substantial losses in peak thrust ratio.

Conclusions

An investigation was conducted in the model preparation area of the Langley 16-Foot Transonic Tunnel to determine the effects of convoluted divergent-flap contouring on the internal performance (nozzle thrust ratio) of a fixed-geometry exhaust nozzle. Testing was conducted at static conditions using a sub-scale, nonaxisymmetric, convergent-divergent nozzle model designed with interchangeable divergent flap surfaces. Force, moment, and pressure measurements were taken and internal focusing schlieren flow visualization was obtained for one baseline (no convolutions) and four convoluted configurations. All tests were conducted with no external flow and nozzle pressure ratio was varied during jet simulation from 1.25 to approximately 9.50. The results of this investigation indicate the following conclusions:

1. Convoluted configurations were found to significantly reduce, and in some cases totally alleviate, shock-induced, boundary-layer separation at off-design conditions. This indicates that the convoluted contouring energized and improved the condition of the nozzle boundary layer such that the boundary layer was able to resist the natural separation tendency of the exhaust flow. This did, however, result in off-design nozzle thrust ratio penalties that ranged from 3.6% to 6.4% below the fully separated baseline configuration, thus imposing a tradeoff between separation alleviation and nozzle

thrust ratio which may be acceptable in some applications.

2. Of the four convoluted configurations tested, the medium-long convoluted configuration provided the best combination of off-design separation alleviation and continuous downstream shock movement. Separation alleviation began at NPR=1.8 in this configuration, and the nozzle was shock free at NPR>4.2, earlier than any of the other convoluted configurations tested. Even with 26% more internal wetted area than the baseline configuration, the medium-long convoluted configuration had a peak thrust ratio of 0.980, only 0.6% below the baseline value.

3. At on-design conditions, nozzle thrust ratio for the convoluted configurations ranged from 1% to 2.9% below the baseline configuration. This was a result of the convolutions increasing skin friction and oblique shock losses inside the nozzle.

NASA Langley Research Center
Hampton, Virginia 23681-0001
January 4, 1999

References

1. Stitt, Leonard E.: Exhaust Nozzles for Propulsion Systems With Emphasis on Supersonic Cruise Aircraft. NASA RP-1235, 1990.

2. Berrier, Bobby L.; and Re, Richard, J.: A Review of Thrust Vectoring Schemes for Fighter Aircraft. AIAA-78-1023, July 1978.

3. Yetter, Jeffrey A.: Why Do Airlines Want and Use Thrust Reversers? NASA TM-109158, 1995.

4. Asbury, Scott C.; and Carlson, John R.: Transonic Aeropropulsive Performance of Advanced Exhaust Nozzles Designed for Reduced Radar Cross-Section Signatures. NASA TP-3505, 1995.

5. Gilkey, S. C.; Hines, R.W.: A Joint Propulsion Perspective of the Next Generation Supersonic Transport. AIAA-91-3330, September 1991.

6. Berrier, Bobby L.; and Re, Richard J.: Investigation of Convergent-Divergent Nozzle Applicable to Reduced-Power Supersonic Cruise Aircraft. NASA TP-1766, 1980.

7. Presz, W. M., Jr.; Werle, M.; and Paterson, R. W.: Trailing Edge Separation/Stall Alleviation. Journal of Propulsion and Power, vol. 25, 1987.

8. Presz, W. M., Jr.; Morin, B.; and Gousy, R.: Short Efficient Ejector Systems. AIAA-87-1837, June 1987.

9. Presz, Walter M., Jr.; Russell, William D.; and Tongue, Steve E.: Rippled Afterbody Performance Study. UTRC87-27, September 1987.

10. Skebe, S. A.; Paterson, R. W.; and Barber, T. J.: Experimental Investigation of Three-Dimensional Forced Mixer Lobe Flow Fields. AIAA-88-3785, July 1988.

11. Mercer, Charles E.; Berrier, Bobby L.; Capone, Francis J.; and Grayston, Alan M.: Data Reduction Formulas for the 16-Foot Transonic Tunnel–NASA Langley Research Center. Revision 2. NASA TM-107646, 1992.

12. Staff of the Propulsion Aerodynamics Branch: A User's Guide to the Langley 16-Foot Transonic Tunnel Complex, Revision 1. NASA TM-102750, 1990. (Supersedes NASA TM-83186, compiled by Kathryn H. Peddrew, 1981.)

13. Berrier, Bobby L.; and Re, Richard J.: Effects of Several Geometric Parameters on the Static Internal Performance of Three Nonaxisymmetric Nozzle Concepts. NASA TP-1468, 1979.

14. Paterson, R.W.: Turbofan Mixer Nozzle Flow Field - A Benchmark Experimental Study. Journal of Engineering for Gas Turbines and Power, July 1984.

15. Capone, Francis J.: Static Performance of Five Twin-Engine Nonaxisymmetric Nozzles with Vectoring and Reversing Capability. NASA TP-1224, 1978.

16. Coleman, Hugh W.; and Steele, W. Glenn, Jr.: Experimentation and Uncertainty Analysis for Engineers. John Wiley & Sons, 1989.

17. Wing, David J.; Mills, Charles T.L.; and Mason, Mary L.: Static Investigation of a Multiaxis Thrust-Vectoring Nozzle With Variable Internal Contouring Ability. NASA TP-3628, 1997.

18. Weinstein, L.M.: An Improved Large-Field Focusing Schlieren System. AIAA-91-0567, January 1991.

19. Capone, F.J.; Konarski, M.; Stevens, H.L.; and Willard, C.M.: Static Performance of Vectoring/Reversing Non-Axisymmetric Nozzles. AIAA-77-840, July 1977.

20. Re, Richard J.; and Leavitt, Laurence D.: Static Internal Performance Including Thrust Vectoring and Thrust Reversing of Two-Dimensional Convergent-Divergent Nozzles. NASA TP-2253, 1984.

21. Taylor, John G.: Static Investigation of a Two-Dimensional Convergent Divergent Exhaust Nozzle With Multiaxis Thrust Vectoring Capability. NASA TP-2973, 1990.

22. Hunter, Craig A.: An Approximate Theoretical Method for Modeling the Static Thrust Performance of Nonaxisymmetric Two-Dimensional Convergent Divergent Nozzles. NASA CR-195050, 1995.

23. Liepmann, Hans Wolfgang; and Roshko, Anatol: Elements of Gasdynamics. John Wiley & Sons, Inc., 1957.

24. Staff of NASA Ames Research Center: Equations, Tables, and Charts for Compressible Flow. NASA TR-1135, 1953.

Table 1. Nozzle Thrust Ratio Performance

Baseline Configuration		Fine Convoluted Configuration		Medium Convoluted Configuration		Medium-Long Convoluted Configuration		Coarse Convoluted Configuration	
NPR	**F/F_i**	**NPR**	**F/F_i**	**NPR**	**F/F_i**	**NPR**	**F/F_i**	**NPR**	**F/F_i**
1.26	0.869	**1.25**	0.849	**1.24**	0.849	**1.25**	0.855	**1.25**	0.832
1.40	0.832	**1.40**	0.819	**1.39**	0.820	**1.40**	0.817	**1.40**	0.814
1.61	0.837	**1.60**	0.816	**1.59**	0.822	**1.60**	0.836	**1.60**	0.825
1.81	0.830	**1.80**	0.845	**1.79**	0.810	**1.80**	0.794	**1.80**	0.792
2.01	0.865	**2.00**	0.851	**1.99**	0.802	**2.00**	0.798	**2.00**	0.799
2.21	0.882	**2.20**	0.825	**2.19**	0.823	**2.20**	0.814	**2.20**	0.811
2.41	0.904	**2.40**	0.845	**2.39**	0.846	**2.40**	0.836	**2.40**	0.824
2.61	0.913	**2.60**	0.861	**2.59**	0.867	**2.60**	0.855	**2.60**	0.844
3.01	0.924	**3.00**	0.883	**2.99**	0.869	**3.00**	0.887	**3.00**	0.877
3.41	0.935	**3.40**	0.905	**3.39**	0.898	**3.40**	0.905	**3.39**	0.902
3.82	0.944	**3.80**	0.921	**3.79**	0.918	**3.80**	0.921	**3.80**	0.917
4.22	0.951	**4.20**	0.937	**4.19**	0.933	**4.20**	0.936	**4.20**	0.920
4.62	0.959	**4.60**	0.948	**4.59**	0.945	**4.60**	0.947	**4.60**	0.925
5.02	0.965	**5.00**	0.957	**4.99**	0.953	**5.00**	0.956	**4.99**	0.931
5.42	0.971	**5.40**	0.963	**5.39**	0.960	**5.40**	0.962	**5.40**	0.937
5.82	0.975	**6.20**	0.972	**6.19**	0.968	**6.19**	0.970	**6.20**	0.946
6.23	0.979	**7.00**	0.976	**6.99**	0.972	**7.00**	0.976	**6.99**	0.951
7.03	0.983	**8.00**	0.979	**7.99**	0.975	**8.00**	0.979	**8.00**	0.955
8.04	0.986	**8.91**	0.980	**8.89**	0.976	**8.89**	0.979	**8.89**	0.957
8.94	0.986	**9.50**	0.980	**9.50**	0.976	**9.51**	0.980	**9.50**	0.957
9.54	0.986								

Table 2. Nozzle Internal Static Pressure Ratios for the Baseline Configuration

(a) Convergent Flap, $z = 0.000$

$p/p_{t,j}$ at x/x_t of

NPR	0.330	0.440	0.550	0.659	0.769	0.890	1.000
1.26	0.959	0.946	0.930	0.903	0.856	0.681	0.448
1.40	0.958	0.945	0.927	0.899	0.850	0.671	0.391
1.61	0.957	0.943	0.927	0.899	0.849	0.670	0.369
1.81	0.958	0.943	0.928	0.899	0.850	0.670	0.369
2.01	0.958	0.942	0.927	0.899	0.849	0.670	0.368
2.21	0.958	0.943	0.929	0.899	0.850	0.670	0.368
2.41	0.958	0.942	0.928	0.899	0.850	0.670	0.368
2.61	0.959	0.943	0.929	0.900	0.851	0.670	0.368
3.01	0.959	0.943	0.929	0.900	0.851	0.670	0.368
3.41	0.959	0.943	0.929	0.900	0.851	0.671	0.369
3.82	0.959	0.943	0.929	0.900	0.850	0.671	0.369
4.22	0.959	0.943	0.929	0.899	0.850	0.671	0.369
4.62	0.959	0.942	0.929	0.899	0.850	0.671	0.369
5.02	0.959	0.942	0.928	0.899	0.850	0.671	0.368
5.42	0.958	0.942	0.928	0.899	0.849	0.670	0.368
5.82	0.958	0.941	0.928	0.898	0.848	0.670	0.367
6.23	0.957	0.941	0.927	0.898	0.848	0.669	0.366
7.03	0.957	0.940	0.926	0.897	0.847	0.669	0.365
8.04	0.956	0.940	0.925	0.896	0.846	0.668	0.364
8.94	0.956	0.939	0.924	0.895	0.845	0.668	0.362
9.54	0.956	0.939	0.924	0.895	0.845	0.668	0.362

(b) Divergent Flap, $z = 0.000$

$p/p_{t,j}$ at x/x_t of

NPR	1.111	1.154	1.198	1.241	1.284	1.327	1.370	1.413	1.456	1.500	1.543	1.586	1.629	1.672	1.715	1.758	1.802	1.845	1.888	1.931	1.974
1.26	0.600	0.641	0.670	0.687	0.704	0.716	0.729	0.737	0.746	0.753	0.760	0.765	0.770	0.774	0.778	0.781	0.783	0.786	0.788	0.790	0.792
1.40	0.447	0.495	0.528	0.546	0.566	0.581	0.596	0.610	0.624	0.635	0.648	0.657	0.666	0.673	0.680	0.686	0.691	0.696	0.700	0.703	0.706
1.61	0.274	0.281	0.294	0.321	0.441	0.468	0.482	0.492	0.503	0.516	0.533	0.546	0.562	0.578	0.593	0.605	0.614	0.622	0.626	0.628	0.627
1.81	0.277	0.285	0.295	0.283	0.277	0.286	0.407	0.433	0.439	0.441	0.444	0.445	0.450	0.455	0.463	0.472	0.483	0.496	0.509	0.523	0.537
2.01	0.278	0.283	0.292	0.282	0.275	0.281	0.413	0.438	0.447	0.451	0.455	0.454	0.456	0.457	0.457	0.459	0.461	0.464	0.468	0.469	0.462
2.21	0.280	0.288	0.293	0.284	0.277	0.263	0.251	0.340	0.402	0.413	0.418	0.420	0.421	0.422	0.422	0.423	0.424	0.425	0.428	0.429	0.420
2.41	0.282	0.285	0.291	0.284	0.276	0.262	0.250	0.234	0.228	0.361	0.382	0.386	0.389	0.391	0.392	0.392	0.392	0.392	0.395	0.395	0.388
2.61	0.282	0.290	0.293	0.286	0.277	0.264	0.252	0.236	0.223	0.209	0.314	0.351	0.359	0.363	0.364	0.365	0.366	0.367	0.368	0.367	0.361
3.01	0.283	0.291	0.293	0.286	0.276	0.264	0.252	0.237	0.224	0.209	0.198	0.183	0.175	0.288	0.305	0.311	0.313	0.315	0.316	0.318	0.313
3.41	0.285	0.291	0.291	0.286	0.276	0.264	0.252	0.237	0.224	0.210	0.198	0.184	0.171	0.159	0.149	0.245	0.267	0.273	0.277	0.279	0.279
3.82	0.284	0.291	0.289	0.286	0.276	0.265	0.253	0.238	0.225	0.210	0.198	0.185	0.172	0.160	0.150	0.139	0.132	0.221	0.240	0.247	0.252
4.22	0.284	0.290	0.289	0.286	0.276	0.265	0.253	0.238	0.225	0.211	0.198	0.185	0.172	0.160	0.150	0.139	0.131	0.123	0.145	0.213	0.225
4.62	0.283	0.290	0.288	0.286	0.275	0.265	0.253	0.238	0.225	0.211	0.198	0.185	0.173	0.161	0.151	0.140	0.131	0.123	0.115	0.115	0.198
5.02	0.283	0.290	0.288	0.285	0.275	0.265	0.253	0.239	0.226	0.212	0.198	0.186	0.173	0.161	0.151	0.141	0.132	0.124	0.116	0.110	0.159
5.42	0.283	0.289	0.288	0.285	0.275	0.265	0.253	0.238	0.226	0.212	0.199	0.187	0.174	0.162	0.152	0.141	0.133	0.124	0.117	0.110	0.107
5.82	0.282	0.289	0.287	0.285	0.275	0.265	0.253	0.239	0.226	0.212	0.199	0.187	0.174	0.162	0.152	0.141	0.133	0.125	0.117	0.110	0.104
6.23	0.281	0.288	0.287	0.284	0.274	0.265	0.253	0.239	0.226	0.213	0.199	0.187	0.174	0.163	0.153	0.142	0.133	0.125	0.118	0.111	0.104
7.03	0.280	0.287	0.286	0.283	0.273	0.264	0.252	0.239	0.226	0.213	0.199	0.188	0.175	0.163	0.153	0.142	0.134	0.126	0.118	0.111	0.105
8.04	0.279	0.285	0.285	0.282	0.272	0.264	0.252	0.238	0.226	0.213	0.200	0.188	0.175	0.164	0.154	0.143	0.135	0.127	0.119	0.112	0.106
8.94	0.278	0.284	0.284	0.282	0.272	0.263	0.252	0.238	0.226	0.214	0.200	0.188	0.176	0.165	0.155	0.144	0.135	0.127	0.119	0.112	0.106
9.54	0.277	0.283	0.283	0.281	0.271	0.263	0.251	0.238	0.226	0.214	0.200	0.189	0.176	0.165	0.155	0.144	0.136	0.128	0.120	0.113	0.106

Table 2. Concluded

(c) Divergent Flap, $z = 1.595$

$p/p_{t,j}$ at x/x_t of

NPR	1.111	1.154	1.198	1.241	1.284	1.327	1.370	1.413	1.456	1.500	1.543	1.586	1.629	1.672	1.715	1.758	1.802	1.845	1.888	1.931	1.974
1.26	0.721	0.738	0.743	0.747	0.748	0.748	0.749	0.748	0.749	0.751	0.752	0.753	0.754	0.756	0.757	0.759	0.759	0.762	0.761	0.762	0.759
1.40	0.566	0.628	0.647	0.658	0.660	0.660	0.660	0.658	0.657	0.658	0.657	0.659	0.658	0.660	0.661	0.662	0.662	0.664	0.664	0.665	0.664
1.61	0.282	0.295	0.328	0.404	0.461	0.504	0.526	0.536	0.545	0.555	0.564	0.578	0.587	0.596	0.603	0.610	0.612	0.617	0.617	0.620	0.620
1.81	0.280	0.288	0.291	0.292	0.289	0.283	0.276	0.344	0.435	0.486	0.515	0.531	0.535	0.538	0.541	0.544	0.546	0.550	0.551	0.553	0.553
2.01	0.278	0.285	0.289	0.288	0.281	0.269	0.256	0.245	0.342	0.398	0.415	0.433	0.449	0.464	0.474	0.484	0.487	0.491	0.493	0.496	0.498
2.21	0.280	0.287	0.291	0.290	0.283	0.270	0.256	0.242	0.239	0.346	0.379	0.387	0.392	0.399	0.405	0.411	0.416	0.422	0.427	0.434	0.439
2.41	0.278	0.286	0.291	0.289	0.281	0.268	0.253	0.238	0.226	0.236	0.355	0.372	0.376	0.379	0.381	0.384	0.384	0.388	0.391	0.395	0.392
2.61	0.280	0.290	0.294	0.291	0.283	0.269	0.254	0.238	0.225	0.212	0.222	0.340	0.353	0.358	0.359	0.361	0.362	0.364	0.365	0.366	0.360
3.01	0.283	0.294	0.295	0.290	0.282	0.269	0.254	0.238	0.224	0.210	0.197	0.185	0.174	0.239	0.294	0.302	0.303	0.304	0.304	0.308	0.314
3.41	0.286	0.295	0.295	0.289	0.282	0.269	0.254	0.238	0.225	0.210	0.197	0.185	0.172	0.162	0.153	0.202	0.260	0.270	0.273	0.277	0.278
3.82	0.286	0.295	0.295	0.289	0.282	0.269	0.255	0.239	0.225	0.211	0.197	0.185	0.172	0.161	0.152	0.142	0.134	0.190	0.234	0.244	0.251
4.22	0.286	0.295	0.295	0.289	0.282	0.269	0.255	0.239	0.226	0.211	0.198	0.185	0.173	0.162	0.152	0.142	0.134	0.127	0.121	0.204	0.224
4.62	0.285	0.295	0.295	0.288	0.281	0.270	0.255	0.240	0.226	0.212	0.198	0.186	0.174	0.162	0.152	0.143	0.134	0.127	0.120	0.115	0.194
5.02	0.285	0.294	0.295	0.288	0.281	0.270	0.255	0.240	0.226	0.212	0.199	0.186	0.174	0.163	0.152	0.143	0.134	0.127	0.120	0.114	0.144
5.42	0.285	0.294	0.295	0.287	0.281	0.270	0.256	0.240	0.226	0.212	0.199	0.187	0.174	0.163	0.153	0.143	0.134	0.127	0.120	0.114	0.110
5.82	0.284	0.293	0.295	0.287	0.280	0.270	0.256	0.240	0.227	0.212	0.199	0.187	0.175	0.163	0.153	0.143	0.135	0.127	0.120	0.113	0.108
6.23	0.283	0.293	0.294	0.286	0.280	0.269	0.256	0.240	0.227	0.213	0.200	0.188	0.175	0.164	0.154	0.144	0.135	0.127	0.120	0.113	0.107
7.03	0.282	0.291	0.293	0.285	0.278	0.268	0.255	0.240	0.227	0.213	0.200	0.188	0.176	0.165	0.155	0.145	0.136	0.128	0.120	0.113	0.107
8.04	0.280	0.290	0.292	0.284	0.277	0.268	0.256	0.241	0.227	0.213	0.201	0.189	0.177	0.166	0.156	0.146	0.136	0.128	0.121	0.114	0.107
8.94	0.279	0.288	0.292	0.284	0.276	0.267	0.255	0.241	0.227	0.213	0.201	0.189	0.178	0.166	0.156	0.146	0.137	0.129	0.121	0.114	0.108
9.54	0.278	0.288	0.292	0.283	0.275	0.268	0.256	0.241	0.227	0.213	0.201	0.190	0.178	0.166	0.156	0.146	0.137	0.129	0.121	0.115	0.108

Table 3. Nozzle Internal Static Pressure Ratios for the Fine Convoluted Configuration

(a) Convergent Flap, $z = 0.000$

$p/p_{t,j}$ at x/x_t of

NPR	0.330	0.440	0.550	0.659	0.769	0.890	1.000
1.25	0.960	0.950	0.931	0.904	0.857	0.684	0.458
1.40	0.958	0.946	0.928	0.900	0.851	0.672	0.379
1.60	0.958	0.946	0.927	0.899	0.850	0.670	0.369
1.80	0.958	0.946	0.927	0.899	0.849	0.670	0.368
2.00	0.958	0.946	0.927	0.899	0.849	0.670	0.367
2.20	0.958	0.946	0.928	0.899	0.849	0.670	0.368
2.40	0.958	0.946	0.928	0.899	0.849	0.671	0.367
2.60	0.958	0.945	0.928	0.899	0.849	0.671	0.367
3.00	0.958	0.946	0.928	0.899	0.849	0.671	0.368
3.40	0.959	0.945	0.928	0.900	0.850	0.671	0.368
3.80	0.958	0.945	0.928	0.899	0.849	0.671	0.367
4.20	0.958	0.945	0.928	0.899	0.849	0.670	0.367
4.60	0.958	0.945	0.927	0.898	0.848	0.670	0.366
5.00	0.958	0.945	0.927	0.898	0.847	0.670	0.365
5.40	0.957	0.944	0.927	0.898	0.847	0.669	0.364
6.20	0.957	0.944	0.925	0.896	0.846	0.668	0.362
7.00	0.956	0.943	0.925	0.896	0.845	0.667	0.361
8.00	0.956	0.942	0.924	0.895	0.844	0.666	0.359
8.91	0.955	0.942	0.923	0.894	0.843	0.665	0.357
9.50	0.955	0.942	0.922	0.894	0.842	0.665	0.357

(b) Divergent Flap, $z = 0.000$ (Hill)

$p/p_{t,j}$ at x/x_t of

NPR	1.111	1.154	1.198	1.241	1.284	1.327	1.370	1.413	1.456	1.500	1.543	1.586	1.629	1.672	1.715	1.758	1.802	1.845	1.888	1.931	1.974
1.25	0.613	0.660	0.684	0.704	0.718	0.731	0.741	0.748	0.753	0.756	0.761	0.766	0.771	0.778	0.783	0.787	0.789	0.794	0.795	0.798	0.797
1.40	0.433	0.496	0.534	0.562	0.583	0.599	0.611	0.620	0.628	0.633	0.641	0.650	0.661	0.674	0.684	0.692	0.698	0.703	0.706	0.712	0.710
1.60	0.272	0.302	0.439	0.476	0.489	0.497	0.498	0.497	0.496	0.497	0.502	0.509	0.521	0.534	0.550	0.565	0.578	0.591	0.602	0.620	0.612
1.80	0.270	0.281	0.369	0.461	0.483	0.495	0.501	0.503	0.505	0.507	0.508	0.508	0.509	0.510	0.511	0.514	0.516	0.520	0.523	0.515	0.522
2.00	0.270	0.281	0.281	0.277	0.405	0.457	0.468	0.472	0.473	0.476	0.478	0.480	0.481	0.481	0.481	0.482	0.482	0.483	0.482	0.475	0.478
2.20	0.269	0.280	0.281	0.276	0.267	0.259	0.258	0.254	0.226	0.195	0.193	0.190	0.230	0.303	0.343	0.369	0.369	0.369	0.380	0.432	0.405
2.40	0.269	0.281	0.281	0.276	0.267	0.259	0.258	0.254	0.226	0.196	0.194	0.181	0.187	0.259	0.304	0.336	0.346	0.344	0.341	0.364	0.346
2.60	0.270	0.281	0.281	0.276	0.266	0.259	0.257	0.253	0.226	0.195	0.194	0.181	0.178	0.197	0.266	0.299	0.320	0.327	0.329	0.342	0.331
3.00	0.271	0.281	0.281	0.276	0.266	0.258	0.257	0.253	0.226	0.196	0.196	0.180	0.170	0.156	0.161	0.166	0.228	0.258	0.281	0.306	0.295
3.40	0.272	0.281	0.281	0.275	0.266	0.258	0.257	0.253	0.227	0.197	0.197	0.181	0.170	0.154	0.156	0.134	0.180	0.212	0.228	0.247	0.243
3.80	0.272	0.280	0.280	0.275	0.266	0.258	0.257	0.254	0.228	0.197	0.198	0.181	0.170	0.155	0.157	0.133	0.135	0.168	0.194	0.210	0.204
4.20	0.272	0.279	0.280	0.275	0.265	0.258	0.258	0.255	0.228	0.198	0.198	0.182	0.171	0.155	0.158	0.134	0.133	0.125	0.118	0.192	0.140
4.60	0.271	0.279	0.280	0.275	0.265	0.258	0.258	0.255	0.229	0.199	0.199	0.182	0.171	0.156	0.159	0.134	0.134	0.125	0.117	0.172	0.113
5.00	0.271	0.278	0.279	0.275	0.265	0.258	0.258	0.255	0.229	0.200	0.199	0.183	0.171	0.156	0.160	0.135	0.135	0.126	0.118	0.130	0.113
5.40	0.270	0.278	0.278	0.274	0.265	0.257	0.258	0.255	0.229	0.200	0.199	0.183	0.171	0.156	0.161	0.135	0.135	0.126	0.119	0.109	0.114
6.20	0.268	0.276	0.277	0.273	0.263	0.256	0.257	0.255	0.229	0.200	0.200	0.183	0.171	0.157	0.162	0.136	0.136	0.127	0.119	0.108	0.115
7.00	0.267	0.274	0.275	0.271	0.262	0.256	0.257	0.255	0.229	0.200	0.200	0.183	0.172	0.157	0.162	0.137	0.137	0.128	0.120	0.109	0.115
8.00	0.265	0.273	0.274	0.270	0.261	0.255	0.256	0.254	0.229	0.200	0.200	0.183	0.172	0.157	0.162	0.137	0.137	0.128	0.120	0.109	0.116
8.91	0.264	0.271	0.273	0.269	0.260	0.254	0.256	0.254	0.228	0.200	0.200	0.183	0.172	0.157	0.162	0.137	0.138	0.128	0.120	0.110	0.116
9.50	0.264	0.271	0.272	0.269	0.260	0.254	0.256	0.254	0.228	0.200	0.200	0.184	0.172	0.158	0.163	0.137	0.138	0.129	0.121	0.110	0.116

Table 3. Concluded

(c) Divergent Flap, $z = 0.1995$ (Valley)

$p/p_{t,j}$ at x/x_t of

NPR	1.327	1.370	1.413	1.456	1.500	1.543	1.586	1.629	1.672	1.715
1.25	0.730	0.741	0.746	0.756	0.762	0.767	0.770	0.774	0.780	0.784
1.40	0.598	0.614	0.622	0.631	0.640	0.648	0.656	0.666	0.677	0.686
1.60	0.497	0.503	0.502	0.505	0.508	0.515	0.520	0.527	0.537	0.552
1.80	0.499	0.506	0.508	0.511	0.513	0.514	0.513	0.513	0.511	0.513
2.00	0.460	0.472	0.474	0.478	0.480	0.482	0.483	0.483	0.483	0.483
2.20	0.249	0.235	0.210	0.221	0.227	0.230	0.237	0.258	0.305	0.343
2.40	0.249	0.235	0.211	0.221	0.228	0.230	0.221	0.222	0.250	0.303
2.60	0.248	0.235	0.211	0.222	0.228	0.230	0.220	0.194	0.156	0.248
3.00	0.248	0.236	0.211	0.222	0.229	0.230	0.220	0.188	0.127	0.148
3.40	0.248	0.236	0.212	0.222	0.229	0.231	0.221	0.190	0.126	0.137
3.80	0.249	0.237	0.212	0.222	0.229	0.231	0.221	0.191	0.127	0.137
4.20	0.248	0.237	0.212	0.222	0.230	0.231	0.222	0.191	0.128	0.137
4.60	0.248	0.237	0.212	0.222	0.230	0.231	0.222	0.192	0.128	0.138
5.00	0.248	0.237	0.212	0.222	0.230	0.231	0.222	0.193	0.129	0.138
5.40	0.248	0.237	0.212	0.222	0.230	0.232	0.223	0.193	0.129	0.139
6.20	0.246	0.236	0.211	0.222	0.230	0.232	0.223	0.193	0.130	0.139
7.00	0.245	0.235	0.211	0.221	0.230	0.232	0.223	0.194	0.131	0.139
8.00	0.245	0.234	0.210	0.221	0.229	0.232	0.223	0.194	0.132	0.140
8.91	0.244	0.234	0.210	0.220	0.229	0.232	0.223	0.194	0.132	0.140
9.50	0.244	0.233	0.209	0.220	0.229	0.232	0.224	0.194	0.132	0.141

(d) Divergent Flap, $z = 1.595$ (Hill)

$p/p_{t,j}$ at x/x_t of

NPR	1.111	1.154	1.198	1.241	1.284	1.327	1.370	1.413	1.456	1.500	1.543	1.586	1.629	1.672	1.715	1.758	1.802	1.845	1.888	1.931	1.974
1.25	0.698	0.740	0.752	0.758	0.758	0.760	0.756	0.756	0.753	0.752	0.752	0.754	0.755	0.762	0.765	0.768	0.768	0.770	0.770	0.771	0.770
1.40	0.480	0.550	0.584	0.607	0.618	0.633	0.632	0.646	0.651	0.655	0.659	0.665	0.669	0.680	0.686	0.688	0.691	0.694	0.696	0.699	0.701
1.60	0.285	0.353	0.412	0.443	0.463	0.487	0.460	0.504	0.526	0.538	0.547	0.562	0.578	0.600	0.611	0.616	0.619	0.622	0.622	0.624	0.625
1.80	0.274	0.281	0.293	0.373	0.447	0.479	0.489	0.488	0.490	0.490	0.494	0.501	0.506	0.512	0.516	0.520	0.524	0.529	0.533	0.540	0.546
2.00	0.273	0.281	0.284	0.285	0.279	0.414	0.460	0.466	0.468	0.472	0.475	0.475	0.474	0.474	0.472	0.471	0.470	0.472	0.474	0.479	0.473
2.20	0.275	0.282	0.284	0.285	0.274	0.268	0.265	0.262	0.257	0.312	0.352	0.351	0.382	0.406	0.419	0.423	0.437	0.445	0.447	0.448	0.451
2.40	0.276	0.283	0.284	0.283	0.272	0.263	0.261	0.256	0.230	0.215	0.264	0.246	0.310	0.348	0.366	0.371	0.392	0.406	0.413	0.416	0.416
2.60	0.276	0.283	0.286	0.282	0.270	0.261	0.259	0.253	0.226	0.207	0.221	0.176	0.226	0.285	0.319	0.329	0.353	0.372	0.382	0.386	0.387
3.00	0.275	0.285	0.288	0.280	0.270	0.260	0.259	0.254	0.224	0.202	0.205	0.163	0.163	0.151	0.163	0.169	0.232	0.257	0.294	0.326	0.341
3.40	0.276	0.286	0.288	0.280	0.270	0.261	0.260	0.255	0.224	0.202	0.205	0.162	0.162	0.148	0.159	0.139	0.150	0.167	0.206	0.271	0.299
3.80	0.275	0.286	0.287	0.280	0.270	0.261	0.260	0.256	0.225	0.202	0.205	0.163	0.163	0.147	0.158	0.137	0.142	0.151	0.171	0.195	0.221
4.20	0.275	0.285	0.287	0.279	0.270	0.261	0.260	0.256	0.226	0.203	0.205	0.163	0.163	0.147	0.159	0.136	0.138	0.135	0.142	0.163	0.193
4.60	0.275	0.285	0.286	0.279	0.270	0.261	0.260	0.257	0.226	0.204	0.206	0.164	0.164	0.147	0.159	0.137	0.137	0.130	0.125	0.133	0.161
5.00	0.274	0.284	0.286	0.279	0.270	0.261	0.259	0.257	0.226	0.205	0.206	0.164	0.165	0.147	0.159	0.137	0.137	0.130	0.122	0.119	0.133
5.40	0.273	0.284	0.285	0.278	0.269	0.261	0.260	0.257	0.227	0.206	0.206	0.164	0.165	0.147	0.160	0.137	0.138	0.130	0.122	0.116	0.117
6.20	0.271	0.282	0.283	0.276	0.267	0.259	0.258	0.256	0.226	0.206	0.206	0.165	0.166	0.148	0.162	0.139	0.140	0.132	0.123	0.116	0.113
7.00	0.270	0.280	0.282	0.274	0.266	0.258	0.257	0.255	0.226	0.205	0.206	0.165	0.166	0.147	0.162	0.138	0.140	0.132	0.123	0.117	0.114
8.00	0.269	0.279	0.280	0.272	0.264	0.257	0.256	0.255	0.225	0.205	0.205	0.165	0.166	0.147	0.162	0.138	0.140	0.132	0.123	0.117	0.113
8.91	0.268	0.278	0.279	0.271	0.263	0.256	0.255	0.255	0.225	0.205	0.205	0.165	0.166	0.148	0.162	0.139	0.140	0.132	0.123	0.116	0.112
9.50	0.268	0.277	0.279	0.270	0.263	0.256	0.255	0.254	0.225	0.206	0.205	0.165	0.166	0.148	0.162	0.139	0.140	0.132	0.124	0.117	0.111

Table 4. Nozzle Internal Static Pressure Ratios for the Medium Convoluted Configuration

(a) Convergent Flap, $z = 0.000$

$p/p_{t,j}$ at x/x_t of

NPR	0.330	0.440	0.550	0.659	0.769	0.890	1.000
1.24	0.961	0.951	0.933	0.904	0.861	0.683	0.452
1.39	0.959	0.948	0.930	0.901	0.854	0.673	0.398
1.59	0.958	0.948	0.929	0.898	0.852	0.670	0.367
1.79	0.958	0.948	0.929	0.899	0.852	0.670	0.367
1.99	0.958	0.947	0.930	0.899	0.851	0.670	0.367
2.19	0.959	0.947	0.929	0.899	0.851	0.670	0.366
2.39	0.959	0.947	0.930	0.899	0.851	0.670	0.367
2.59	0.959	0.947	0.930	0.899	0.850	0.669	0.366
2.99	0.959	0.946	0.930	0.900	0.850	0.670	0.367
3.39	0.959	0.946	0.929	0.899	0.850	0.670	0.367
3.79	0.959	0.946	0.929	0.899	0.850	0.670	0.367
4.19	0.958	0.946	0.929	0.899	0.849	0.669	0.367
4.59	0.958	0.946	0.929	0.899	0.849	0.669	0.366
4.99	0.958	0.945	0.928	0.898	0.848	0.669	0.365
5.39	0.958	0.944	0.927	0.898	0.847	0.668	0.364
6.19	0.957	0.944	0.926	0.897	0.846	0.667	0.363
6.99	0.956	0.943	0.925	0.896	0.845	0.666	0.361
7.99	0.956	0.942	0.924	0.895	0.844	0.665	0.359
8.89	0.955	0.942	0.923	0.894	0.843	0.665	0.358
9.50	0.955	0.942	0.923	0.894	0.842	0.665	0.357

(b) Divergent Flap, $z = 0.000$ (Hill)

$p/p_{t,j}$ at x/x_t of

NPR	1.111	1.154	1.198	1.241	1.284	1.327	1.370	1.413	1.456	1.500	1.543	1.586	1.629	1.672	1.715	1.758	1.802	1.845	1.888	1.931	1.974
1.24	0.624	0.660	0.685	0.704	0.719	0.738	0.749	0.762	0.756	0.748	0.754	0.765	0.772	0.779	0.784	0.788	0.792	0.795	0.798	0.800	0.801
1.39	0.491	0.523	0.546	0.563	0.578	0.596	0.606	0.619	0.624	0.621	0.628	0.640	0.651	0.664	0.675	0.685	0.692	0.698	0.704	0.708	0.711
1.59	0.272	0.279	0.295	0.365	0.454	0.504	0.545	0.606	0.601	0.547	0.555	0.579	0.598	0.606	0.618	0.625	0.624	0.627	0.629	0.630	0.628
1.79	0.271	0.279	0.282	0.278	0.273	0.361	0.393	0.408	0.401	0.399	0.394	0.397	0.409	0.428	0.462	0.489	0.511	0.527	0.540	0.550	0.555
1.99	0.271	0.281	0.282	0.279	0.272	0.263	0.298	0.320	0.260	0.187	0.155	0.229	0.277	0.310	0.370	0.431	0.472	0.497	0.509	0.513	0.510
2.19	0.272	0.280	0.283	0.279	0.272	0.263	0.297	0.319	0.260	0.186	0.139	0.226	0.253	0.277	0.320	0.355	0.383	0.401	0.418	0.433	0.444
2.39	0.272	0.281	0.283	0.280	0.272	0.263	0.297	0.320	0.261	0.186	0.136	0.219	0.247	0.265	0.294	0.332	0.353	0.364	0.375	0.386	0.394
2.59	0.272	0.281	0.284	0.280	0.272	0.263	0.296	0.319	0.261	0.186	0.136	0.210	0.240	0.259	0.275	0.308	0.327	0.337	0.346	0.355	0.361
2.99	0.273	0.281	0.283	0.279	0.272	0.263	0.296	0.319	0.262	0.187	0.137	0.197	0.196	0.179	0.146	0.178	0.152	0.139	0.148	0.241	0.284
3.39	0.272	0.281	0.282	0.278	0.271	0.263	0.296	0.319	0.263	0.187	0.137	0.199	0.195	0.172	0.139	0.169	0.140	0.129	0.119	0.149	0.241
3.79	0.271	0.280	0.282	0.278	0.271	0.263	0.296	0.320	0.264	0.188	0.138	0.200	0.193	0.169	0.139	0.168	0.138	0.129	0.119	0.117	0.213
4.19	0.271	0.279	0.281	0.278	0.271	0.263	0.296	0.320	0.264	0.189	0.138	0.200	0.192	0.167	0.140	0.168	0.138	0.130	0.120	0.115	0.167
4.59	0.270	0.279	0.281	0.278	0.270	0.262	0.296	0.320	0.264	0.190	0.139	0.201	0.192	0.167	0.140	0.169	0.138	0.130	0.120	0.115	0.114
4.99	0.269	0.278	0.280	0.277	0.270	0.262	0.296	0.320	0.264	0.190	0.139	0.200	0.192	0.167	0.140	0.170	0.139	0.131	0.121	0.115	0.111
5.39	0.268	0.277	0.279	0.277	0.270	0.261	0.296	0.320	0.265	0.191	0.140	0.200	0.192	0.167	0.141	0.171	0.139	0.131	0.122	0.115	0.109
6.19	0.267	0.275	0.277	0.275	0.268	0.260	0.295	0.319	0.265	0.191	0.140	0.200	0.192	0.168	0.142	0.173	0.140	0.131	0.123	0.116	0.109
6.99	0.265	0.273	0.276	0.274	0.267	0.258	0.295	0.319	0.264	0.192	0.141	0.200	0.191	0.169	0.143	0.175	0.141	0.132	0.123	0.116	0.109
7.99	0.263	0.272	0.274	0.273	0.266	0.257	0.294	0.318	0.264	0.192	0.141	0.199	0.191	0.170	0.143	0.177	0.141	0.133	0.124	0.117	0.109
8.89	0.262	0.271	0.273	0.272	0.265	0.256	0.294	0.318	0.264	0.193	0.141	0.199	0.192	0.171	0.144	0.179	0.142	0.133	0.124	0.117	0.109
9.50	0.262	0.270	0.272	0.271	0.265	0.256	0.294	0.318	0.264	0.193	0.141	0.199	0.192	0.171	0.144	0.180	0.142	0.133	0.124	0.117	0.109

Table 4. Concluded

(c) Divergent Flap, $z = 0.1995$ (Valley)

$p/p_{t,j}$ at x/x_t of

NPR	1.327	1.370	1.413	1.456	1.500	1.543	1.586	1.629	1.672	1.715
1.24	0.732	0.744	0.705	0.758	0.764	0.769	0.772	0.779	0.780	0.785
1.39	0.595	0.609	0.578	0.628	0.636	0.643	0.647	0.660	0.667	0.677
1.59	0.512	0.537	0.526	0.570	0.581	0.590	0.600	0.617	0.610	0.616
1.79	0.389	0.414	0.378	0.420	0.424	0.426	0.421	0.428	0.429	0.458
1.99	0.243	0.224	0.171	0.211	0.274	0.324	0.353	0.389	0.296	0.389
2.19	0.244	0.225	0.162	0.211	0.273	0.321	0.347	0.380	0.263	0.356
2.39	0.244	0.226	0.178	0.212	0.273	0.320	0.346	0.377	0.233	0.333
2.59	0.245	0.226	0.171	0.212	0.274	0.320	0.343	0.373	0.207	0.303
2.99	0.247	0.227	0.175	0.213	0.273	0.318	0.341	0.370	0.160	0.098
3.39	0.248	0.228	0.172	0.214	0.273	0.318	0.340	0.369	0.161	0.090
3.79	0.249	0.228	0.179	0.215	0.273	0.317	0.340	0.369	0.161	0.092
4.19	0.250	0.228	0.182	0.215	0.273	0.317	0.341	0.368	0.161	0.093
4.59	0.250	0.227	0.179	0.216	0.273	0.317	0.341	0.369	0.161	0.094
4.99	0.250	0.227	0.182	0.216	0.274	0.317	0.341	0.369	0.162	0.094
5.39	0.249	0.226	0.189	0.216	0.274	0.317	0.341	0.369	0.162	0.095
6.19	0.248	0.225	0.186	0.217	0.273	0.317	0.342	0.369	0.162	0.097
6.99	0.247	0.224	0.186	0.217	0.273	0.317	0.342	0.369	0.161	0.098
7.99	0.246	0.223	0.186	0.217	0.273	0.318	0.342	0.369	0.161	0.099
8.89	0.245	0.222	0.185	0.217	0.273	0.318	0.342	0.369	0.161	0.100
9.50	0.244	0.222	0.187	0.216	0.273	0.318	0.343	0.369	0.161	0.100

(d) Divergent Flap, $z = 1.595$ (Hill)

$p/p_{t,j}$ at x/x_t of

NPR	1.111	1.154	1.198	1.241	1.284	1.327	1.370	1.413	1.456	1.500	1.543	1.586	1.629	1.672	1.715	1.758	1.802	1.845	1.888	1.931	1.974
1.24	0.726	0.747	0.756	0.759	0.754	0.757	0.754	0.755	0.750	0.749	0.748	0.750	0.752	0.756	0.764	0.770	0.770	0.772	0.772	0.777	0.778
1.39	0.466	0.527	0.568	0.598	0.614	0.641	0.660	0.685	0.667	0.643	0.651	0.671	0.683	0.688	0.696	0.704	0.701	0.706	0.709	0.713	0.713
1.59	0.275	0.286	0.341	0.421	0.470	0.510	0.531	0.573	0.522	0.473	0.499	0.521	0.540	0.555	0.577	0.595	0.598	0.608	0.615	0.621	0.624
1.79	0.275	0.281	0.287	0.292	0.285	0.289	0.407	0.474	0.469	0.418	0.428	0.448	0.486	0.503	0.532	0.554	0.555	0.560	0.561	0.563	0.560
1.99	0.274	0.280	0.289	0.289	0.280	0.268	0.331	0.400	0.389	0.315	0.308	0.378	0.437	0.451	0.472	0.491	0.484	0.489	0.491	0.495	0.495
2.19	0.273	0.282	0.290	0.287	0.276	0.258	0.298	0.325	0.306	0.274	0.254	0.318	0.379	0.403	0.429	0.448	0.437	0.444	0.445	0.449	0.451
2.39	0.273	0.284	0.291	0.285	0.274	0.256	0.294	0.317	0.275	0.201	0.161	0.254	0.315	0.346	0.395	0.420	0.395	0.405	0.411	0.418	0.414
2.59	0.275	0.287	0.291	0.284	0.273	0.254	0.291	0.315	0.269	0.193	0.138	0.204	0.247	0.281	0.344	0.376	0.358	0.369	0.378	0.389	0.390
2.99	0.280	0.289	0.290	0.284	0.272	0.253	0.290	0.313	0.267	0.188	0.133	0.195	0.197	0.188	0.138	0.236	0.215	0.265	0.282	0.292	0.308
3.39	0.279	0.288	0.290	0.284	0.272	0.253	0.290	0.312	0.268	0.188	0.134	0.199	0.198	0.190	0.141	0.258	0.232	0.268	0.269	0.271	0.272
3.79	0.279	0.287	0.290	0.284	0.271	0.253	0.290	0.312	0.268	0.189	0.134	0.200	0.199	0.189	0.135	0.207	0.160	0.141	0.136	0.147	0.224
4.19	0.278	0.287	0.289	0.283	0.271	0.252	0.290	0.312	0.269	0.189	0.134	0.202	0.199	0.189	0.135	0.205	0.159	0.139	0.131	0.131	0.164
4.59	0.278	0.287	0.289	0.283	0.271	0.252	0.290	0.312	0.269	0.190	0.135	0.202	0.199	0.190	0.135	0.202	0.158	0.139	0.129	0.124	0.127
4.99	0.277	0.286	0.289	0.282	0.270	0.252	0.290	0.312	0.270	0.191	0.135	0.202	0.199	0.189	0.135	0.200	0.157	0.138	0.128	0.123	0.118
5.39	0.276	0.285	0.288	0.282	0.269	0.251	0.290	0.312	0.270	0.191	0.136	0.202	0.199	0.190	0.135	0.199	0.156	0.139	0.128	0.123	0.118
6.19	0.274	0.283	0.287	0.280	0.268	0.250	0.289	0.312	0.270	0.192	0.136	0.202	0.199	0.191	0.136	0.198	0.154	0.138	0.128	0.122	0.117
6.99	0.272	0.282	0.285	0.279	0.266	0.248	0.289	0.311	0.270	0.192	0.137	0.203	0.199	0.192	0.138	0.200	0.155	0.138	0.128	0.121	0.117
7.99	0.271	0.280	0.284	0.278	0.265	0.247	0.288	0.310	0.269	0.192	0.137	0.202	0.199	0.192	0.138	0.201	0.154	0.138	0.128	0.121	0.117
8.89	0.269	0.279	0.283	0.277	0.264	0.246	0.288	0.310	0.269	0.192	0.137	0.202	0.198	0.192	0.138	0.200	0.153	0.136	0.127	0.121	0.117
9.50	0.269	0.278	0.283	0.277	0.263	0.246	0.287	0.310	0.269	0.192	0.137	0.202	0.198	0.193	0.138	0.200	0.152	0.136	0.126	0.120	0.117

Table 5. Nozzle Internal Static Pressure Ratios for the Medium-Long Convoluted Configuration

(a) Convergent Flap, $z = 0.000$

$p/p_{t,j}$ at x/x_t of

NPR	0.330	0.440	0.550	0.659	0.769	0.890	1.000
1.25	0.961	0.949	0.929	0.903	0.857	0.684	0.443
1.40	0.958	0.946	0.926	0.900	0.852	0.675	0.422
1.60	0.958	0.945	0.926	0.898	0.849	0.670	0.371
1.80	0.957	0.945	0.927	0.898	0.850	0.670	0.368
2.00	0.958	0.945	0.927	0.899	0.850	0.670	0.367
2.20	0.958	0.945	0.927	0.898	0.850	0.670	0.367
2.40	0.958	0.945	0.928	0.898	0.850	0.670	0.366
2.60	0.958	0.945	0.928	0.899	0.850	0.670	0.366
3.00	0.958	0.945	0.928	0.899	0.850	0.670	0.367
3.40	0.958	0.945	0.928	0.899	0.849	0.670	0.367
3.80	0.958	0.945	0.928	0.899	0.850	0.670	0.367
4.20	0.958	0.945	0.928	0.899	0.849	0.670	0.367
4.60	0.958	0.945	0.927	0.899	0.848	0.670	0.366
5.00	0.958	0.945	0.927	0.898	0.848	0.669	0.365
5.40	0.958	0.944	0.927	0.898	0.847	0.669	0.364
6.19	0.957	0.943	0.926	0.897	0.846	0.668	0.363
7.00	0.957	0.943	0.925	0.896	0.845	0.666	0.361
8.00	0.956	0.942	0.924	0.895	0.844	0.665	0.359
8.89	0.955	0.942	0.923	0.894	0.843	0.665	0.358
9.51	0.955	0.942	0.923	0.894	0.842	0.665	0.357

(b) Divergent Flap, $z = 0.000$ (Hill)

$p/p_{t,j}$ at x/x_t of

NPR	1.111	1.154	1.198	1.241	1.284	1.327	1.370	1.413	1.456	1.500	1.543	1.586	1.629	1.672	1.715	1.758	1.802	1.845	1.888	1.931	1.974
1.25	0.621	0.663	0.688	0.707	0.724	0.737	0.745	0.740	0.742	0.746	0.752	0.758	0.763	0.769	0.774	0.780	0.784	0.790	0.793	0.796	0.799
1.40	0.547	0.572	0.584	0.595	0.603	0.607	0.618	0.607	0.610	0.615	0.620	0.629	0.636	0.644	0.651	0.659	0.666	0.674	0.683	0.689	0.713
1.60	0.504	0.528	0.539	0.546	0.551	0.553	0.560	0.553	0.554	0.555	0.557	0.560	0.562	0.565	0.567	0.570	0.571	0.573	0.576	0.578	0.624
1.80	0.267	0.277	0.295	0.269	0.299	0.295	0.298	0.238	0.260	0.370	0.365	0.373	0.422	0.489	0.533	0.553	0.564	0.571	0.571	0.573	0.554
2.00	0.268	0.281	0.294	0.268	0.299	0.297	0.290	0.239	0.204	0.187	0.244	0.293	0.294	0.301	0.328	0.382	0.441	0.489	0.514	0.524	0.499
2.20	0.269	0.284	0.295	0.269	0.300	0.299	0.284	0.239	0.205	0.178	0.175	0.202	0.231	0.251	0.262	0.283	0.313	0.356	0.405	0.437	0.453
2.40	0.270	0.284	0.295	0.270	0.301	0.300	0.279	0.239	0.205	0.179	0.176	0.182	0.194	0.214	0.194	0.251	0.300	0.319	0.342	0.368	0.415
2.60	0.271	0.285	0.295	0.271	0.302	0.301	0.275	0.240	0.206	0.179	0.176	0.181	0.185	0.181	0.191	0.219	0.262	0.296	0.311	0.331	0.383
3.00	0.272	0.285	0.295	0.271	0.302	0.301	0.269	0.242	0.207	0.180	0.178	0.183	0.186	0.179	0.171	0.186	0.234	0.264	0.281	0.290	0.332
3.40	0.271	0.285	0.295	0.272	0.301	0.301	0.265	0.242	0.207	0.181	0.178	0.183	0.186	0.179	0.164	0.157	0.143	0.185	0.226	0.254	0.293
3.80	0.271	0.285	0.294	0.272	0.301	0.302	0.262	0.243	0.208	0.181	0.178	0.184	0.186	0.180	0.165	0.154	0.123	0.120	0.134	0.207	0.262
4.20	0.270	0.285	0.294	0.272	0.301	0.302	0.260	0.243	0.209	0.181	0.179	0.184	0.187	0.181	0.165	0.155	0.124	0.120	0.119	0.144	0.237
4.60	0.269	0.284	0.293	0.271	0.301	0.302	0.258	0.243	0.209	0.181	0.179	0.185	0.187	0.181	0.166	0.156	0.124	0.121	0.120	0.144	0.216
5.00	0.269	0.283	0.293	0.271	0.301	0.302	0.257	0.243	0.209	0.182	0.180	0.185	0.188	0.182	0.167	0.156	0.125	0.121	0.120	0.145	0.199
5.40	0.268	0.282	0.292	0.271	0.300	0.301	0.256	0.243	0.209	0.182	0.180	0.186	0.188	0.182	0.167	0.157	0.126	0.122	0.121	0.146	0.184
6.19	0.266	0.281	0.290	0.269	0.299	0.300	0.253	0.243	0.209	0.182	0.180	0.186	0.188	0.182	0.168	0.158	0.127	0.122	0.122	0.147	0.161
7.00	0.264	0.279	0.288	0.268	0.298	0.299	0.251	0.242	0.209	0.181	0.180	0.187	0.189	0.183	0.169	0.158	0.127	0.122	0.122	0.148	0.142
8.00	0.262	0.277	0.287	0.266	0.297	0.298	0.249	0.242	0.209	0.181	0.180	0.187	0.189	0.184	0.170	0.159	0.128	0.123	0.122	0.149	0.125
8.89	0.261	0.276	0.285	0.265	0.296	0.297	0.248	0.241	0.209	0.181	0.180	0.187	0.189	0.184	0.170	0.160	0.128	0.123	0.123	0.149	0.112
9.51	0.260	0.276	0.284	0.265	0.295	0.297	0.247	0.241	0.209	0.181	0.180	0.188	0.189	0.184	0.170	0.160	0.128	0.123	0.123	0.150	0.105

Table 5. Concluded

(c) Divergent Flap, $z = 0.1995$ (Valley)

$p/p_{t,j}$ at x/x_t of

NPR	1.327	1.370	1.413	1.456	1.500	1.543	1.586	1.629	1.672	1.715
1.25	0.728	0.739	0.743	0.752	0.757	0.762	0.766	0.770	0.775	0.779
1.40	0.616	0.621	0.623	0.630	0.635	0.639	0.644	0.648	0.653	0.659
1.60	0.561	0.566	0.565	0.570	0.572	0.573	0.574	0.574	0.574	0.575
1.80	0.219	0.227	0.246	0.321	0.392	0.422	0.444	0.469	0.512	0.536
2.00	0.219	0.227	0.241	0.247	0.262	0.284	0.320	0.353	0.375	0.373
2.20	0.218	0.228	0.241	0.247	0.259	0.264	0.267	0.263	0.278	0.294
2.40	0.218	0.228	0.242	0.246	0.259	0.263	0.265	0.261	0.316	0.317
2.60	0.218	0.228	0.242	0.247	0.259	0.263	0.264	0.252	0.234	0.197
3.00	0.218	0.228	0.241	0.247	0.259	0.263	0.264	0.251	0.234	0.193
3.40	0.218	0.229	0.242	0.248	0.259	0.263	0.263	0.250	0.234	0.193
3.80	0.218	0.229	0.242	0.248	0.259	0.263	0.264	0.250	0.234	0.193
4.20	0.218	0.229	0.242	0.248	0.259	0.263	0.264	0.251	0.234	0.193
4.60	0.218	0.229	0.242	0.248	0.260	0.263	0.264	0.251	0.234	0.194
5.00	0.217	0.229	0.243	0.249	0.260	0.264	0.264	0.251	0.235	0.194
5.40	0.216	0.228	0.243	0.249	0.260	0.264	0.265	0.251	0.235	0.194
6.19	0.215	0.228	0.242	0.249	0.260	0.264	0.265	0.251	0.235	0.195
7.00	0.214	0.227	0.241	0.248	0.260	0.263	0.265	0.251	0.236	0.195
8.00	0.213	0.226	0.241	0.248	0.260	0.264	0.265	0.252	0.237	0.195
8.89	0.213	0.226	0.240	0.248	0.259	0.264	0.266	0.252	0.237	0.196
9.51	0.212	0.226	0.240	0.248	0.259	0.264	0.266	0.252	0.237	0.196

(d) Divergent Flap, $z = 1.595$ (Hill)

$p/p_{t,j}$ at x/x_t of

NPR	1.111	1.154	1.198	1.241	1.284	1.327	1.370	1.413	1.456	1.500	1.543	1.586	1.629	1.672	1.715	1.758	1.802	1.845	1.888	1.931	1.974
1.25	0.666	0.704	0.715	0.722	0.733	0.742	0.743	0.742	0.744	0.750	0.759	0.767	0.771	0.780	0.784	0.788	0.791	0.796	0.796	0.798	0.798
1.40	0.508	0.551	0.577	0.595	0.614	0.629	0.638	0.638	0.639	0.642	0.649	0.655	0.659	0.669	0.673	0.679	0.685	0.693	0.699	0.704	0.706
1.60	0.499	0.520	0.531	0.539	0.545	0.550	0.554	0.554	0.557	0.561	0.563	0.567	0.567	0.572	0.573	0.576	0.577	0.581	0.588	0.594	0.588
1.80	0.268	0.279	0.303	0.283	0.327	0.335	0.305	0.289	0.407	0.470	0.483	0.487	0.492	0.503	0.508	0.517	0.530	0.543	0.548	0.557	0.557
2.00	0.267	0.281	0.302	0.281	0.325	0.332	0.305	0.297	0.318	0.322	0.371	0.401	0.432	0.454	0.460	0.467	0.479	0.489	0.490	0.497	0.496
2.20	0.269	0.282	0.303	0.278	0.316	0.306	0.278	0.264	0.223	0.270	0.293	0.327	0.384	0.403	0.405	0.413	0.429	0.443	0.446	0.455	0.451
2.40	0.270	0.285	0.303	0.277	0.314	0.303	0.272	0.248	0.215	0.192	0.210	0.267	0.274	0.336	0.361	0.368	0.387	0.403	0.406	0.426	0.419
2.60	0.273	0.291	0.304	0.277	0.313	0.303	0.271	0.245	0.210	0.183	0.183	0.194	0.245	0.243	0.260	0.309	0.342	0.362	0.368	0.395	0.389
3.00	0.277	0.294	0.304	0.277	0.312	0.303	0.270	0.243	0.209	0.180	0.176	0.181	0.185	0.183	0.172	0.182	0.242	0.273	0.298	0.317	0.331
3.40	0.278	0.294	0.304	0.278	0.312	0.303	0.271	0.243	0.210	0.180	0.176	0.181	0.184	0.181	0.168	0.159	0.128	0.154	0.209	0.275	0.295
3.80	0.278	0.294	0.304	0.278	0.313	0.303	0.271	0.244	0.210	0.181	0.177	0.181	0.184	0.181	0.168	0.159	0.127	0.126	0.131	0.157	0.208
4.20	0.277	0.294	0.304	0.278	0.313	0.303	0.271	0.245	0.211	0.181	0.177	0.182	0.185	0.181	0.169	0.159	0.128	0.126	0.130	0.157	0.155
4.60	0.277	0.293	0.304	0.277	0.313	0.303	0.271	0.245	0.211	0.182	0.178	0.182	0.185	0.181	0.169	0.159	0.128	0.126	0.129	0.156	0.141
5.00	0.276	0.293	0.303	0.277	0.313	0.303	0.271	0.244	0.211	0.182	0.178	0.182	0.185	0.182	0.170	0.160	0.129	0.126	0.129	0.153	0.135
5.40	0.275	0.292	0.303	0.276	0.313	0.303	0.271	0.245	0.211	0.182	0.179	0.183	0.186	0.182	0.170	0.160	0.130	0.127	0.130	0.151	0.129
6.19	0.273	0.291	0.301	0.275	0.312	0.302	0.271	0.245	0.212	0.182	0.179	0.184	0.187	0.183	0.171	0.161	0.131	0.128	0.131	0.150	0.125
7.00	0.271	0.288	0.300	0.272	0.310	0.300	0.270	0.244	0.211	0.183	0.179	0.185	0.187	0.184	0.171	0.163	0.132	0.131	0.133	0.153	0.124
8.00	0.269	0.287	0.298	0.271	0.309	0.298	0.270	0.244	0.211	0.182	0.180	0.185	0.188	0.184	0.172	0.163	0.132	0.131	0.133	0.152	0.124
8.89	0.268	0.286	0.297	0.270	0.308	0.297	0.269	0.244	0.211	0.182	0.180	0.185	0.188	0.185	0.172	0.163	0.132	0.131	0.132	0.151	0.123
9.51	0.268	0.285	0.297	0.269	0.307	0.297	0.269	0.243	0.210	0.182	0.180	0.185	0.188	0.185	0.172	0.163	0.132	0.131	0.132	0.150	0.122

Table 6. Nozzle Internal Static Pressure Ratios for the Coarse Convoluted Configuration

(a) Convergent Flap, $z = 0.000$

$p/p_{t,j}$ at x/x_t of

NPR	0.330	0.440	0.550	0.659	0.769	0.890	1.000
1.25	0.960	0.949	0.928	0.904	0.857	0.682	0.455
1.40	0.959	0.946	0.926	0.900	0.852	0.674	0.441
1.60	0.959	0.945	0.926	0.900	0.851	0.671	0.385
1.80	0.958	0.946	0.926	0.900	0.850	0.670	0.368
2.00	0.959	0.945	0.927	0.900	0.850	0.671	0.368
2.20	0.959	0.946	0.927	0.900	0.850	0.671	0.368
2.40	0.959	0.946	0.928	0.900	0.851	0.671	0.367
2.60	0.959	0.946	0.928	0.901	0.851	0.671	0.367
3.00	0.959	0.946	0.928	0.900	0.851	0.671	0.367
3.39	0.959	0.946	0.928	0.900	0.850	0.671	0.367
3.80	0.959	0.945	0.928	0.900	0.849	0.670	0.367
4.20	0.958	0.945	0.928	0.899	0.849	0.670	0.367
4.60	0.958	0.945	0.928	0.899	0.848	0.670	0.366
4.99	0.958	0.945	0.927	0.899	0.848	0.669	0.366
5.40	0.958	0.945	0.926	0.898	0.847	0.669	0.365
6.20	0.957	0.944	0.926	0.897	0.846	0.667	0.363
6.99	0.957	0.943	0.925	0.896	0.845	0.666	0.361
8.00	0.956	0.943	0.924	0.895	0.844	0.665	0.359
8.89	0.956	0.942	0.923	0.894	0.843	0.665	0.358
9.50	0.955	0.942	0.922	0.894	0.842	0.665	0.357

(b) Divergent Flap, $z = 0.000$ (Hill)

$p/p_{t,j}$ at x/x_t of

NPR	1.111	1.154	1.198	1.241	1.284	1.327	1.370	1.413	1.456	1.500	1.543	1.586	1.629	1.672	1.715	1.758	1.802	1.845	1.888	1.931	1.974
1.25	0.621	0.659	0.684	0.706	0.723	0.742	0.762	0.798	0.760	0.699	0.704	0.756	0.760	0.764	0.770	0.775	0.780	0.784	0.788	0.793	0.795
1.40	0.560	0.580	0.593	0.603	0.613	0.622	0.627	0.643	0.644	0.629	0.637	0.650	0.656	0.662	0.668	0.672	0.676	0.680	0.684	0.687	0.684
1.60	0.500	0.519	0.530	0.540	0.546	0.553	0.552	0.553	0.556	0.559	0.565	0.571	0.579	0.584	0.585	0.586	0.586	0.586	0.586	0.587	0.582
1.80	0.273	0.281	0.283	0.282	0.276	0.283	0.465	0.597	0.384	0.309	0.397	0.386	0.385	0.414	0.454	0.488	0.514	0.532	0.545	0.553	0.557
2.00	0.273	0.282	0.284	0.282	0.276	0.281	0.443	0.574	0.368	0.210	0.312	0.313	0.335	0.344	0.372	0.424	0.436	0.437	0.444	0.454	0.472
2.20	0.274	0.282	0.283	0.282	0.277	0.280	0.425	0.547	0.351	0.180	0.228	0.258	0.272	0.273	0.294	0.346	0.395	0.410	0.412	0.418	0.435
2.40	0.275	0.282	0.284	0.283	0.277	0.281	0.424	0.546	0.349	0.172	0.196	0.246	0.250	0.243	0.251	0.272	0.310	0.342	0.367	0.386	0.402
2.60	0.275	0.283	0.285	0.284	0.277	0.281	0.423	0.545	0.349	0.172	0.206	0.247	0.251	0.239	0.240	0.248	0.272	0.299	0.323	0.345	0.362
3.00	0.276	0.283	0.285	0.283	0.277	0.281	0.421	0.545	0.350	0.171	0.161	0.236	0.234	0.225	0.221	0.222	0.235	0.252	0.269	0.288	0.300
3.39	0.276	0.282	0.284	0.282	0.276	0.281	0.420	0.545	0.350	0.172	0.139	0.225	0.216	0.209	0.211	0.211	0.218	0.230	0.243	0.258	0.265
3.80	0.275	0.282	0.283	0.281	0.276	0.281	0.420	0.545	0.351	0.173	0.134	0.216	0.200	0.189	0.198	0.204	0.206	0.214	0.223	0.234	0.241
4.20	0.275	0.281	0.283	0.281	0.276	0.281	0.420	0.546	0.351	0.174	0.133	0.204	0.173	0.160	0.140	0.154	0.169	0.181	0.194	0.207	0.221
4.60	0.274	0.280	0.282	0.280	0.275	0.281	0.420	0.546	0.351	0.175	0.134	0.202	0.172	0.159	0.130	0.136	0.131	0.141	0.158	0.172	0.195
4.99	0.273	0.280	0.282	0.280	0.275	0.281	0.420	0.547	0.351	0.175	0.134	0.202	0.173	0.161	0.130	0.137	0.126	0.127	0.140	0.139	0.165
5.40	0.272	0.279	0.281	0.279	0.275	0.281	0.420	0.547	0.352	0.176	0.134	0.201	0.174	0.162	0.131	0.137	0.127	0.127	0.138	0.129	0.133
6.20	0.270	0.277	0.279	0.278	0.273	0.280	0.419	0.547	0.352	0.177	0.135	0.200	0.175	0.163	0.133	0.139	0.127	0.128	0.139	0.125	0.119
6.99	0.269	0.275	0.278	0.276	0.272	0.278	0.418	0.548	0.352	0.177	0.136	0.199	0.176	0.164	0.134	0.140	0.128	0.129	0.139	0.125	0.117
8.00	0.267	0.273	0.276	0.274	0.271	0.277	0.418	0.547	0.352	0.177	0.136	0.198	0.177	0.165	0.134	0.140	0.129	0.129	0.139	0.125	0.115
8.89	0.265	0.272	0.275	0.273	0.270	0.276	0.417	0.548	0.352	0.178	0.137	0.197	0.178	0.165	0.135	0.141	0.129	0.129	0.140	0.125	0.114
9.50	0.265	0.271	0.274	0.273	0.269	0.276	0.417	0.548	0.352	0.178	0.137	0.196	0.178	0.165	0.135	0.141	0.129	0.130	0.140	0.125	0.114

Table 6. Concluded

(c) Divergent Flap, z = 0.1995 (Valley)

$p/p_{t,j}$ at x/x_t of

NPR	1.327	1.370	1.413	1.456	1.500	1.543	1.586	1.629	1.672	1.715
1.25	0.729	0.736	0.748	0.751	0.755	0.761	0.765	0.772	0.769	0.770
1.40	0.627	0.633	0.648	0.663	0.666	0.667	0.666	0.664	0.658	0.664
1.60	0.557	0.559	0.575	0.590	0.592	0.592	0.589	0.586	0.578	0.582
1.80	0.286	0.376	0.377	0.377	0.373	0.372	0.378	0.412	0.475	0.461
2.00	0.250	0.292	0.308	0.320	0.339	0.360	0.388	0.457	0.490	0.363
2.20	0.249	0.255	0.272	0.292	0.320	0.358	0.409	0.501	0.445	0.270
2.40	0.249	0.241	0.258	0.279	0.315	0.360	0.422	0.527	0.410	0.212
2.60	0.249	0.238	0.254	0.275	0.314	0.361	0.424	0.530	0.398	0.189
3.00	0.249	0.235	0.251	0.272	0.311	0.362	0.427	0.529	0.382	0.163
3.39	0.249	0.235	0.251	0.270	0.309	0.361	0.429	0.531	0.374	0.149
3.80	0.249	0.235	0.250	0.269	0.308	0.360	0.429	0.534	0.367	0.137
4.20	0.249	0.235	0.249	0.268	0.308	0.361	0.429	0.536	0.362	0.117
4.60	0.248	0.234	0.249	0.269	0.310	0.362	0.429	0.537	0.361	0.116
4.99	0.248	0.234	0.249	0.269	0.311	0.363	0.428	0.537	0.361	0.117
5.40	0.248	0.234	0.248	0.270	0.312	0.363	0.427	0.537	0.361	0.117
6.20	0.247	0.233	0.248	0.270	0.312	0.362	0.425	0.538	0.361	0.117
6.99	0.245	0.233	0.247	0.270	0.313	0.361	0.423	0.538	0.360	0.118
8.00	0.244	0.233	0.247	0.270	0.313	0.360	0.422	0.539	0.360	0.118
8.89	0.244	0.232	0.247	0.270	0.312	0.359	0.422	0.540	0.360	0.118
9.50	0.243	0.232	0.247	0.270	0.312	0.358	0.422	0.541	0.359	0.118

(d) Divergent Flap, z = 1.595 (Hill)

$p/p_{t,j}$ at x/x_t of

NPR	1.111	1.154	1.198	1.241	1.284	1.327	1.370	1.413	1.456	1.500	1.543	1.586	1.629	1.672	1.715	1.758	1.802	1.845	1.888	1.931	1.974
1.25	0.645	0.676	0.694	0.711	0.727	0.758	0.794	0.827	0.753	0.697	0.694	0.765	0.763	0.760	0.767	0.774	0.779	0.786	0.788	0.793	0.795
1.40	0.556	0.583	0.598	0.612	0.623	0.635	0.645	0.667	0.662	0.631	0.637	0.662	0.664	0.669	0.672	0.676	0.678	0.683	0.687	0.692	0.685
1.60	0.492	0.516	0.530	0.541	0.548	0.556	0.560	0.570	0.574	0.563	0.567	0.576	0.580	0.584	0.585	0.587	0.590	0.594	0.596	0.601	0.591
1.80	0.274	0.291	0.289	0.291	0.285	0.364	0.488	0.650	0.495	0.347	0.365	0.417	0.436	0.465	0.503	0.535	0.546	0.553	0.555	0.558	0.557
2.00	0.272	0.289	0.289	0.289	0.279	0.292	0.440	0.556	0.379	0.211	0.332	0.330	0.343	0.359	0.380	0.420	0.441	0.456	0.467	0.478	0.486
2.20	0.273	0.287	0.288	0.289	0.280	0.290	0.442	0.557	0.398	0.251	0.244	0.305	0.327	0.342	0.362	0.407	0.431	0.443	0.449	0.452	0.454
2.40	0.276	0.288	0.288	0.289	0.279	0.288	0.427	0.532	0.368	0.190	0.199	0.226	0.250	0.256	0.274	0.351	0.389	0.399	0.400	0.400	0.400
2.60	0.280	0.290	0.290	0.289	0.279	0.287	0.423	0.523	0.364	0.186	0.144	0.220	0.226	0.219	0.233	0.281	0.337	0.361	0.366	0.369	0.371
3.00	0.284	0.291	0.290	0.288	0.278	0.286	0.419	0.520	0.361	0.180	0.121	0.219	0.207	0.190	0.204	0.220	0.246	0.275	0.294	0.311	0.322
3.39	0.283	0.291	0.290	0.288	0.278	0.286	0.418	0.519	0.360	0.179	0.129	0.223	0.210	0.196	0.204	0.208	0.219	0.233	0.245	0.259	0.273
3.80	0.282	0.291	0.290	0.288	0.277	0.285	0.418	0.519	0.360	0.179	0.125	0.221	0.208	0.193	0.201	0.201	0.204	0.212	0.221	0.233	0.239
4.20	0.282	0.290	0.290	0.288	0.278	0.286	0.418	0.519	0.361	0.180	0.116	0.213	0.184	0.161	0.161	0.175	0.184	0.192	0.199	0.209	0.218
4.60	0.282	0.290	0.290	0.287	0.277	0.286	0.419	0.519	0.361	0.180	0.114	0.211	0.177	0.148	0.129	0.135	0.147	0.164	0.174	0.184	0.196
4.99	0.281	0.290	0.290	0.287	0.277	0.286	0.419	0.519	0.361	0.181	0.114	0.210	0.177	0.147	0.126	0.128	0.127	0.140	0.154	0.164	0.183
5.40	0.281	0.289	0.289	0.287	0.277	0.285	0.419	0.519	0.362	0.181	0.114	0.209	0.178	0.148	0.127	0.128	0.124	0.133	0.140	0.144	0.160
6.20	0.279	0.288	0.287	0.286	0.276	0.285	0.419	0.519	0.362	0.182	0.115	0.208	0.180	0.150	0.128	0.129	0.123	0.130	0.134	0.129	0.126
6.99	0.277	0.286	0.286	0.285	0.275	0.284	0.418	0.519	0.362	0.182	0.115	0.208	0.181	0.151	0.129	0.130	0.123	0.130	0.133	0.126	0.119
8.00	0.276	0.285	0.284	0.283	0.274	0.284	0.418	0.519	0.362	0.183	0.115	0.206	0.183	0.154	0.130	0.131	0.123	0.130	0.133	0.124	0.118
8.89	0.274	0.283	0.283	0.282	0.273	0.283	0.418	0.520	0.363	0.183	0.115	0.204	0.185	0.159	0.133	0.134	0.124	0.131	0.135	0.124	0.116
9.50	0.274	0.283	0.282	0.281	0.272	0.283	0.418	0.520	0.363	0.183	0.116	0.203	0.186	0.161	0.134	0.135	0.125	0.132	0.136	0.123	0.115

Table 7. Measured Peak Thrust Ratio $(F/F_i)_{peak}$ at NPR=8.9

Configuration	$(F/F_i)_{peak}$
Baseline	0.986
Fine convoluted	0.980
Medium convoluted	0.976
Medium-long convoluted	0.980
Coarse convoluted	0.957

Table 8. Wetted Area, Skin Friction Drag Penalties $\Delta(F/F_i)_f$, and Peak Thrust Ratio $(F/F_i)_{peak}$

Configuration	Wetted Area, in^2	Estimated $\Delta(F/F_i)_f$	Predicted $(F/F_i)peak$	Measured $(F/F_i)peak$
Baseline	52.400	0.0075	0.986	0.986
Fine convoluted	60.206	0.0092	0.984	0.980
Medium convoluted	60.206	0.0092	0.984	0.976
Medium-long convoluted	65.965	0.0105	0.983	0.980
Coarse convoluted	60.206	0.0092	0.984	0.957

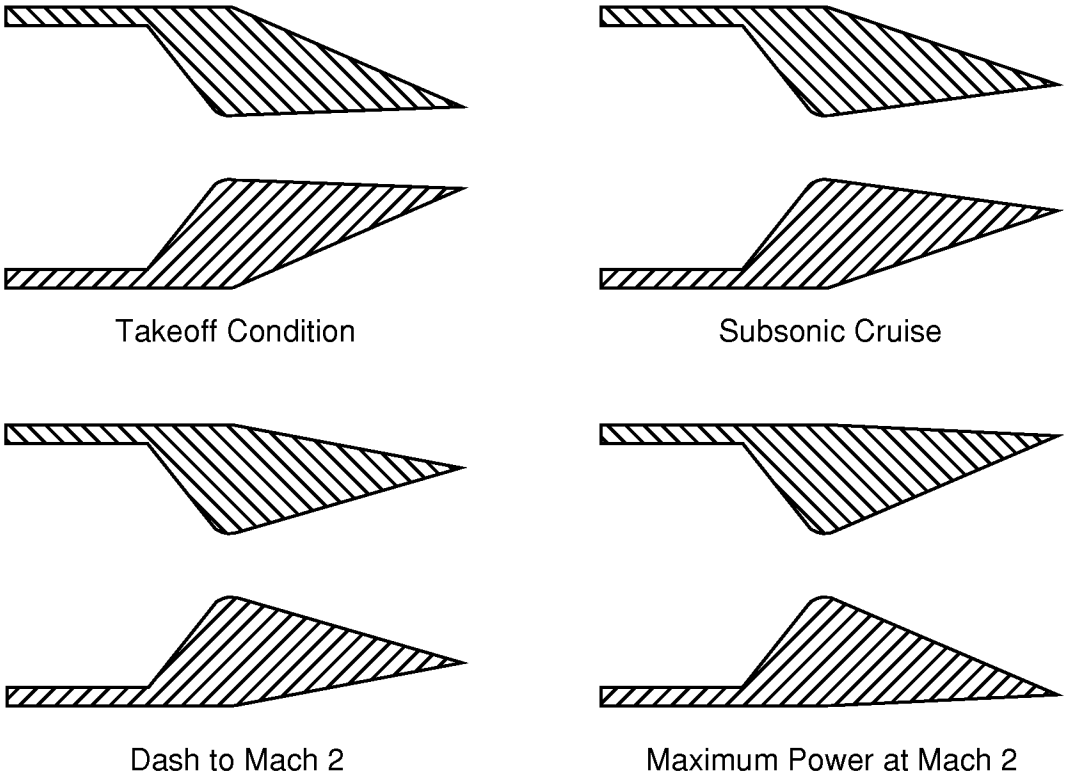

Figure 1. Sketch showing a typical variable geometry nozzle over several operating conditions.

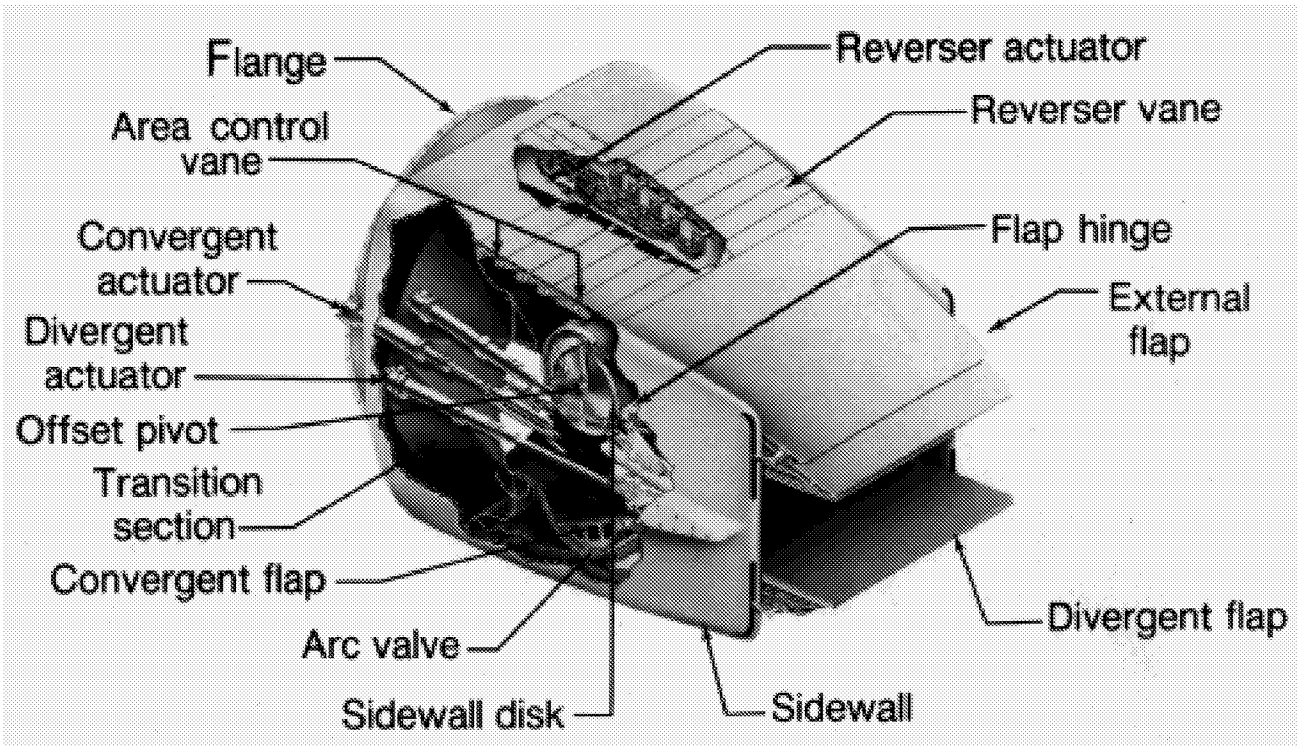

Figure 2. Sketch showing a typical variable geometry nonaxisymmetric exhaust nozzle.

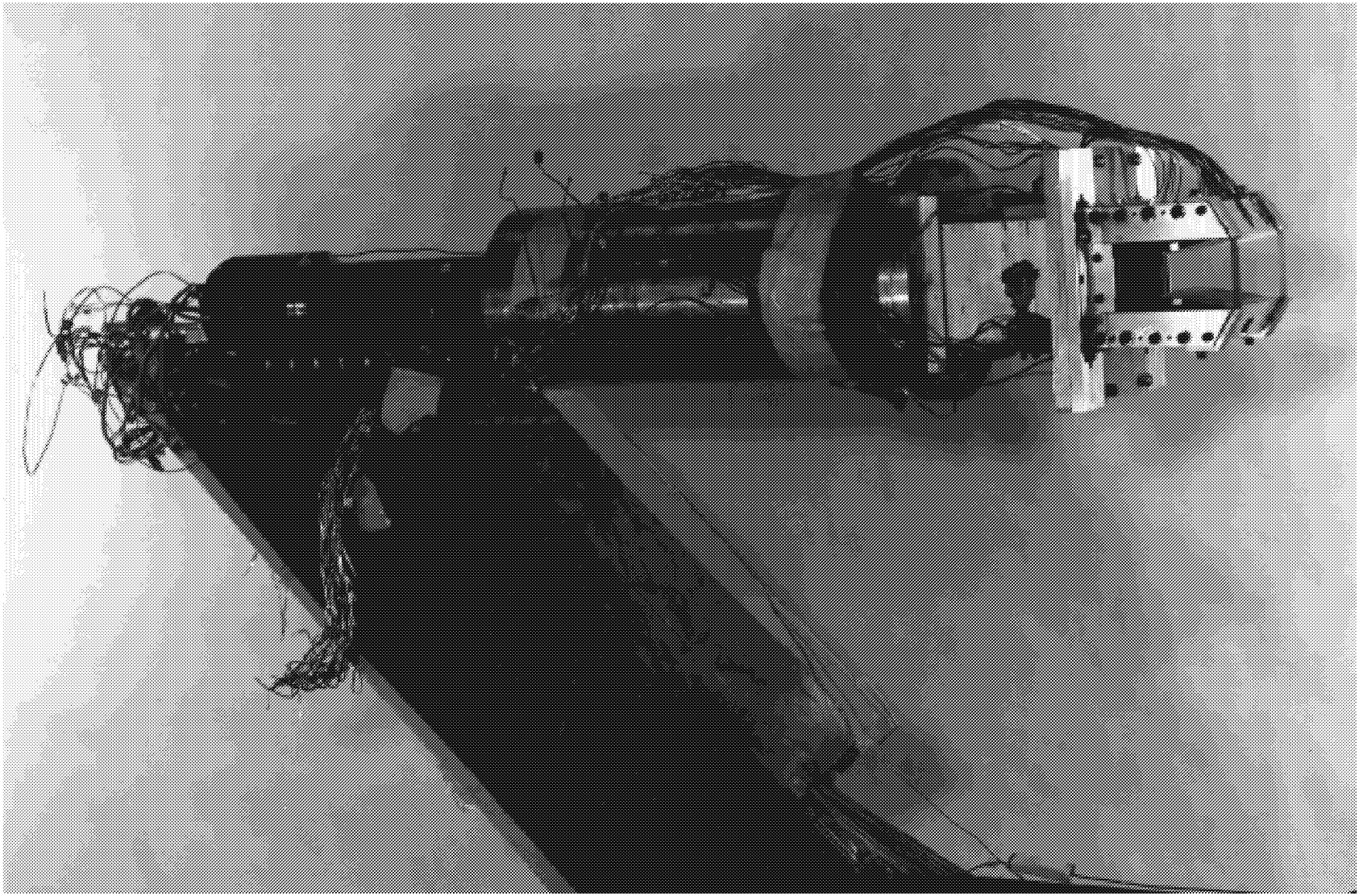

(a) Photograph of the propulsion simulation system with a typical nozzle configuration installed.

Figure 3. Details of the single-engine propulsion simulation system.

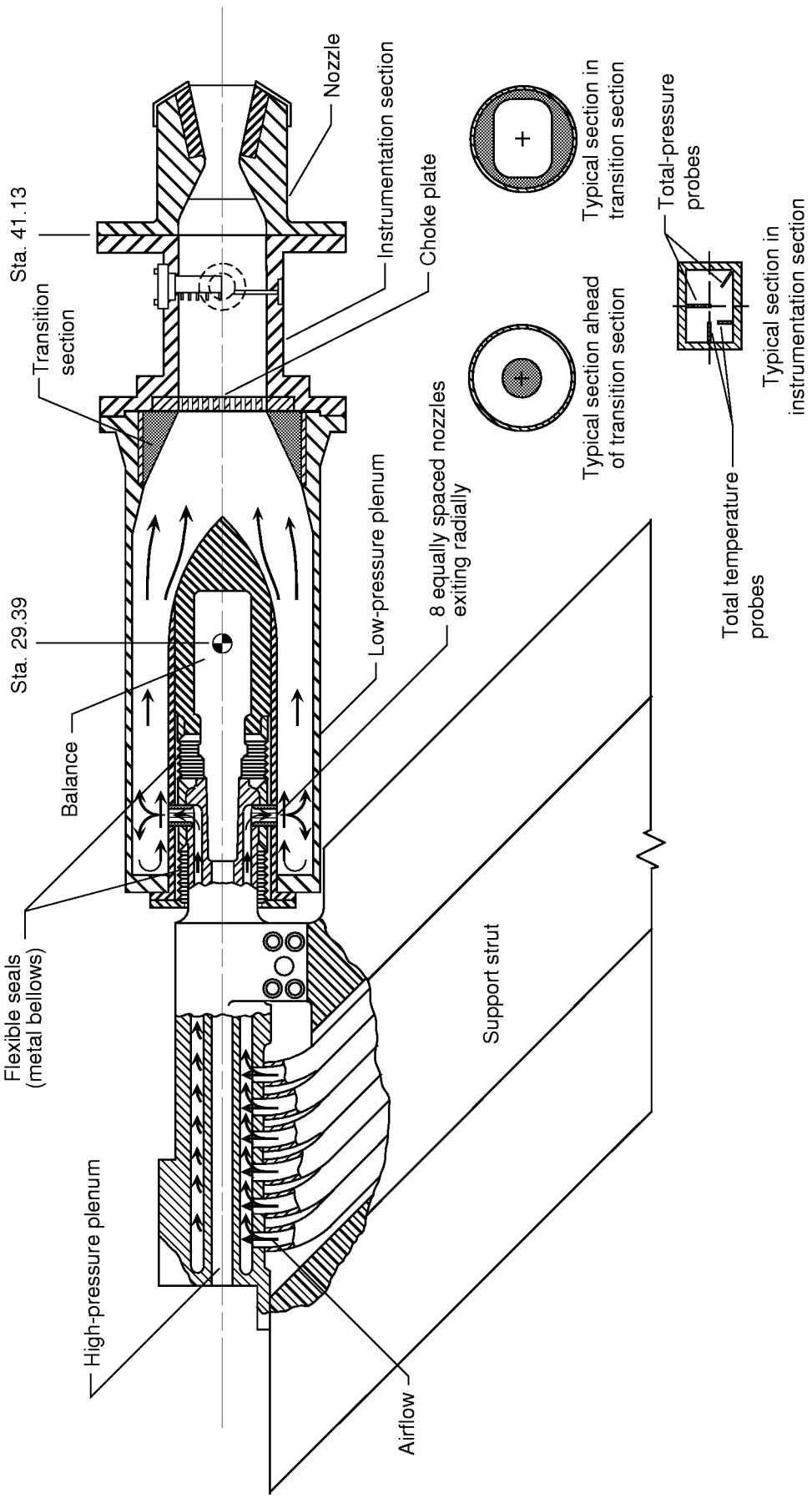

(b) Sketch of the propulsion simulation system. Station numbers are in inches.

Figure 3. Concluded.

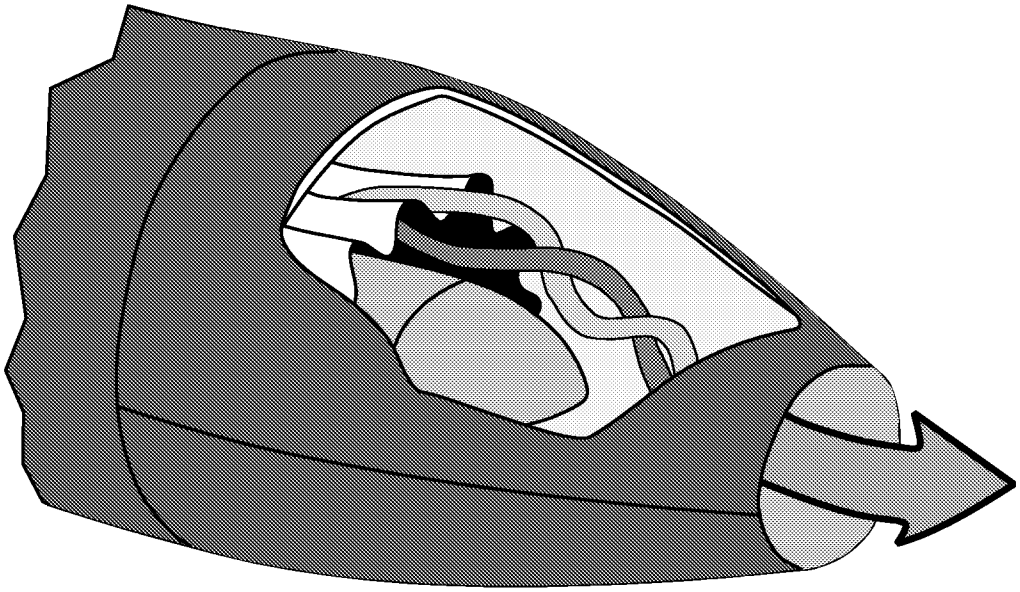

Figure 4. Partial cutaway sketch of a typical turbofan forced mixer.

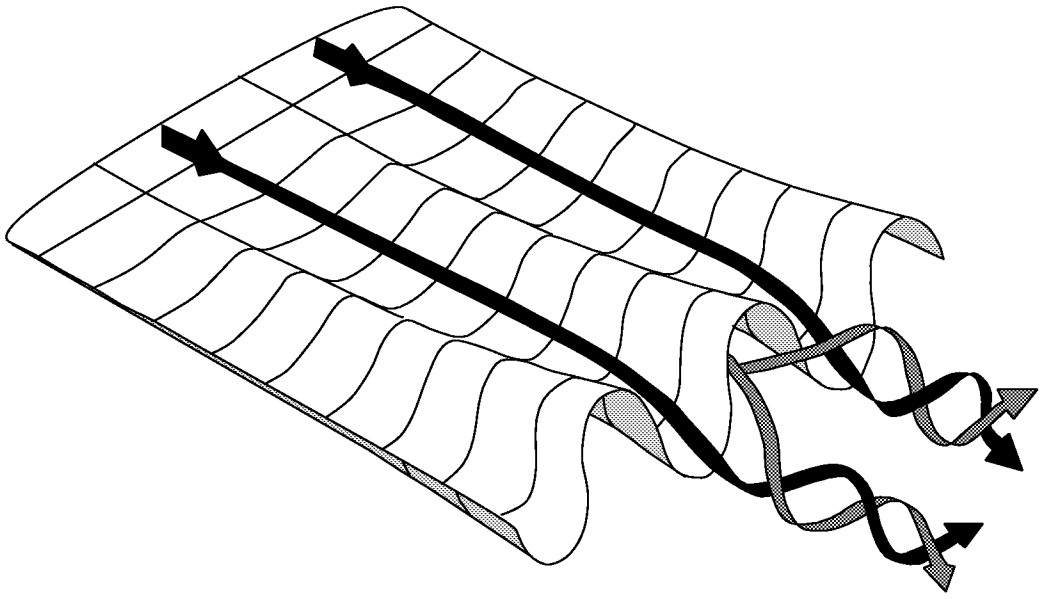

Figure 5. Sketch showing streamwise vorticity generated by a convoluted mixer.

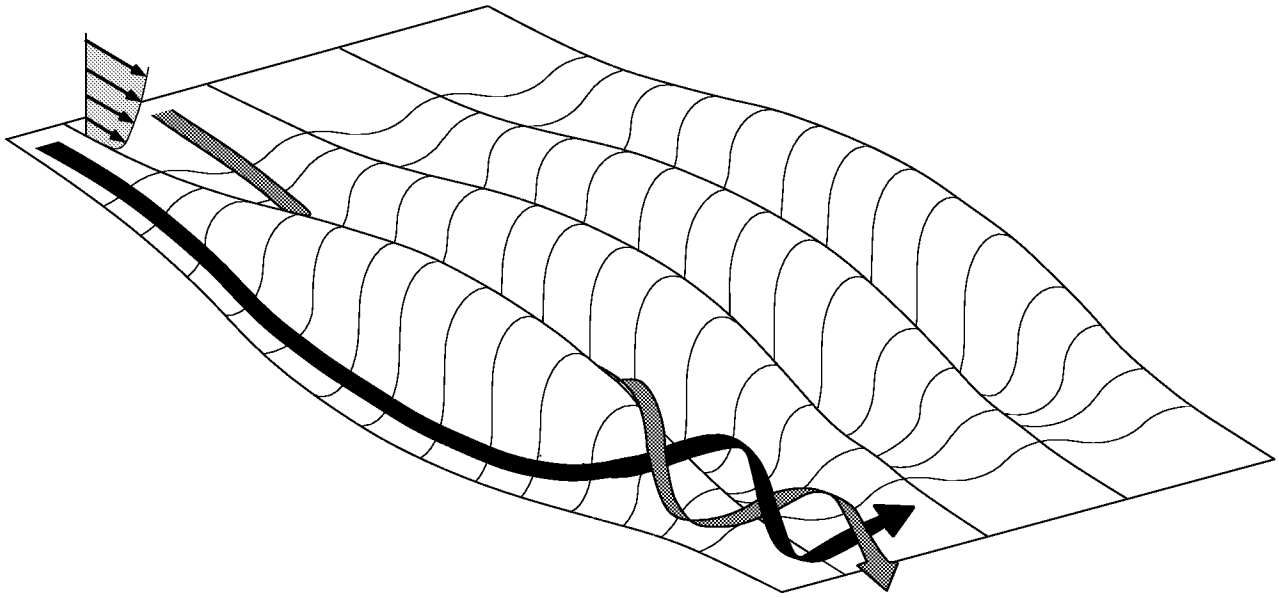

Figure 6. Sketch showing "bump" type convoluted contouring used in this investigation.

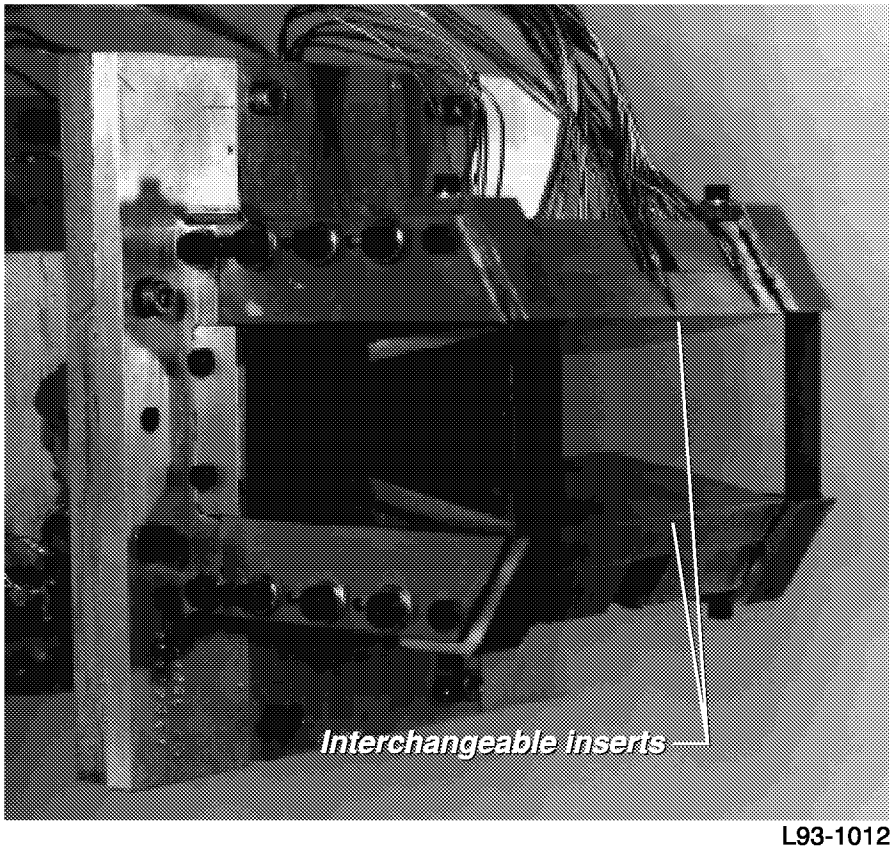

Figure 7. Photograph of the static test model with baseline flap inserts installed.

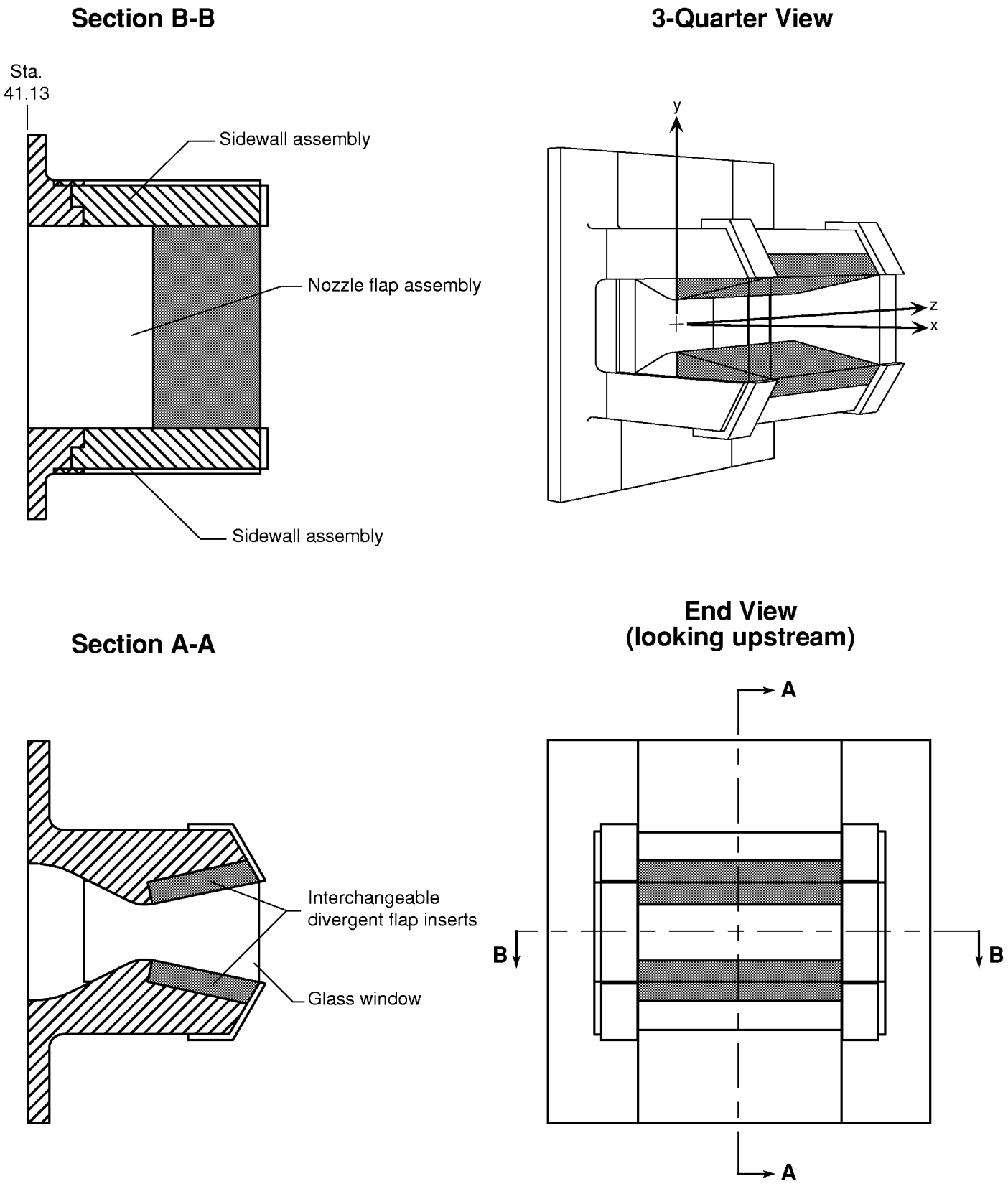

Figure 8. Sketch of nozzle model with baseline flap inserts (shaded) installed.

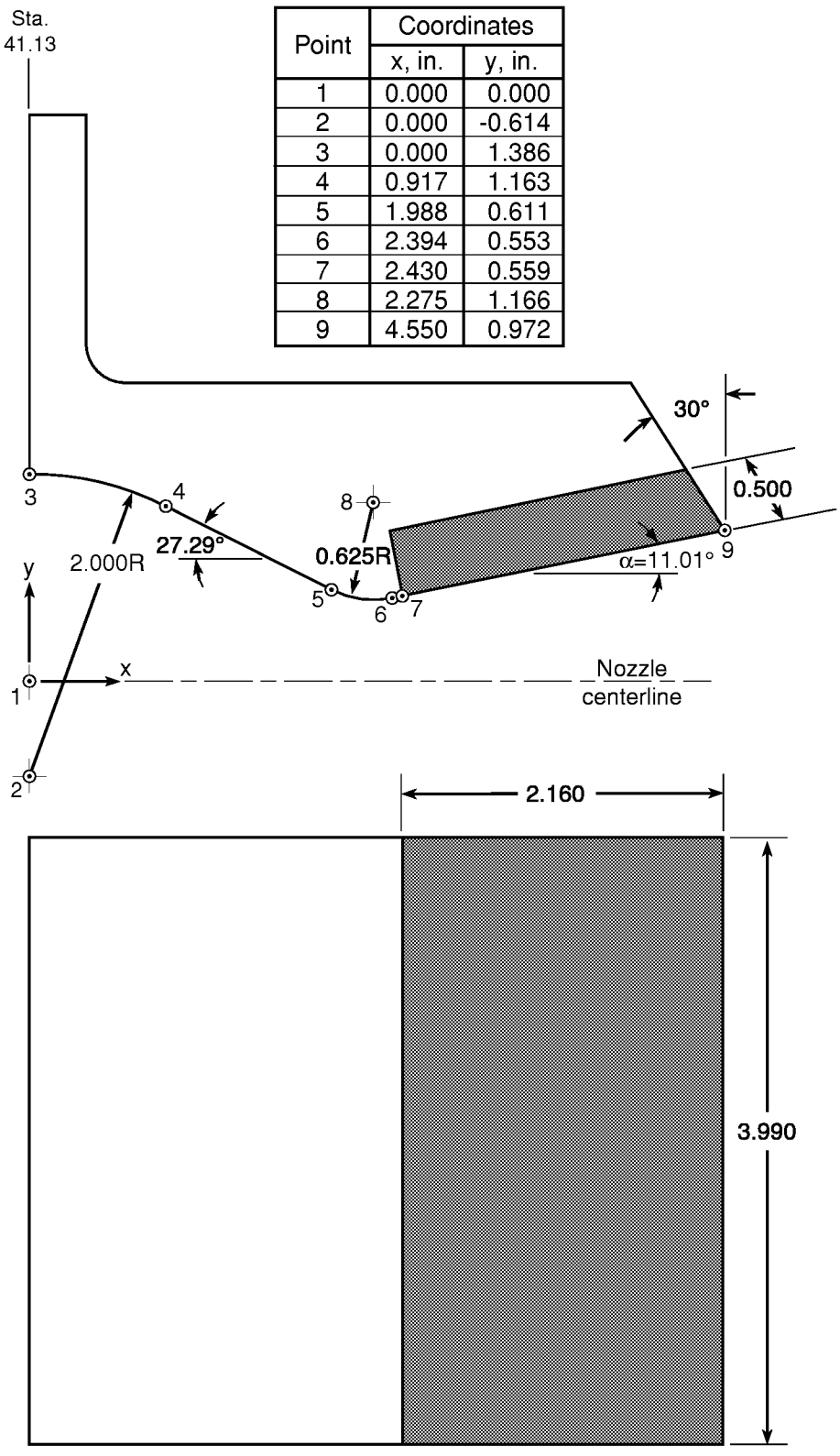

Point	Coordinates	
	x, in.	y, in.
1	0.000	0.000
2	0.000	-0.614
3	0.000	1.386
4	0.917	1.163
5	1.988	0.611
6	2.394	0.553
7	2.430	0.559
8	2.275	1.166
9	4.550	0.972

(a) Nozzle flap assembly.

Figure 9. Sketch showing nozzle geometric details. Dimensions are in inches.

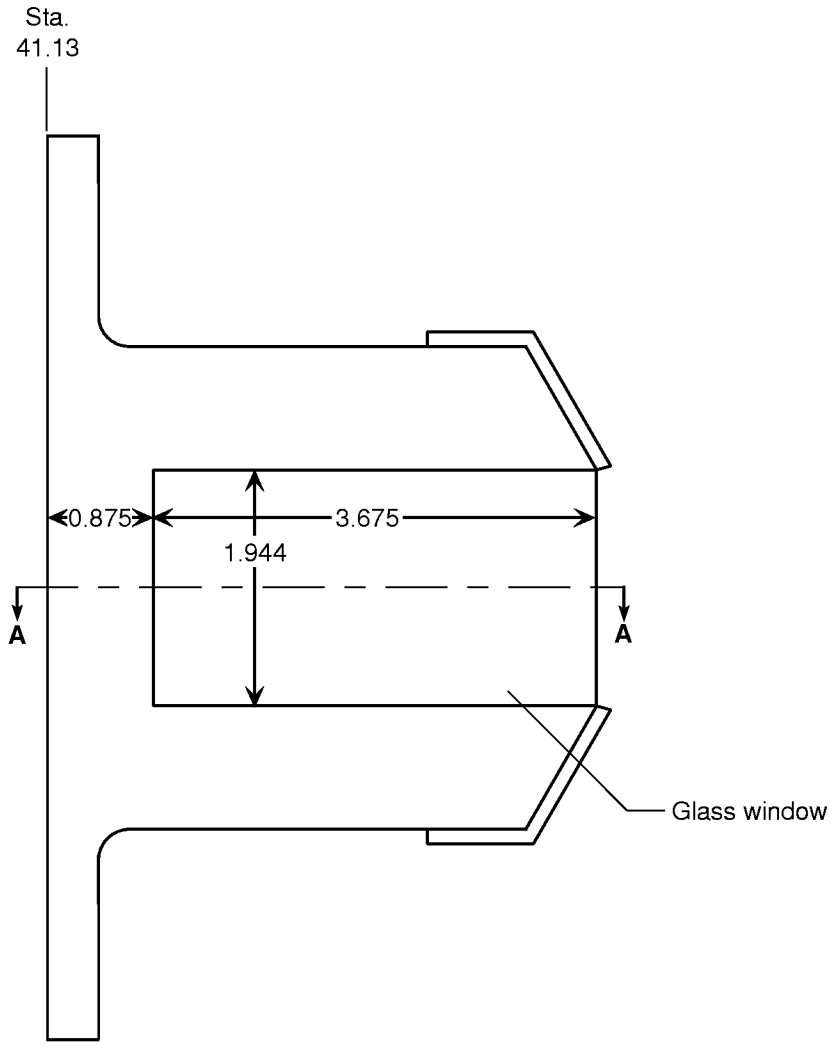

Section A-A

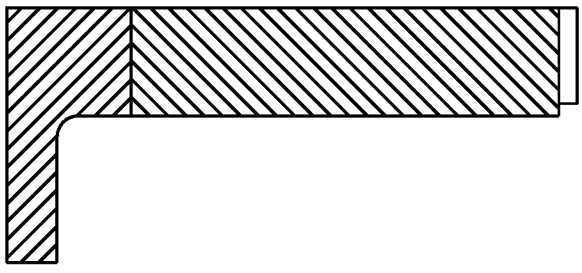

(b) Sidewall assembly.

Figure 9. Concluded.

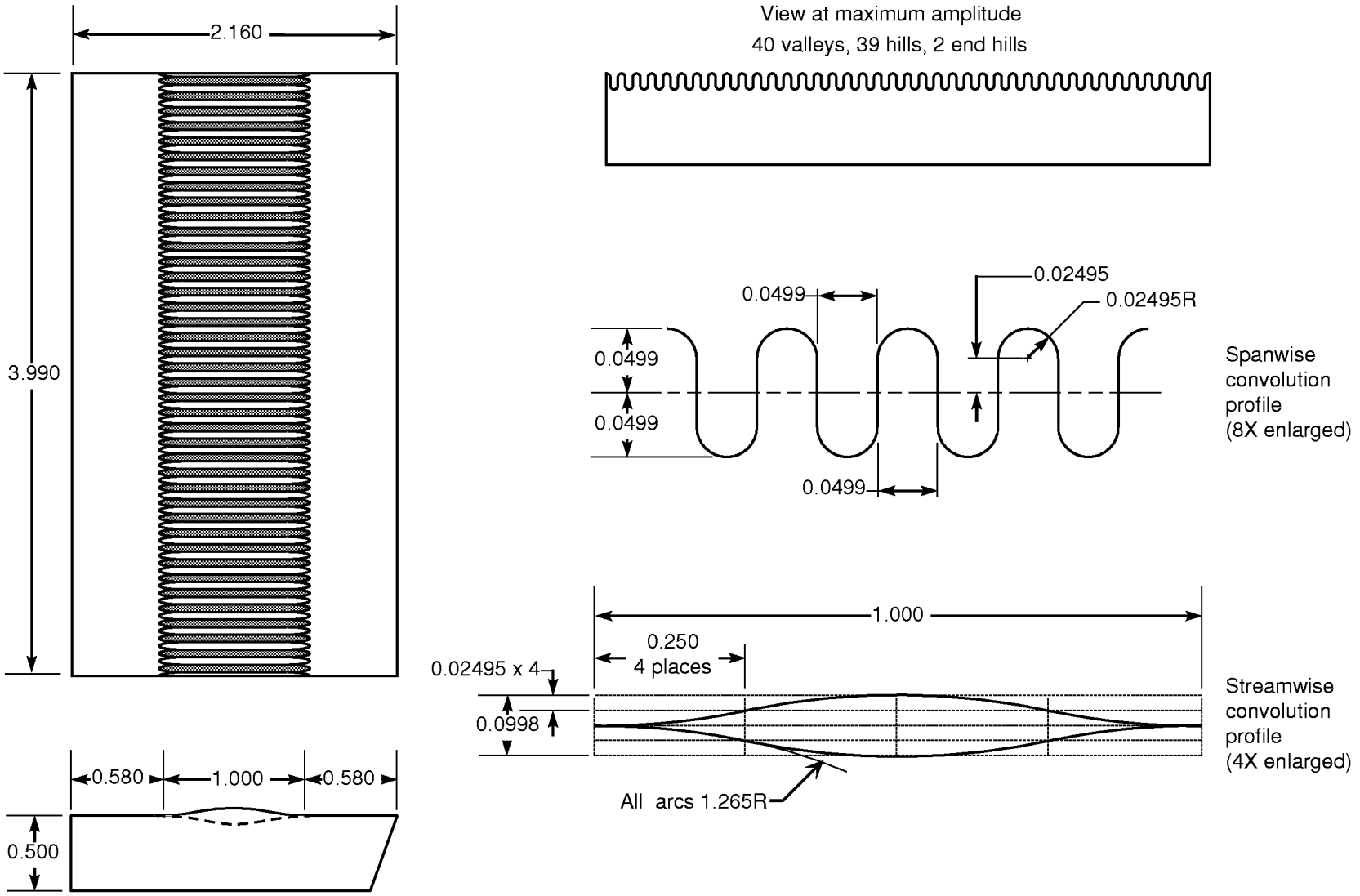

(a) Fine convoluted flap inserts.

Figure 10. Details of convoluted flap inserts. Dimensions are in inches.

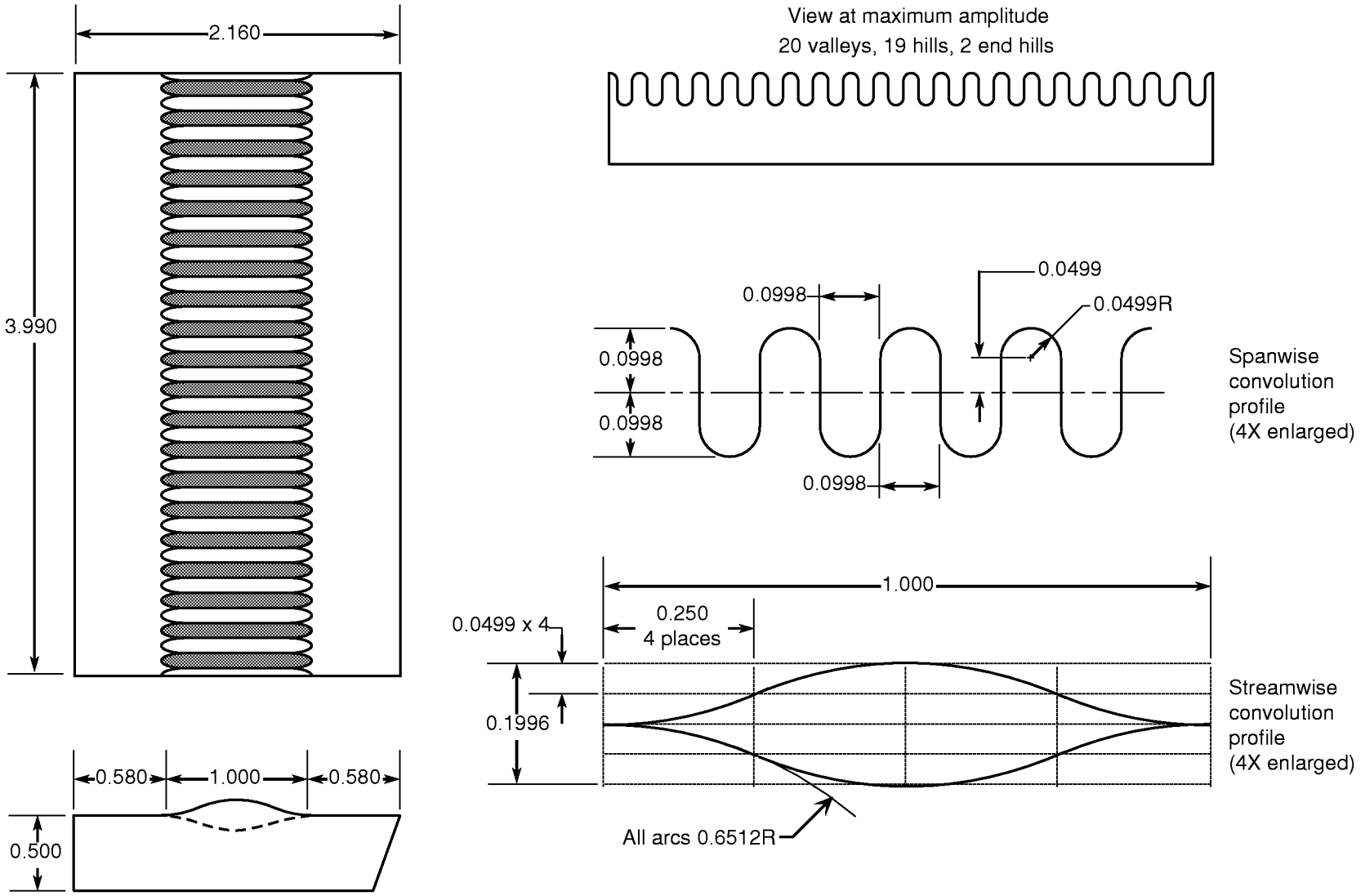

(b) Medium convoluted flap inserts.

Figure 10. Continued.

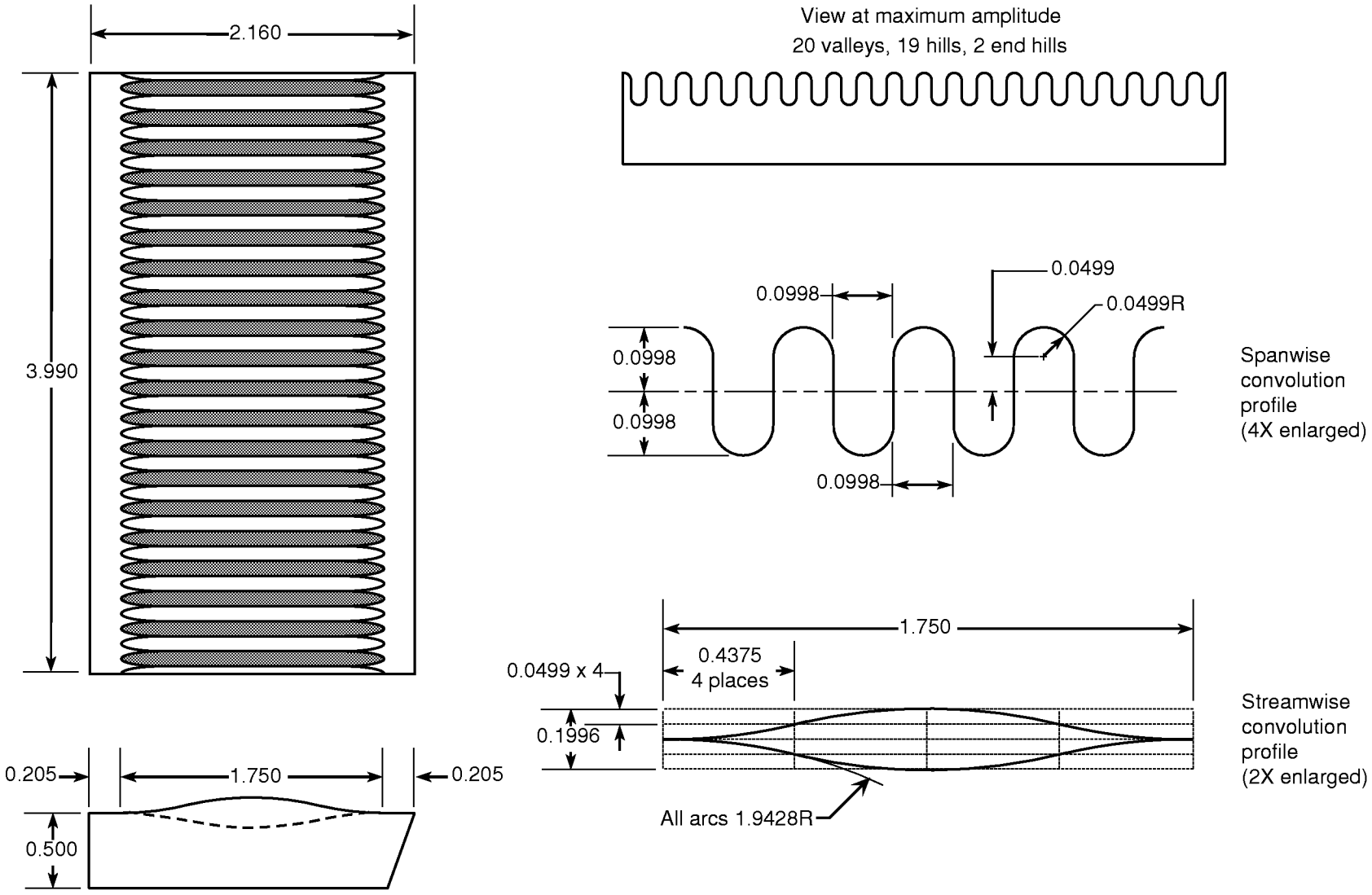

(c) Medium-long convoluted flap inserts.

Figure 10. Continued.

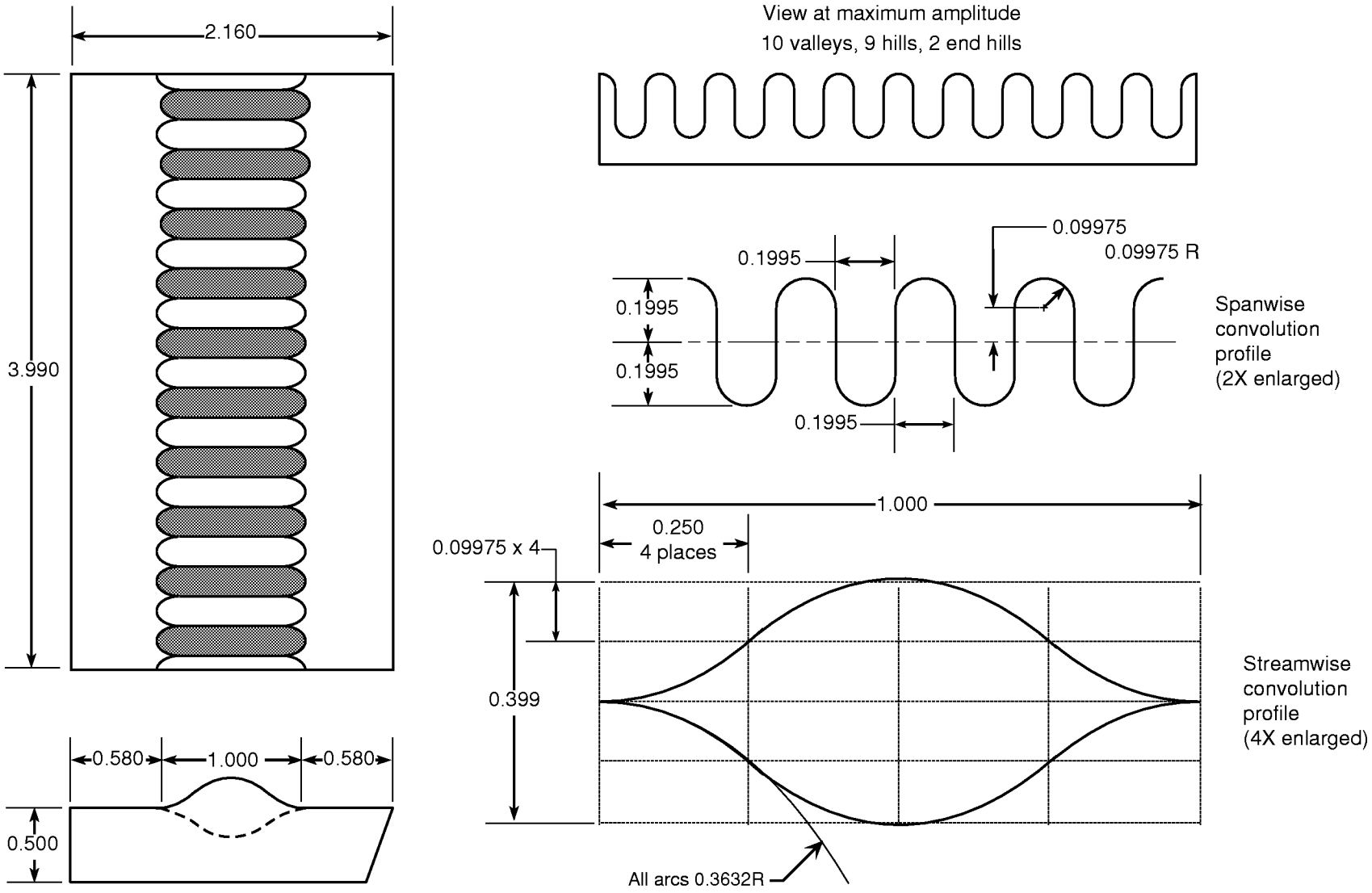

(d) Coarse convoluted flap inserts.

Figure 10. Concluded.

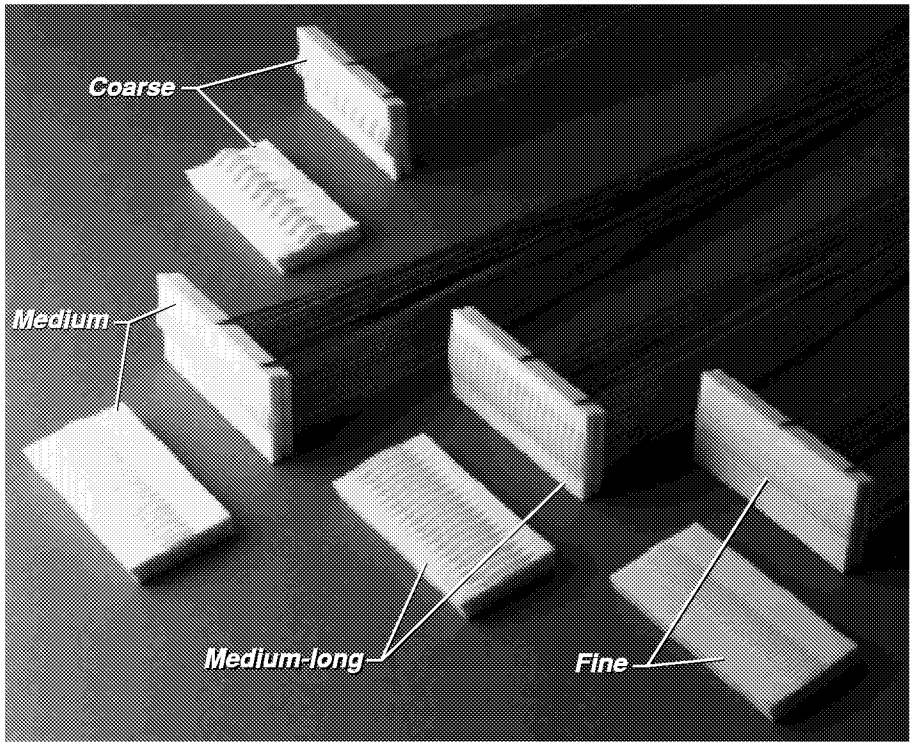

Figure 11. Photograph of the convoluted flap insert pairs.

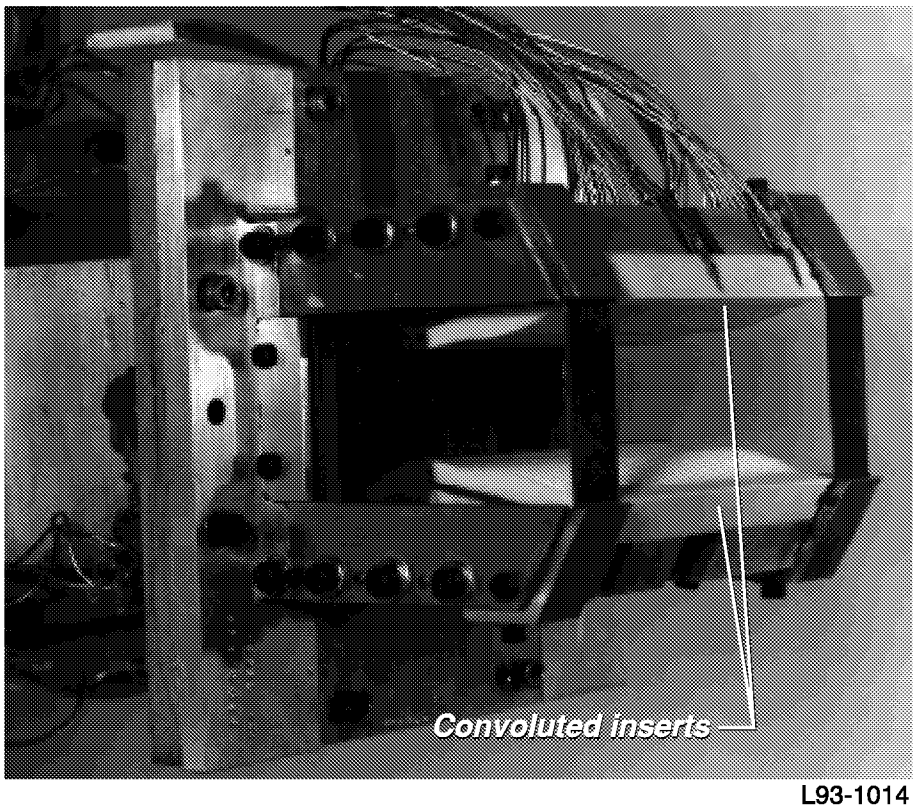

Figure 12. Photograph of the static test model with convoluted flap inserts installed.

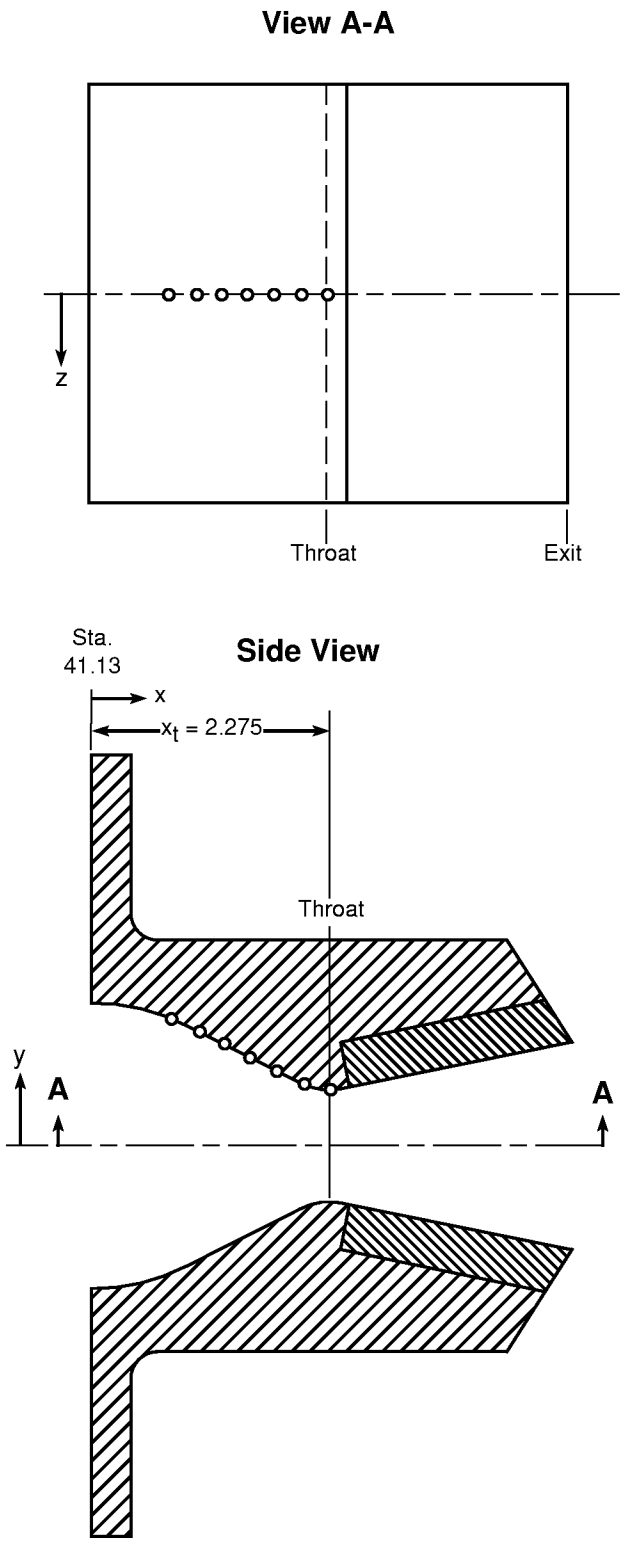

Static Pressure Orifice Locations	
x, in.	x/x_t
0.750	0.330
1.000	0.440
1.250	0.550
1.500	0.659
1.750	0.769
2.025	0.890
2.275	1.000

o Denotes static pressure orifice location

(a) Nozzle flap assembly static pressure taps.

Figure 13. Nozzle static pressure orifice locations. Dimensions are in inches.

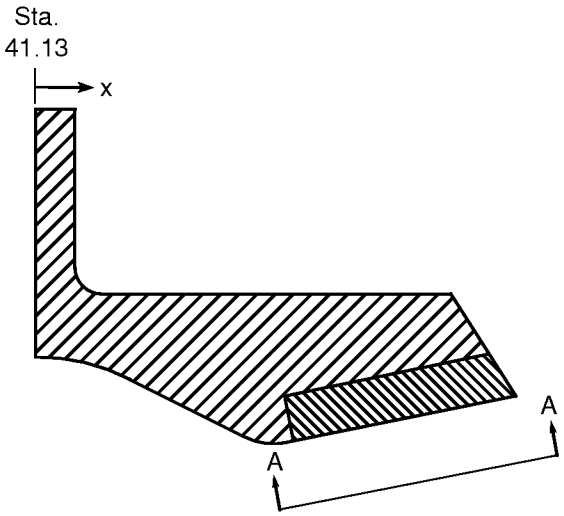

View A-A

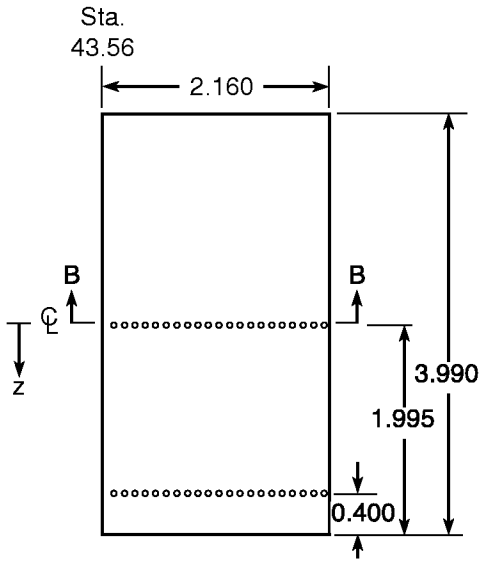

Static Pressure Orifice Locations			
z = 0.000 in.		z = 1.595 in.	
x, in.	x/x_t	x, in.	x/x_t
2.528	1.111	2.528	1.111
2.626	1.154	2.626	1.154
2.724	1.198	2.724	1.198
2.823	1.241	2.823	1.241
2.921	1.284	2.921	1.284
3.019	1.327	3.019	1.327
3.117	1.370	3.117	1.370
3.215	1.413	3.215	1.413
3.313	1.456	3.313	1.456
3.412	1.500	3.412	1.500
3.510	1.543	3.510	1.543
3.608	1.586	3.608	1.586
3.706	1.629	3.706	1.629
3.804	1.672	3.804	1.672
3.902	1.715	3.902	1.715
4.001	1.758	4.001	1.758
4.099	1.802	4.099	1.802
4.197	1.845	4.197	1.845
4.295	1.888	4.295	1.888
4.393	1.931	4.393	1.931
4.491	1.974	4.491	1.974

o Denotes static pressure orifice location

Section B-B

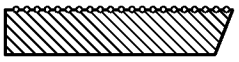

(b) Baseline flap insert static pressure taps.

Figure 13. Continued.

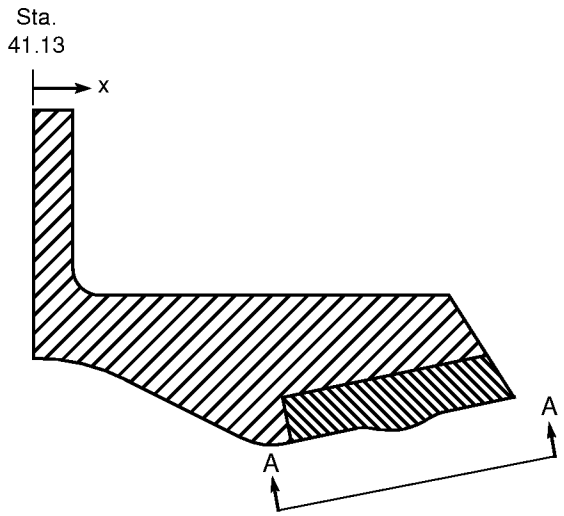

Static Pressure Orifice Locations					
z = 0.000 in.		z = 0.1995 in.		z = 1.595 in.	
x, in.	x/x_t	x, in.	x/x_t	x, in.	x/x_t
2.528	1.111			2.528	1.111
2.626	1.154			2.626	1.154
2.724	1.198			2.724	1.198
2.823	1.241			2.823	1.241
2.921	1.284			2.921	1.284
3.019	1.327	3.019	1.327	3.019	1.327
3.117	1.370	3.117	1.370	3.117	1.370
3.215	1.413	3.215	1.413	3.215	1.413
3.313	1.456	3.313	1.456	3.313	1.456
3.412	1.500	3.412	1.500	3.412	1.500
3.510	1.543	3.510	1.543	3.510	1.543
3.608	1.586	3.608	1.586	3.608	1.586
3.706	1.629	3.706	1.629	3.706	1.629
3.804	1.672	3.804	1.672	3.804	1.672
3.902	1.715	3.902	1.715	3.902	1.715
4.001	1.758			4.001	1.758
4.099	1.802			4.099	1.802
4.197	1.845			4.197	1.845
4.295	1.888			4.295	1.888
4.393	1.931			4.393	1.931
4.491	1.974			4.491	1.974

o Denotes static pressure orifice location

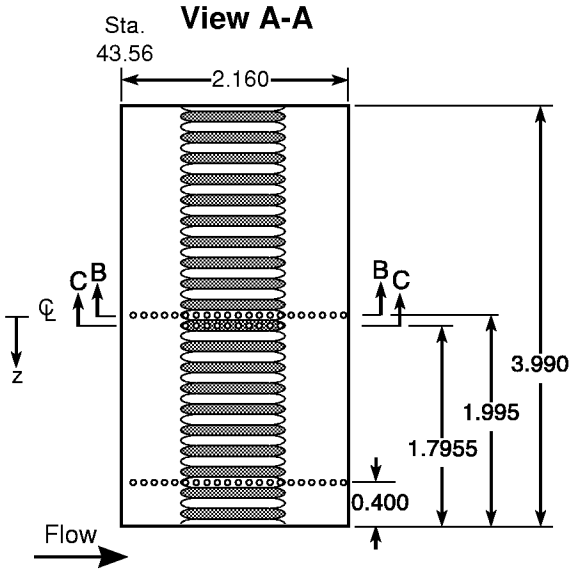

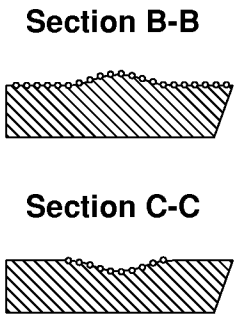

(c) Convoluted flap inserts (medium convoluted flap insert shown) static pressure taps.

Figure 13. Concluded.

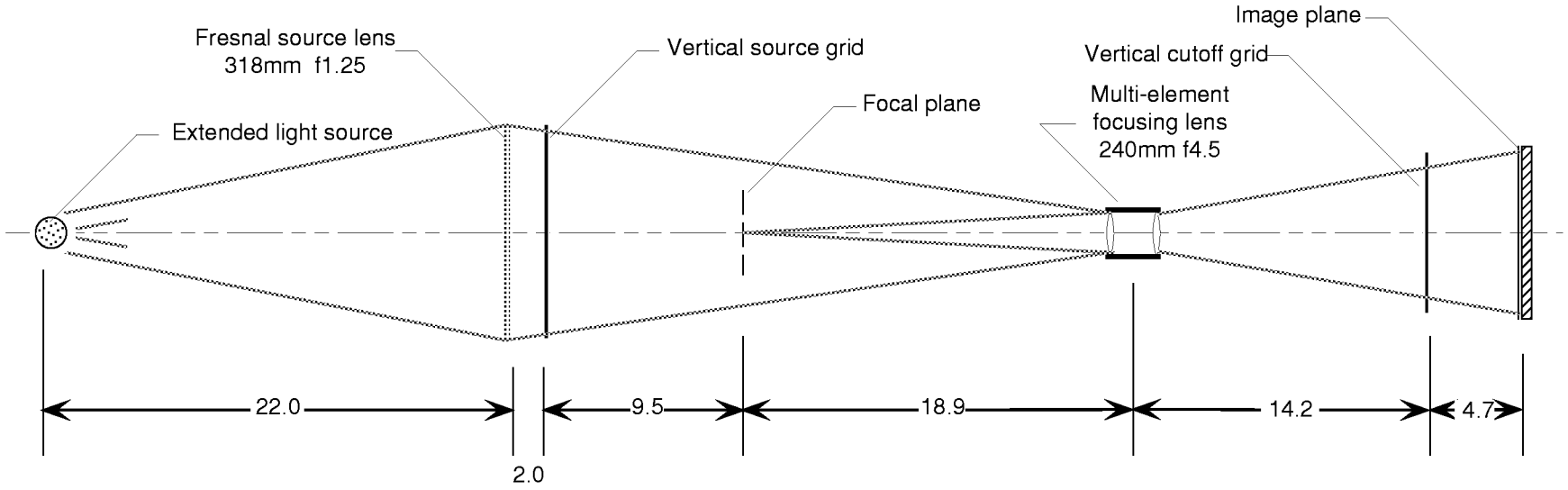

Source grid details

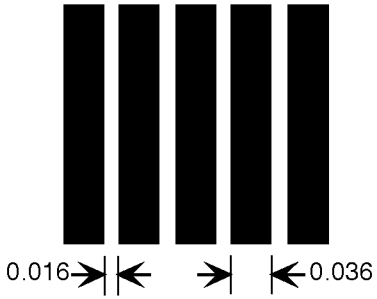

Note: Cutoff grid is optical negative of source grid.

(a) Optical description.

Figure 14. Optical description and schematic layout of focusing schlieren flow visualization system. Dimensions are in inches.

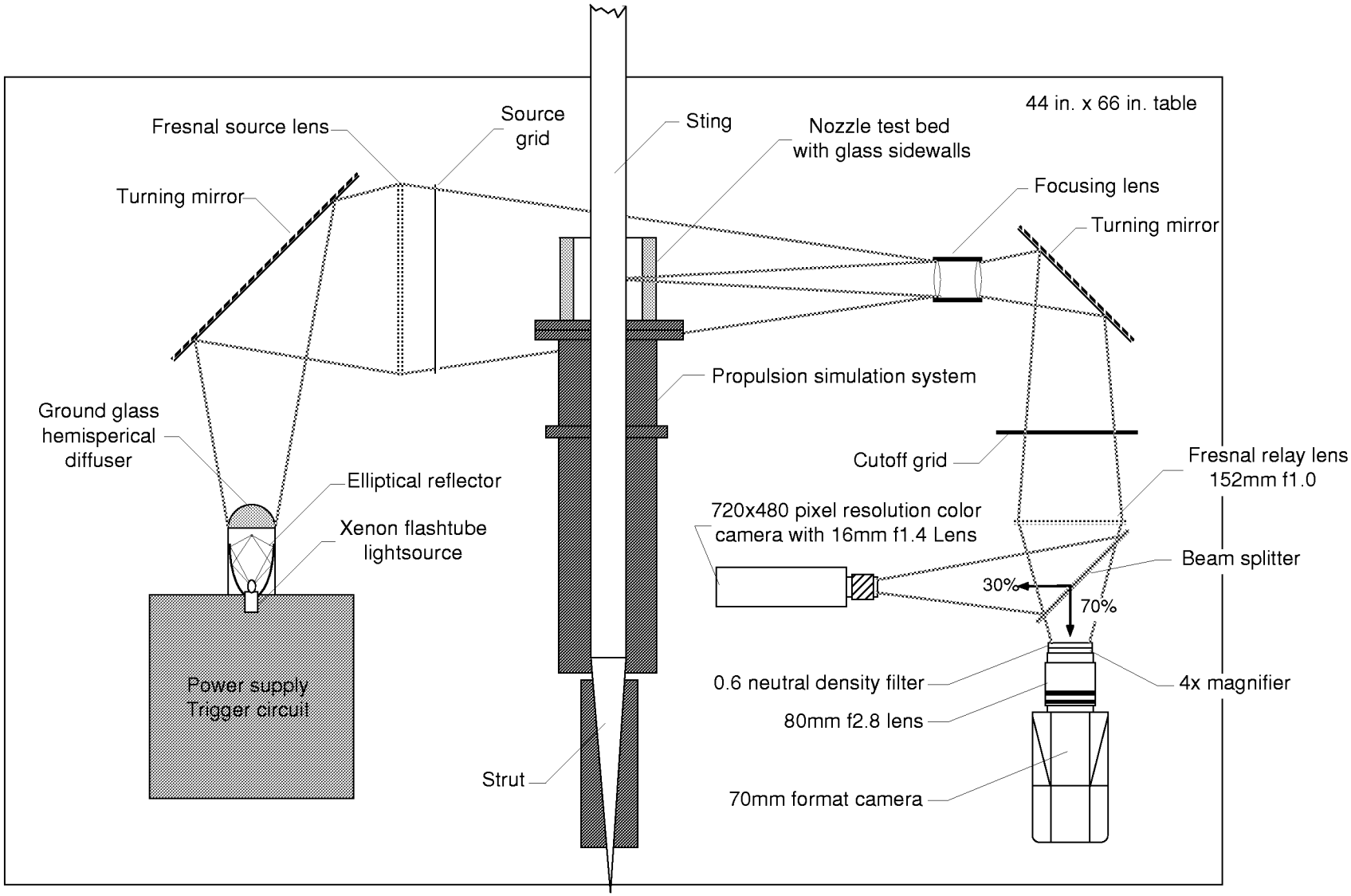

(b) Schematic layout.

Figure 14. Concluded.

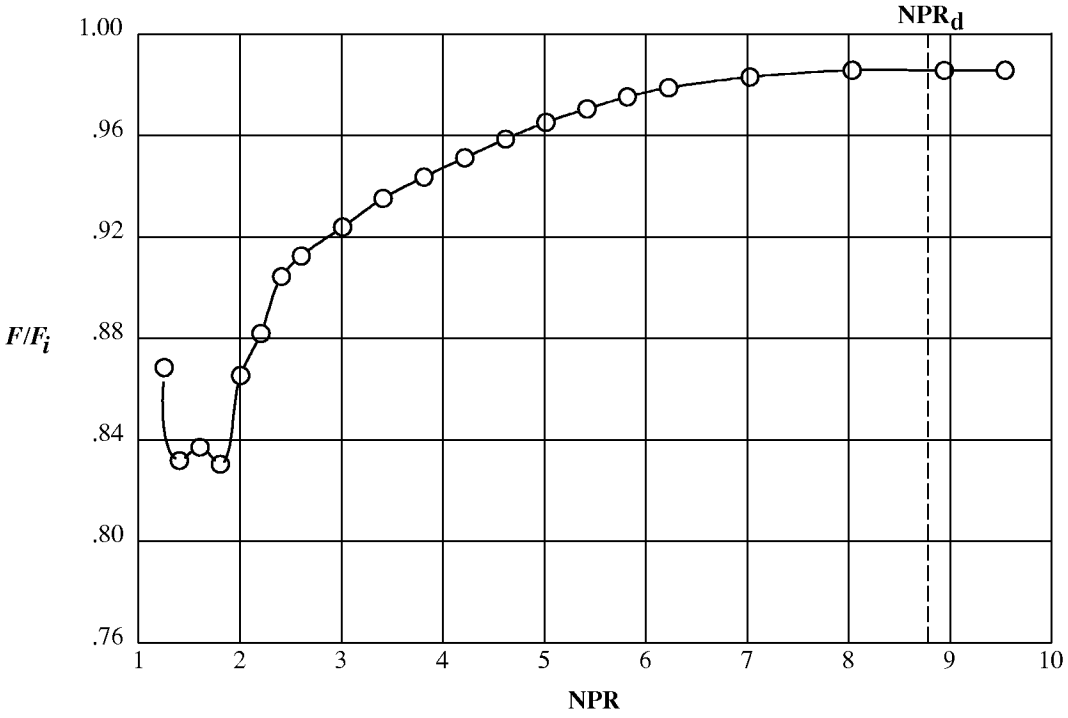

Figure 15. Nozzle thrust ratio performance for the baseline configuration.

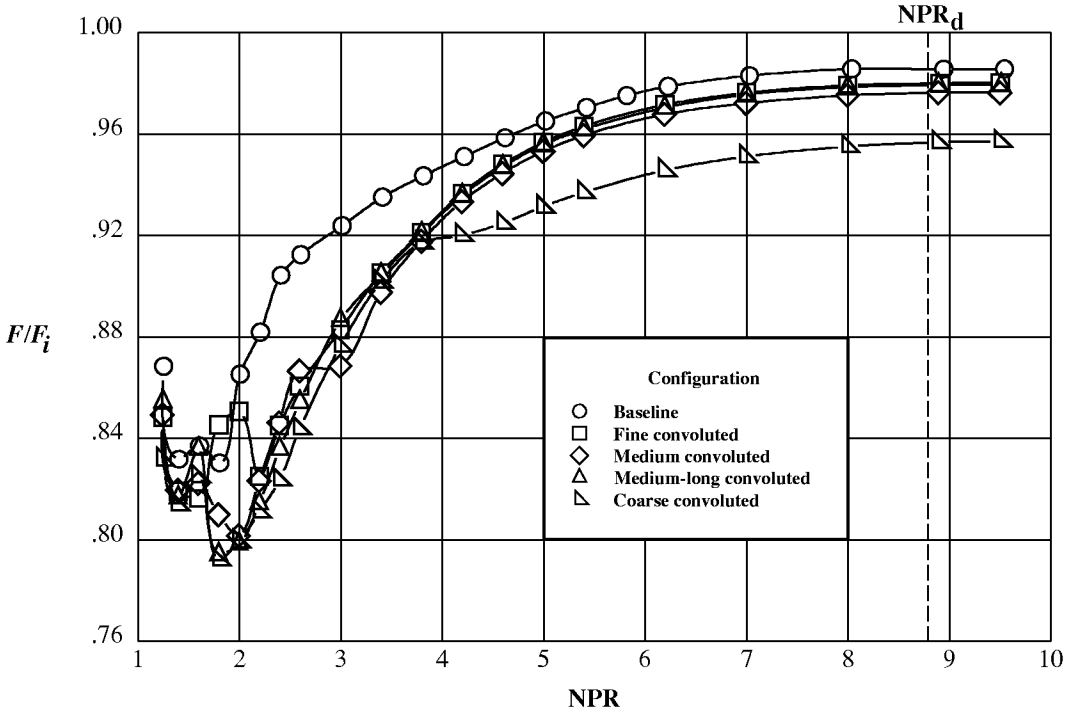

Figure 16. Comparison of nozzle thrust ratio performance for baseline and convoluted configurations.

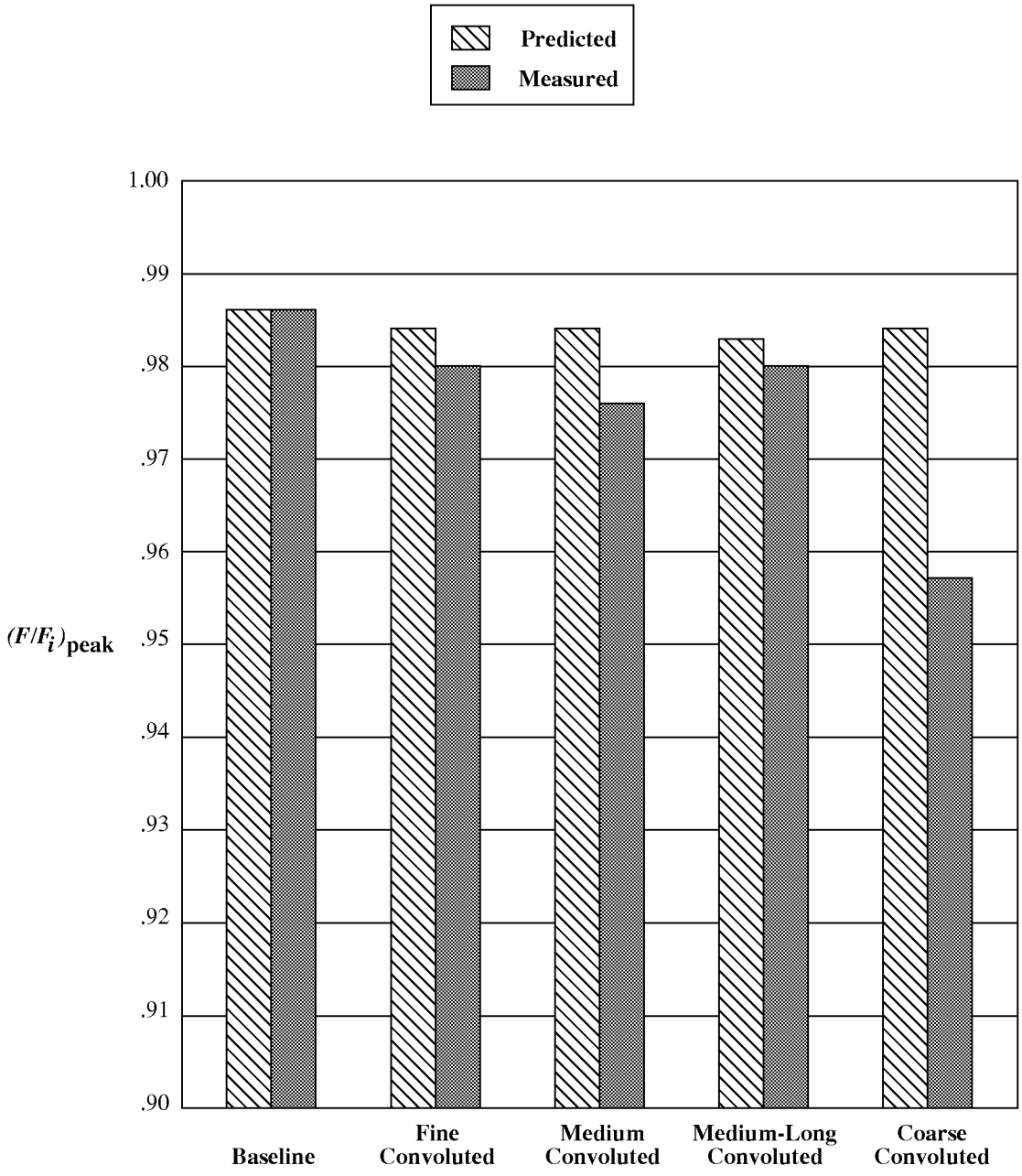

Figure 17. Comparison of NPAC predicted and experimentally measured peak thrust ratios for baseline and convoluted configurations.

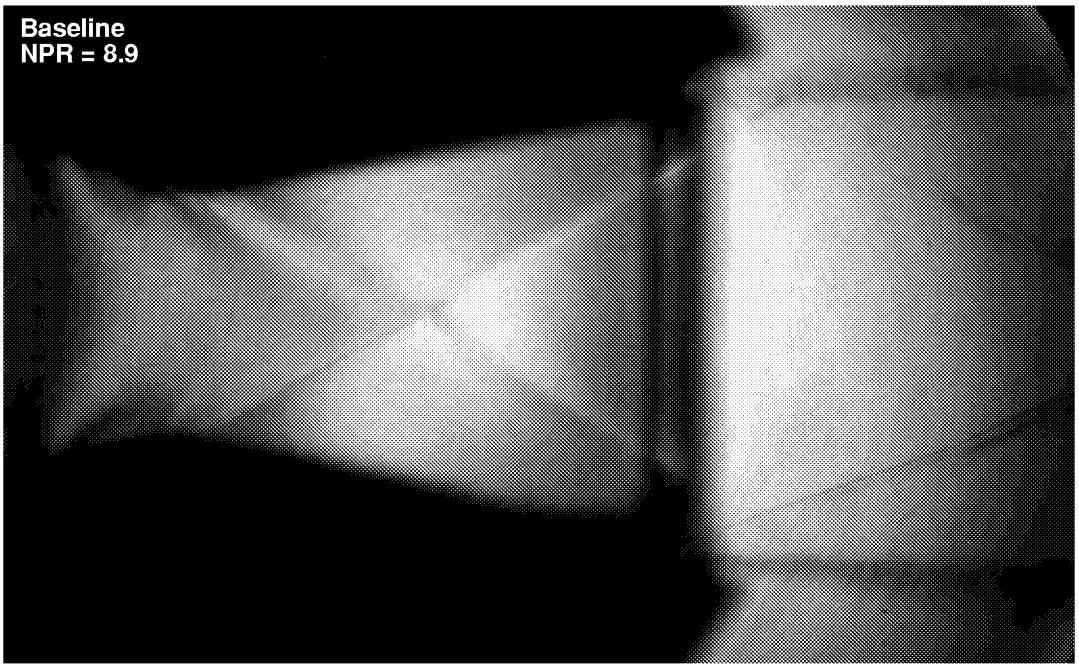

(a) Baseline configuration.

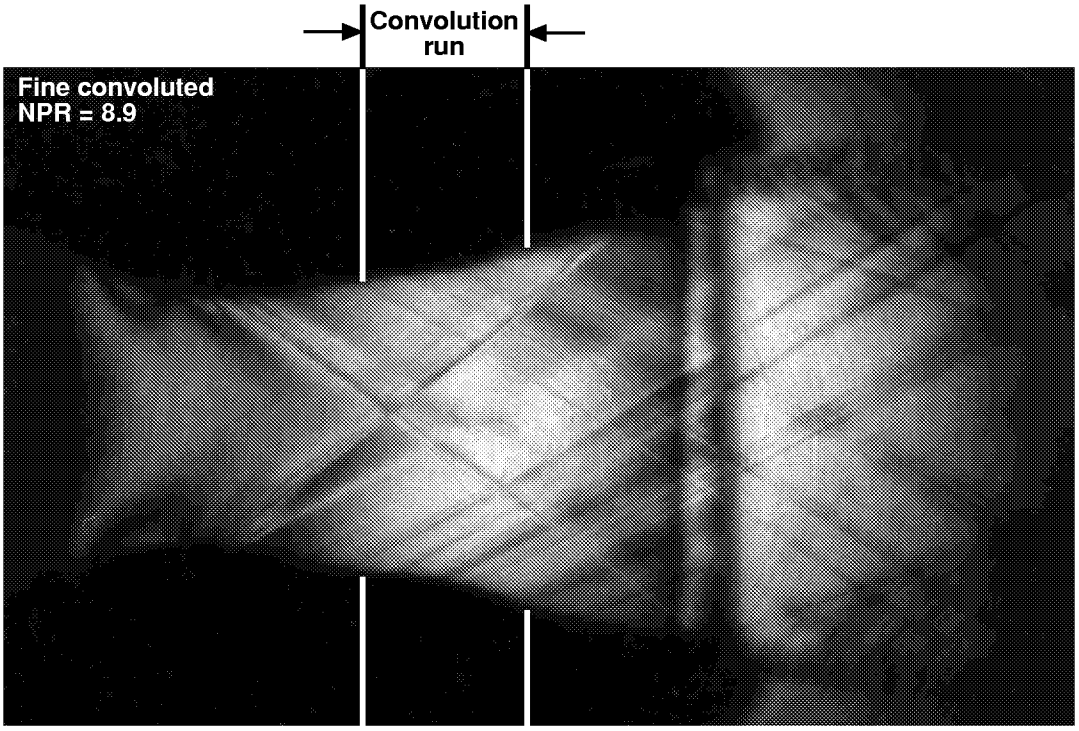

(b) Fine convoluted configuration.

Figure 18. Focusing schlieren flow visualization at NPR=8.9 for baseline and convoluted configurations.

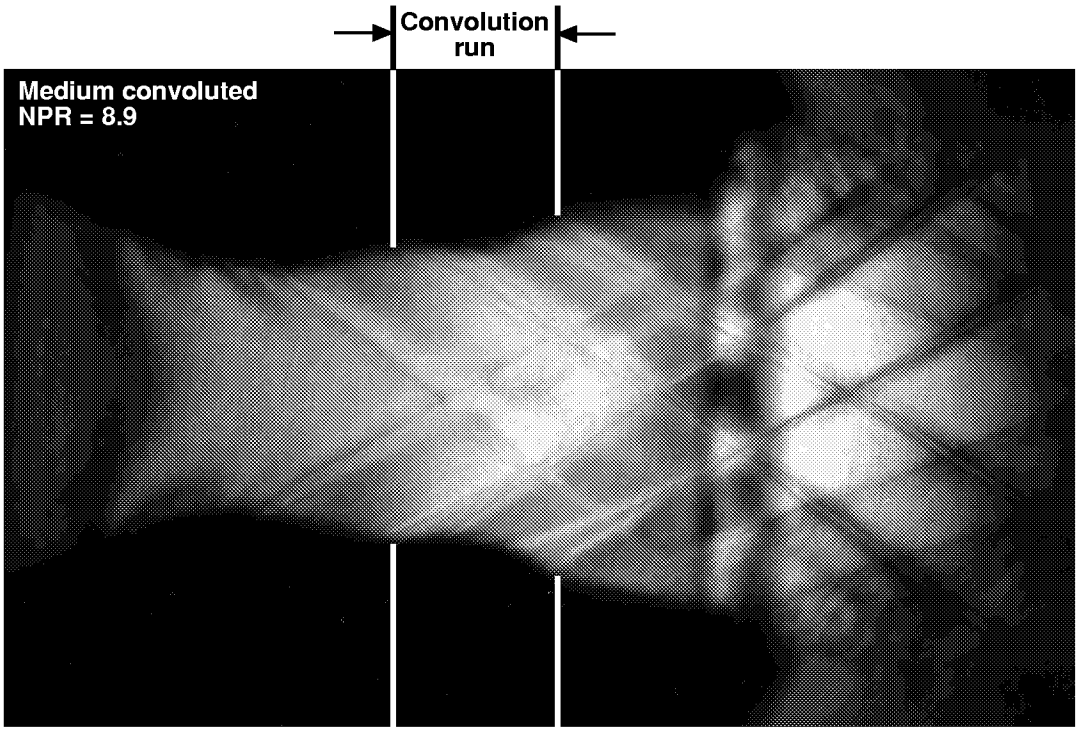

(c) Medium convoluted configuration.

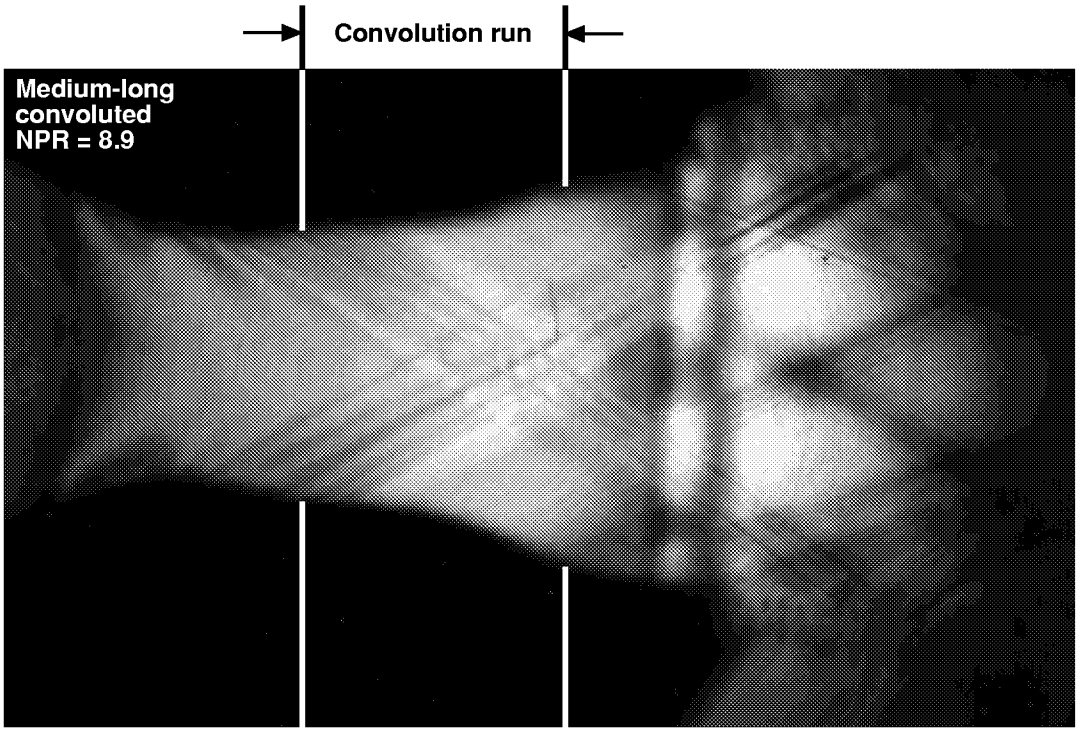

(d) Medium-long convoluted configuration.

Figure 18. Continued.

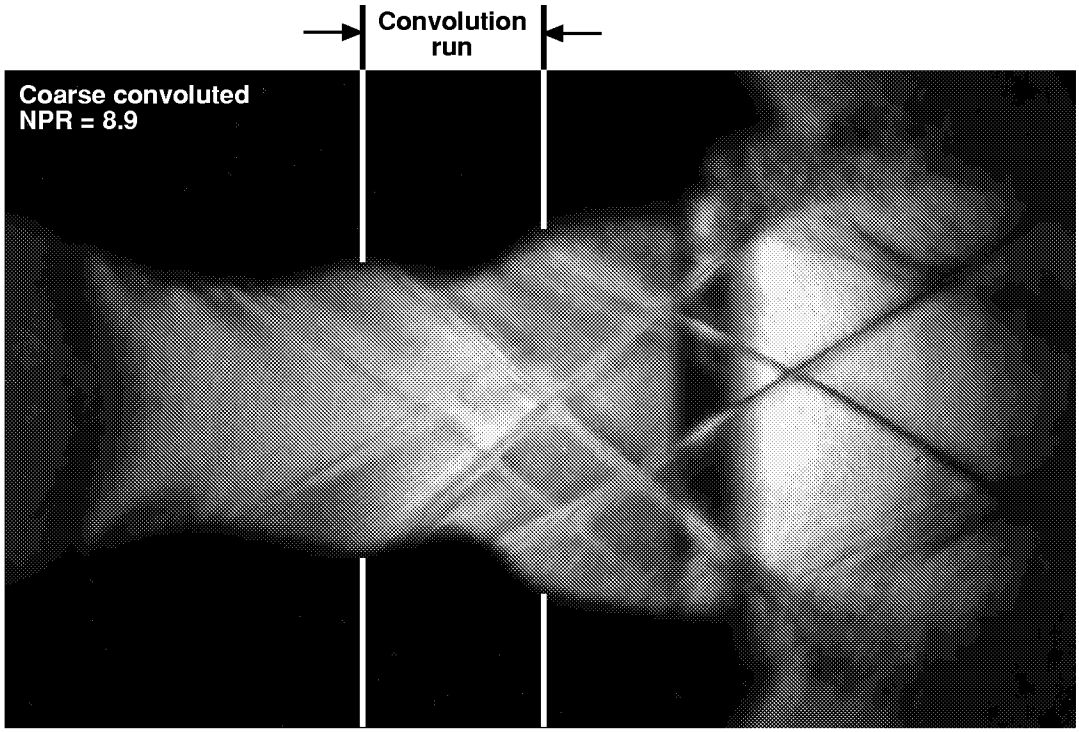

(e) Coarse convoluted configuration.

Figure 18. Concluded.

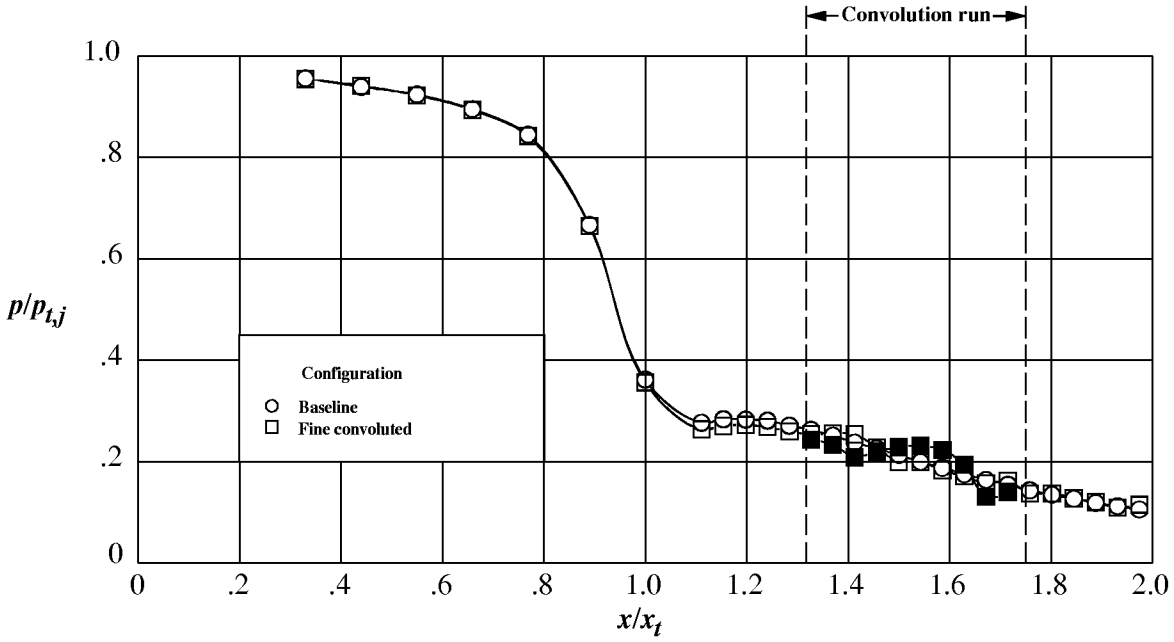

(a) Fine convoluted configuration.

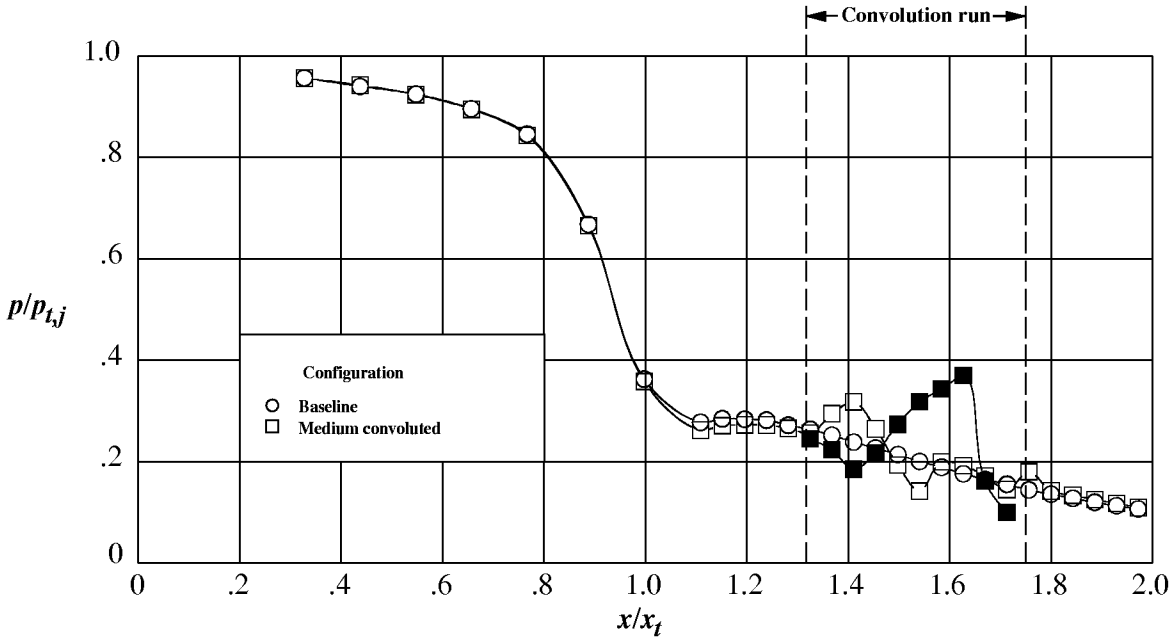

(b) Medium convoluted configuration.

Figure 19. Comparison of baseline and convoluted internal static pressure ratio distributions at NPR=8.9. Open symbols deonte hill pressures; solid symbols denote valley pressures.

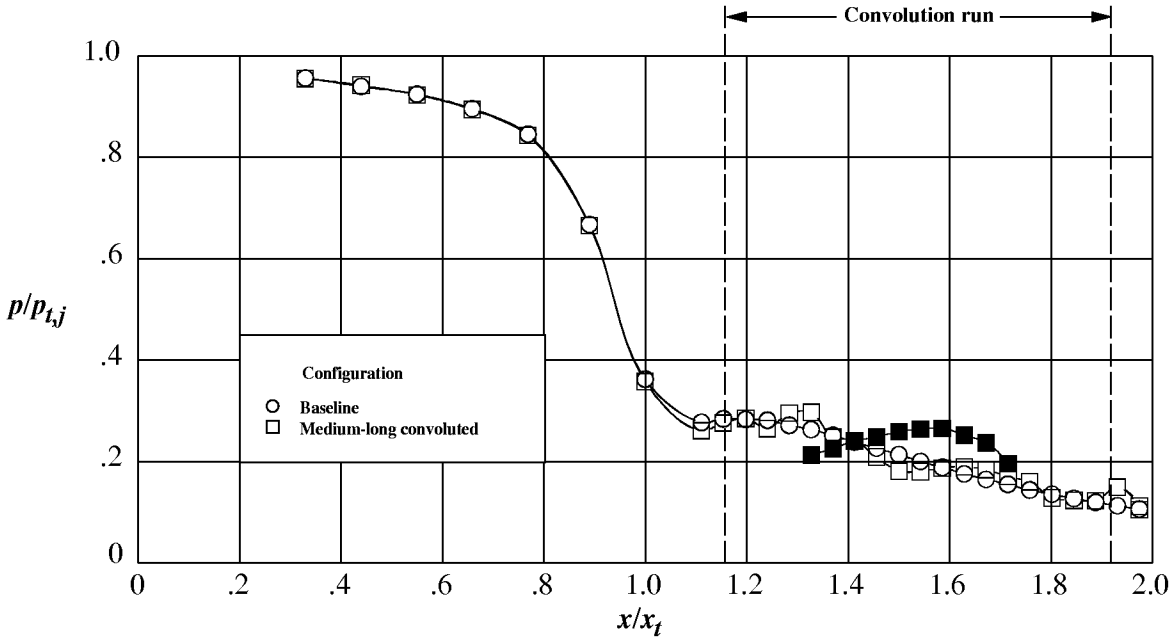

(c) Medium-long convoluted configuration.

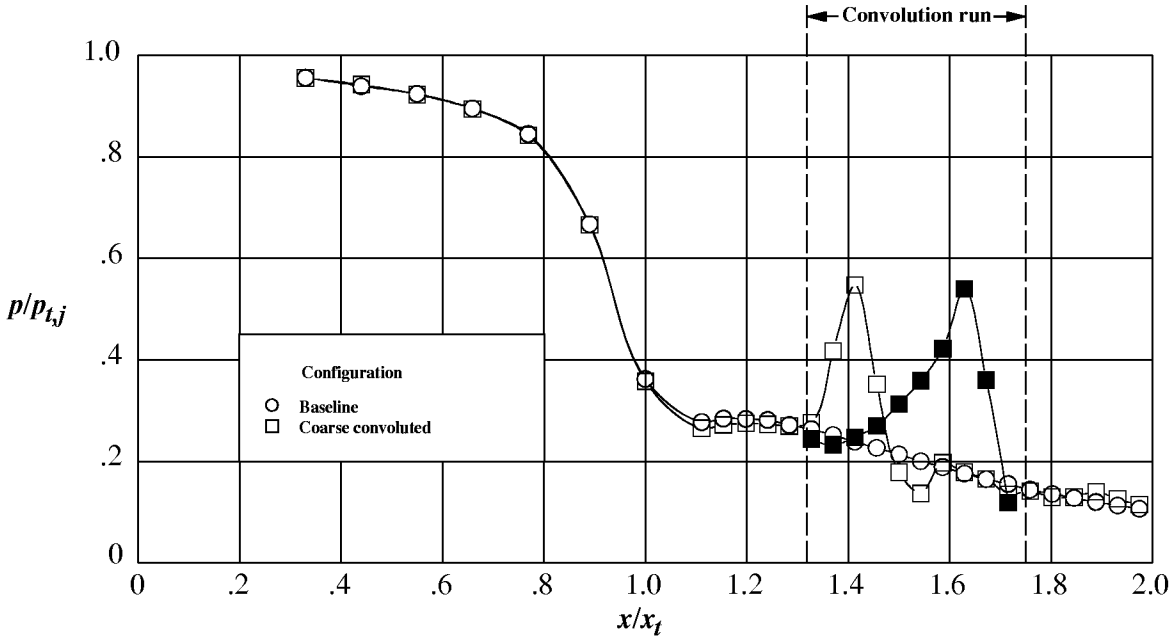

(d) Coarse convoluted configuration.

Figure 19. Concluded.

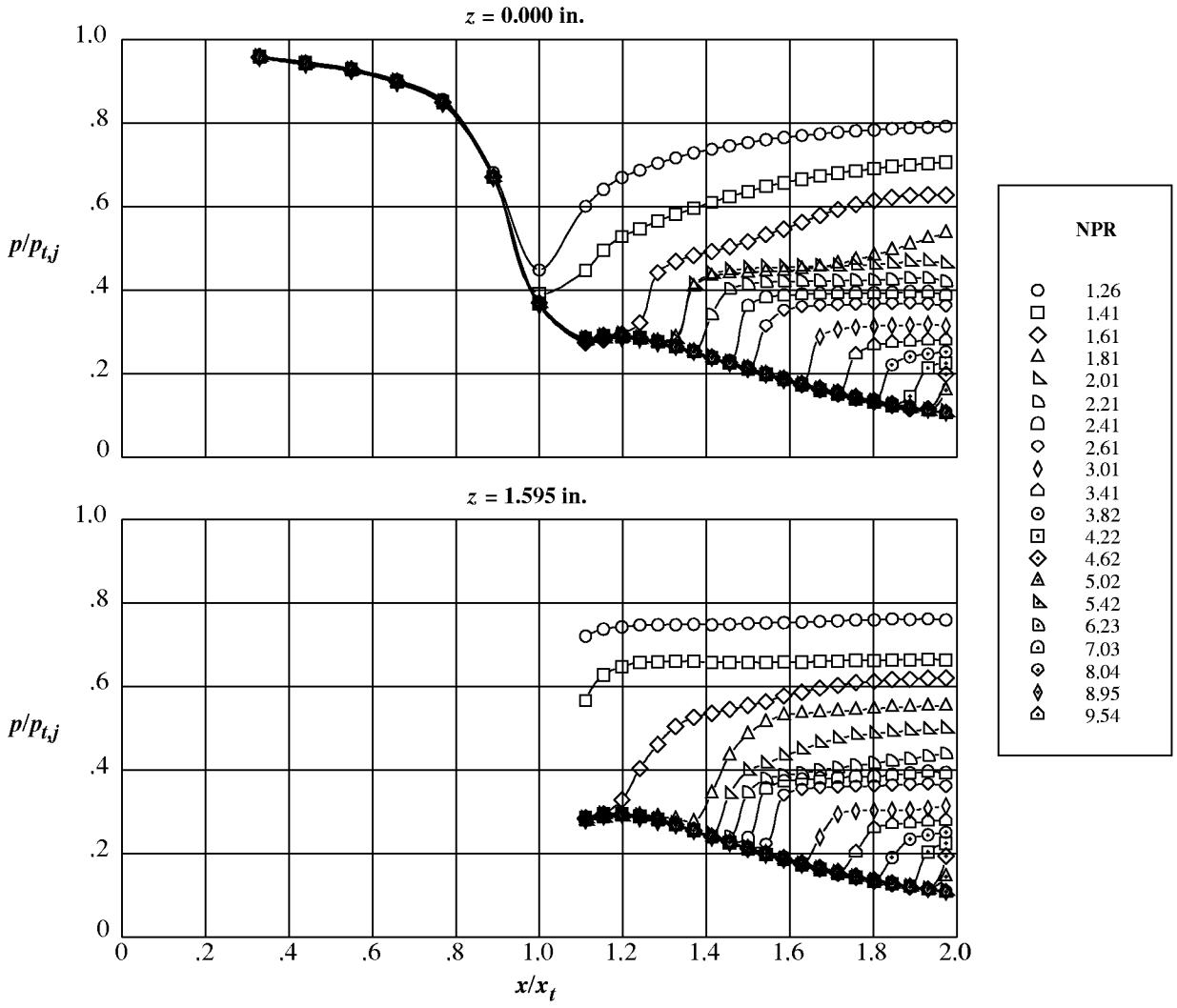

Figure 20. Internal static pressure ratio distributions for the baseline configuration.

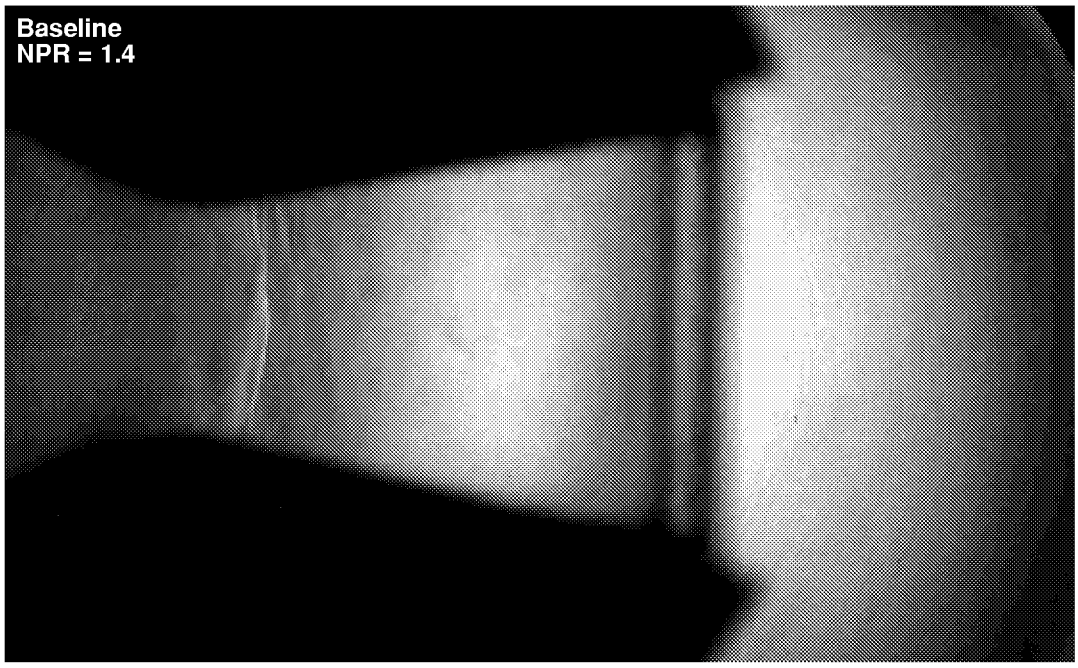

(a) NPR = 1.4.

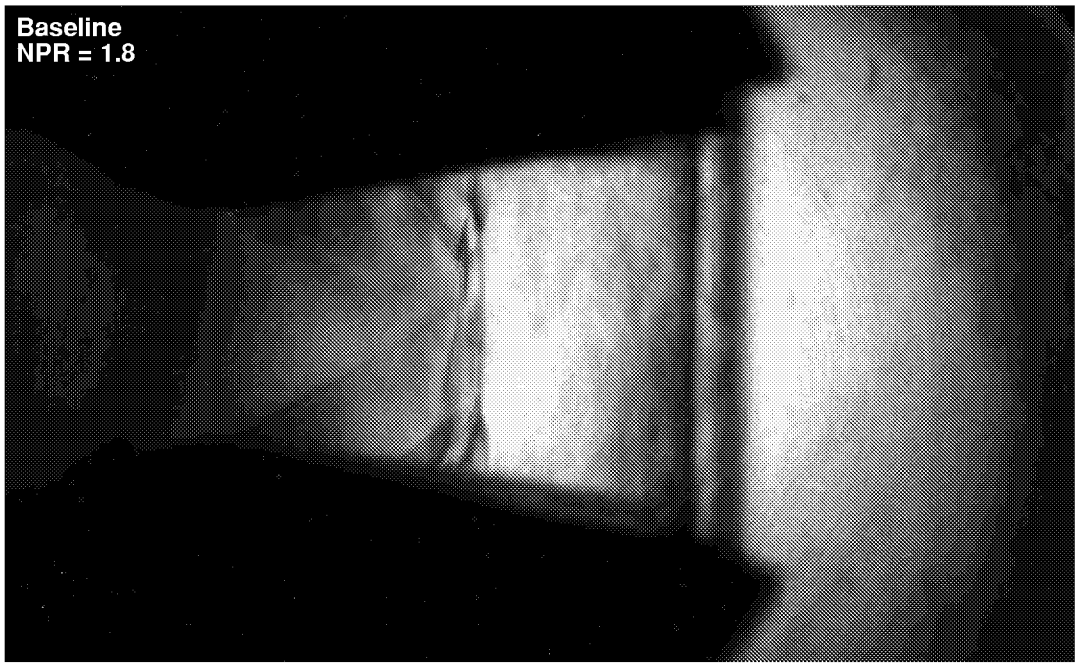

(b) NPR = 1.8.

Figure 21. Focusing schlieren flow visualization for the baseline configuration.

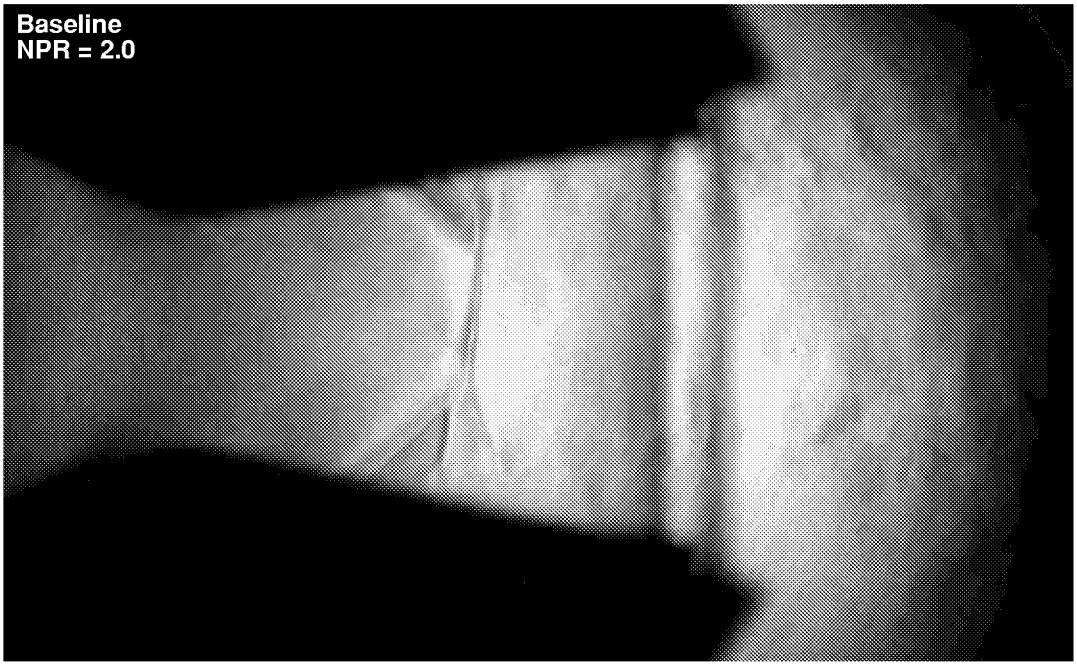

(c) NPR = 2.0.

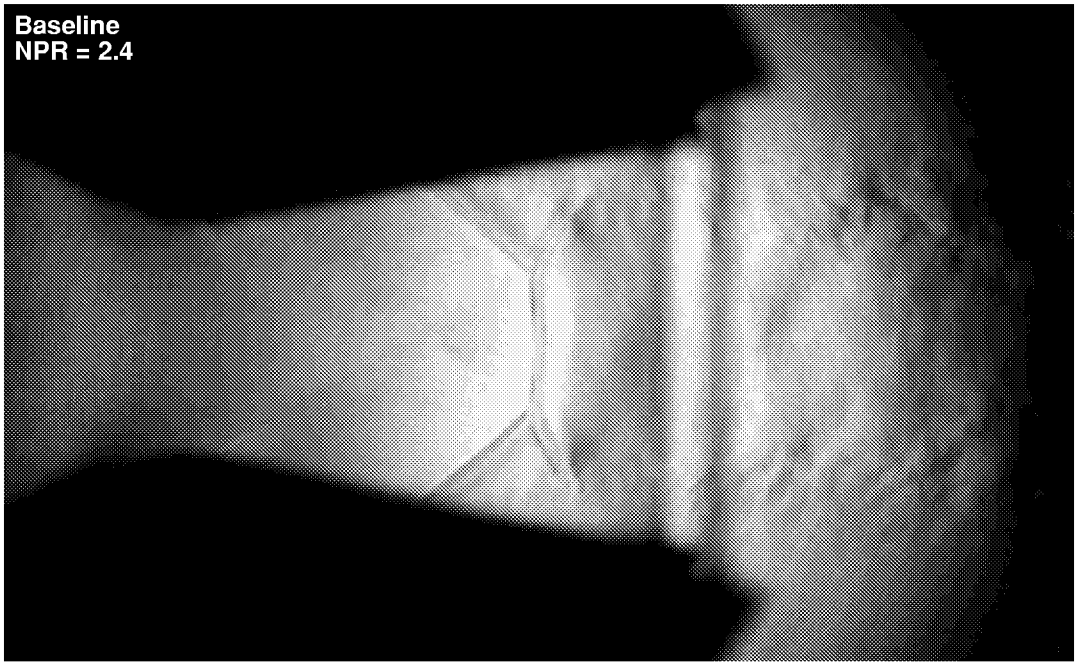

(d) NPR = 2.4.

Figure 21. Continued.

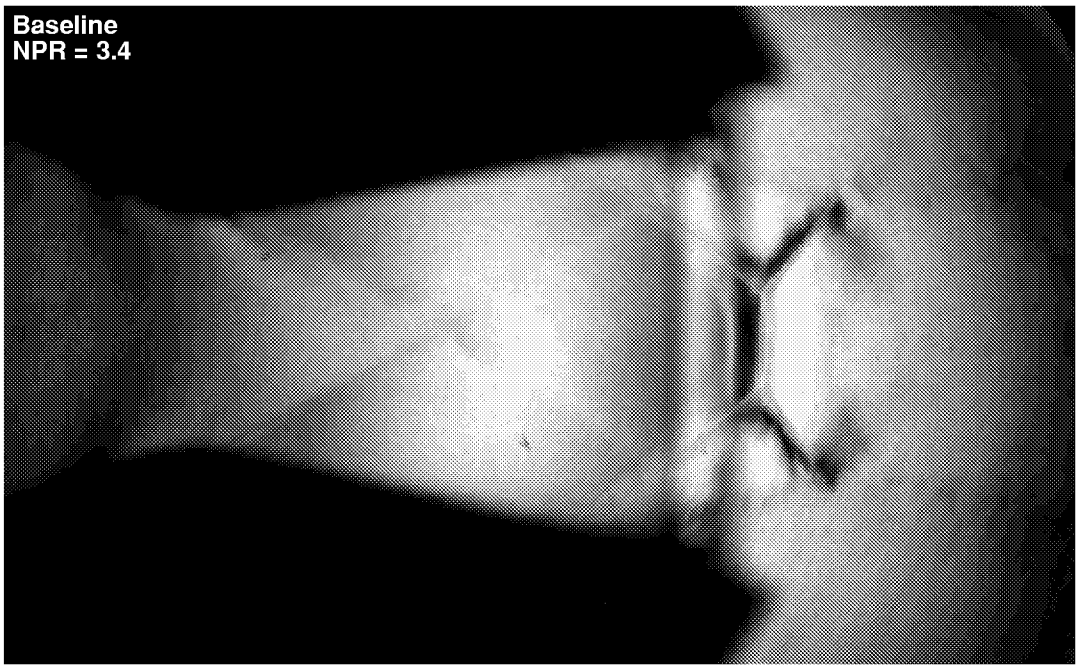

(e) NPR = 3.4.

Figure 21. Concluded.

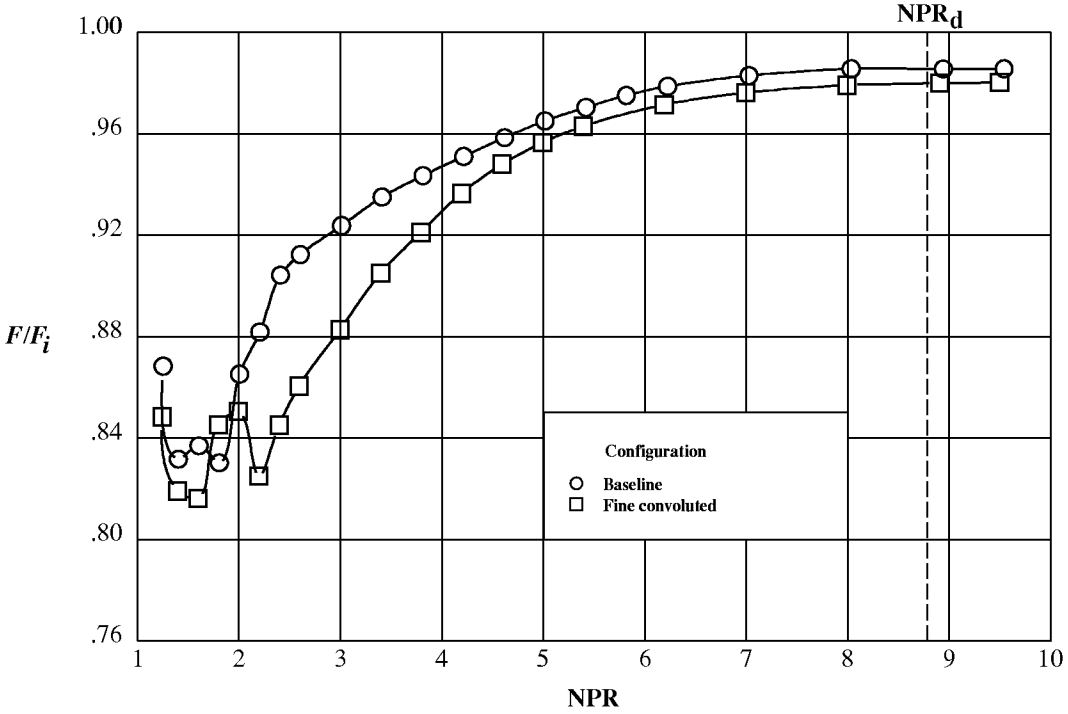

(a) Fine convoluted configuration.

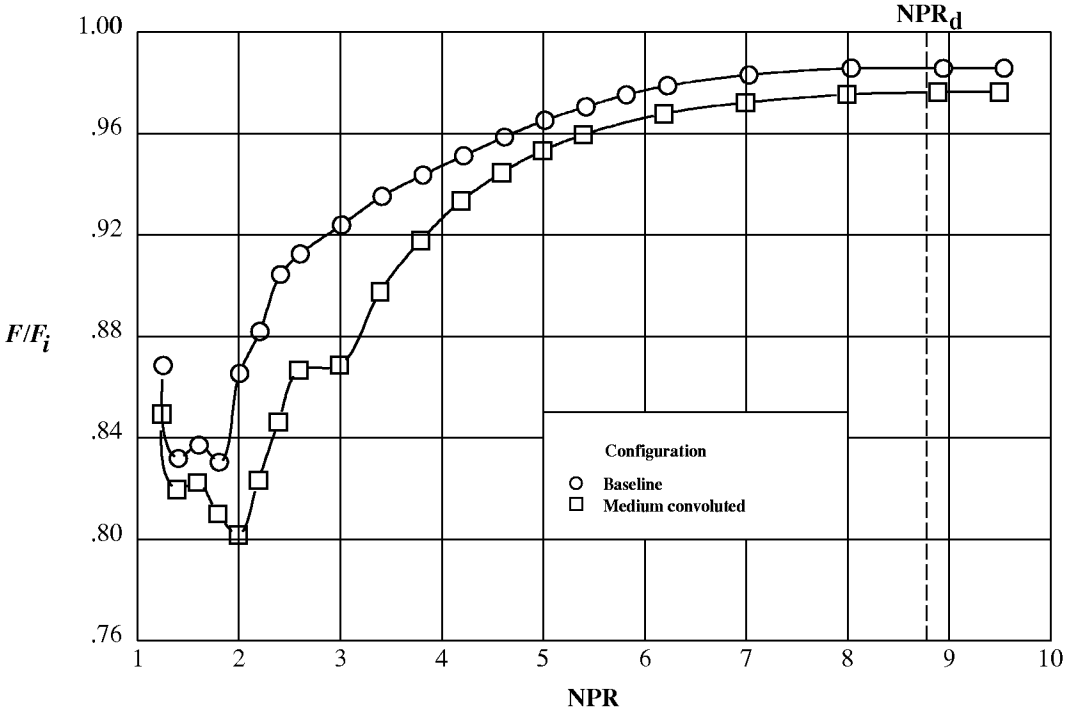

(b) Medium convoluted configuration.

Figure 22. Individual comparisons of nozzle thrust ratio performance for baseline and convoluted configurations.

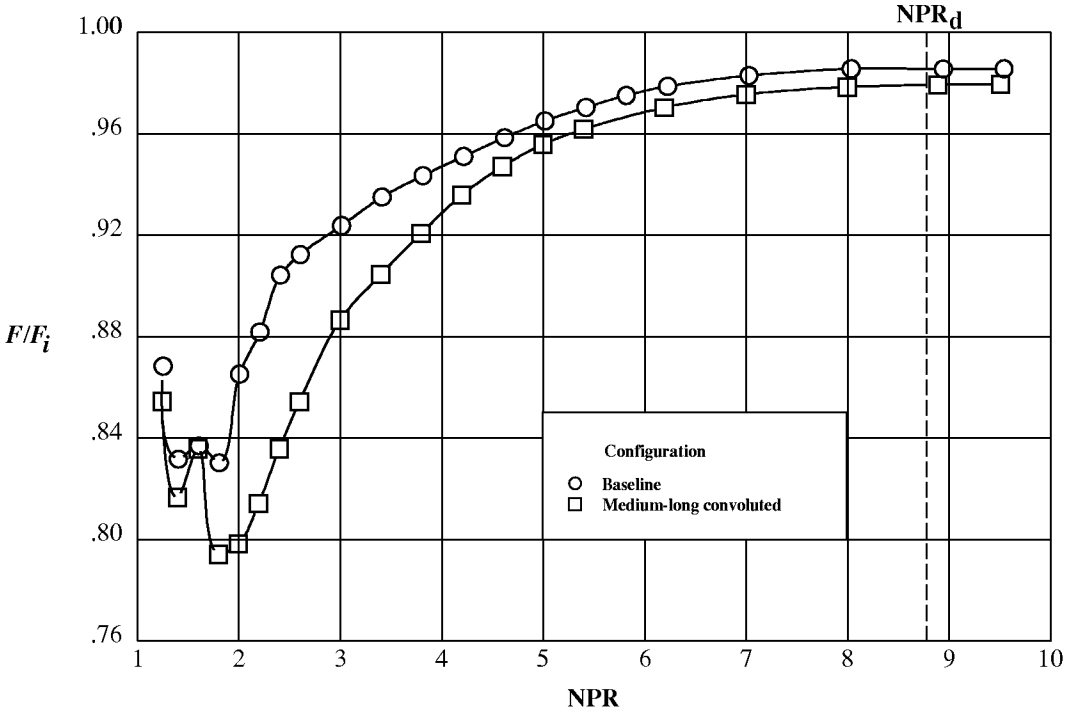

(c) Medium-long convoluted configuration.

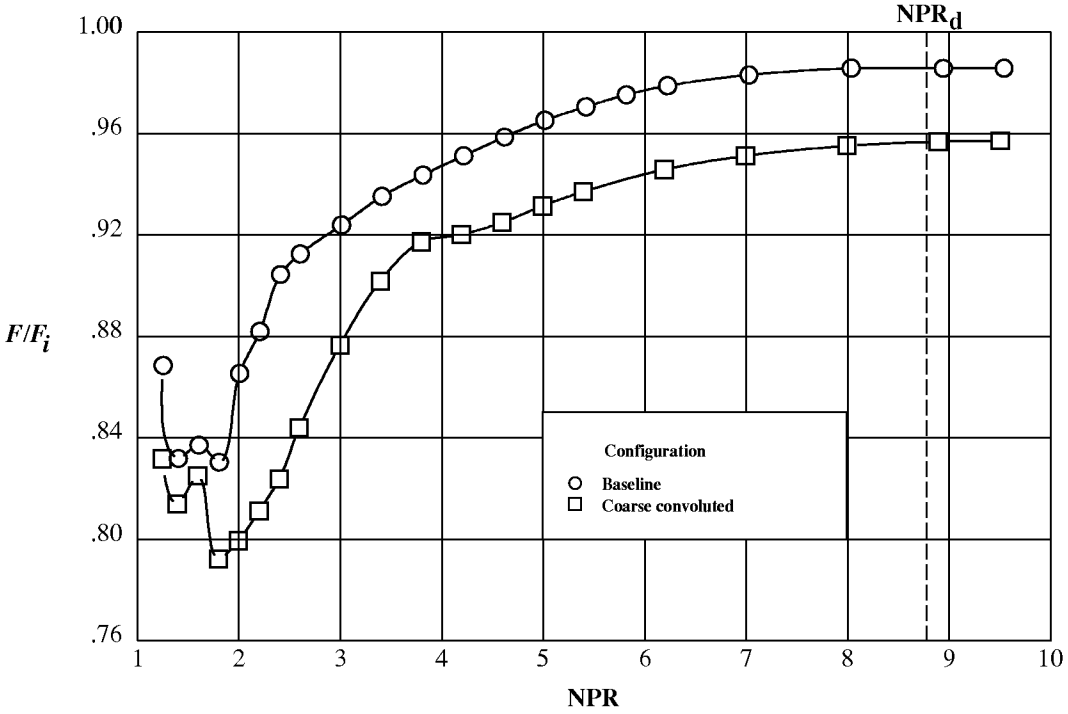

(d) Coarse convoluted configuration.

Figure 22. Concluded.

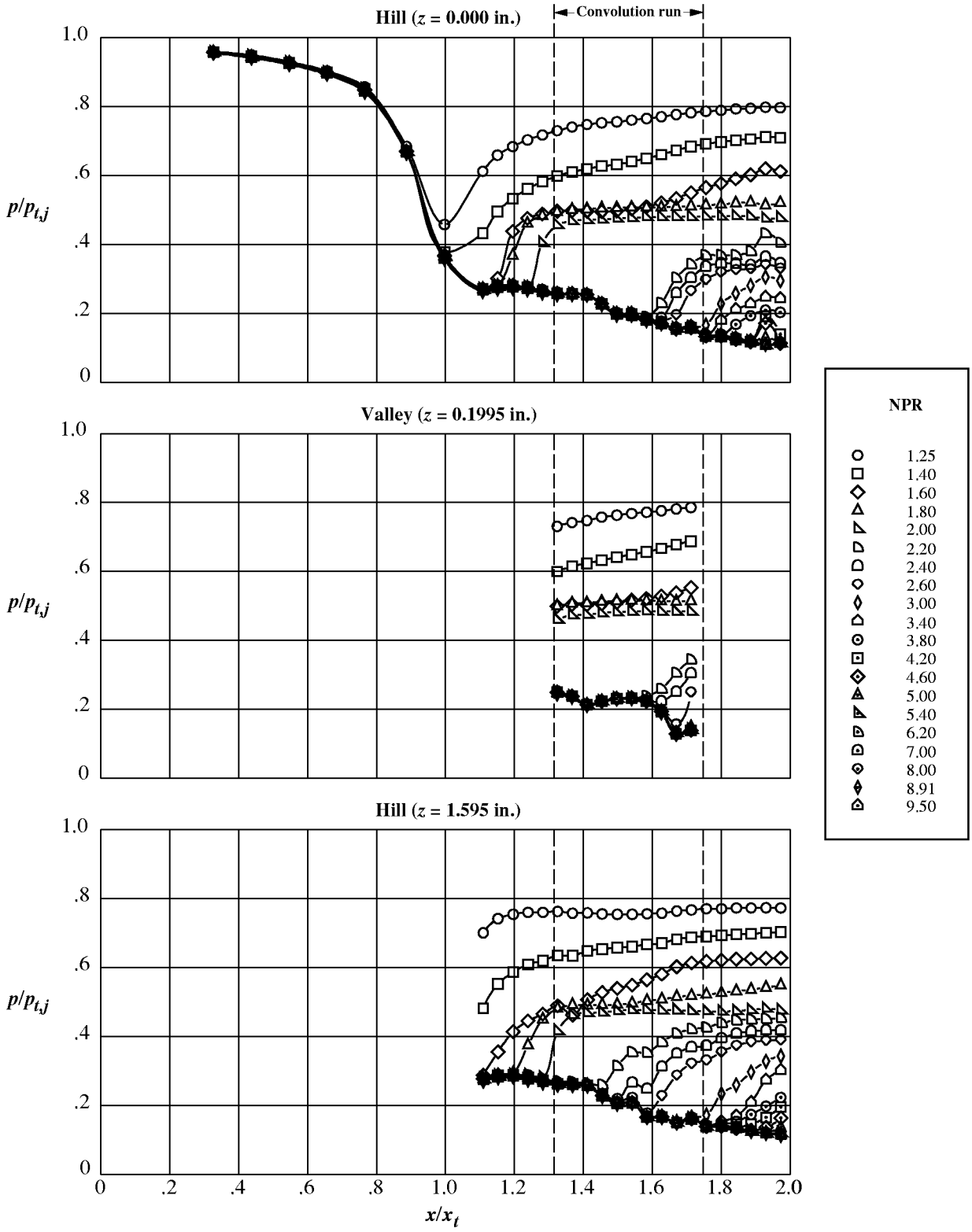

(a) Fine convoluted configuration.

Figure 23. Internal static pressure ratio distributions for convoluted configurations.

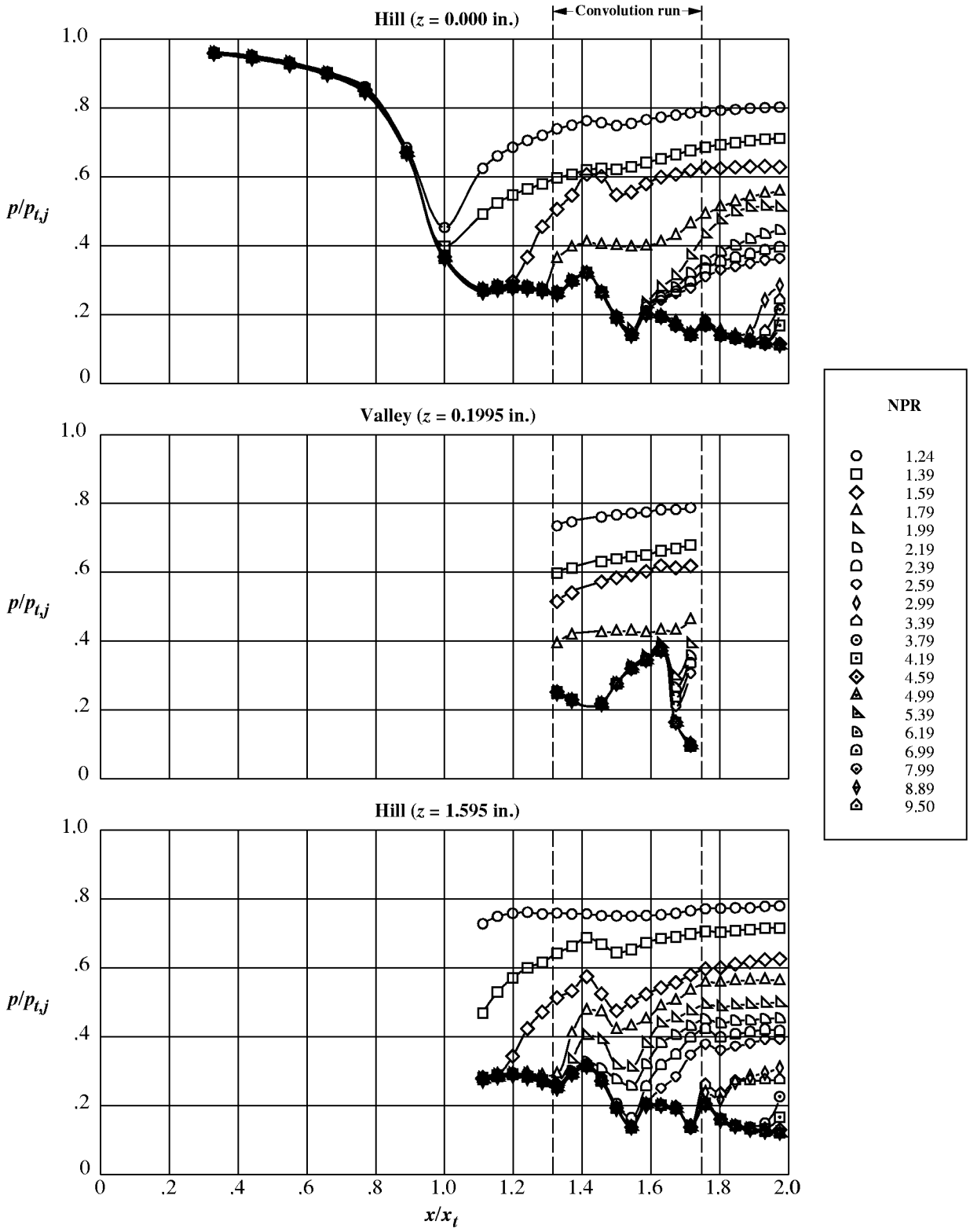

(b) Medium convoluted configuration.

Figure 23. Continued.

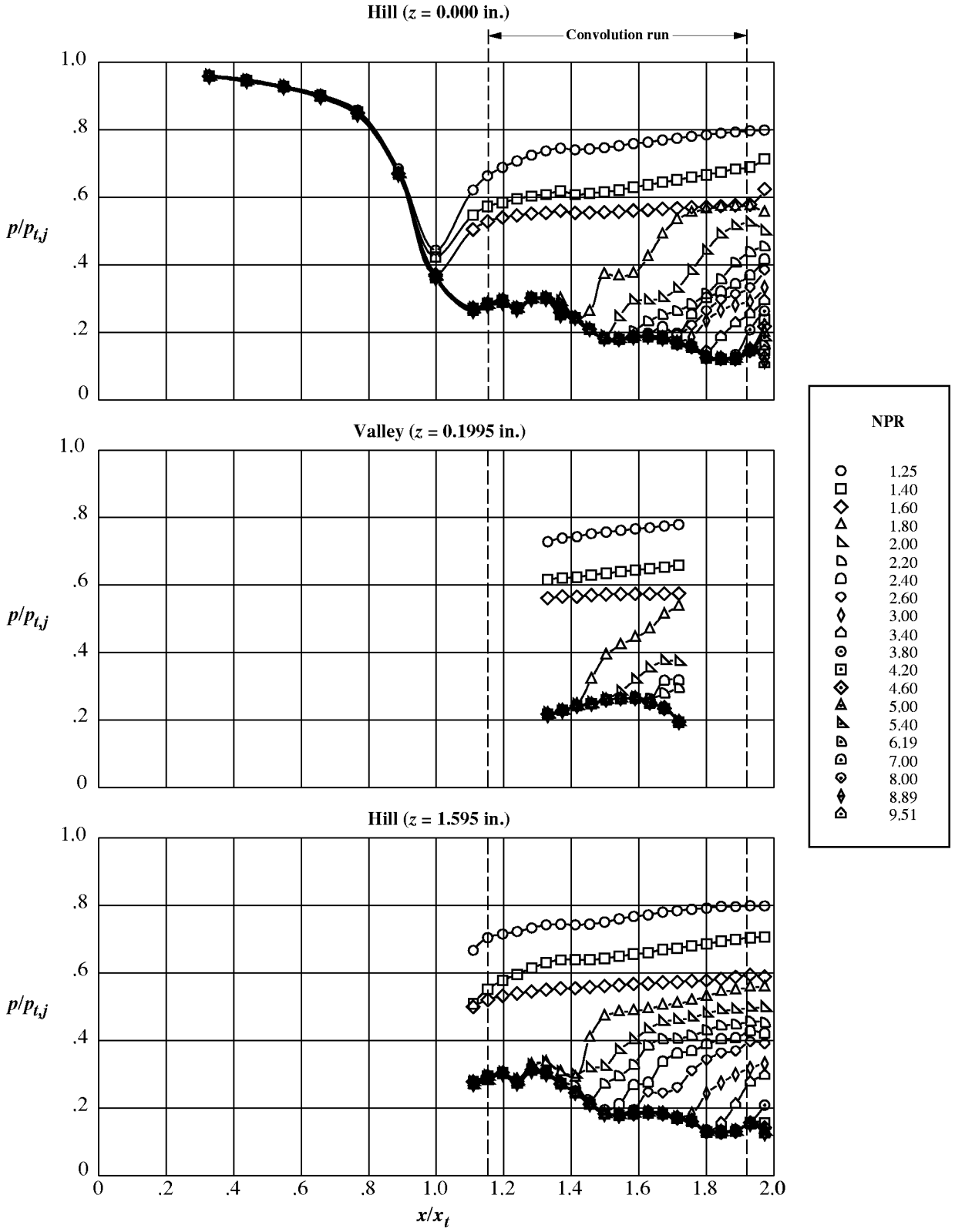

(c) Medium-long convoluted configuration.

Figure 23. Continued.

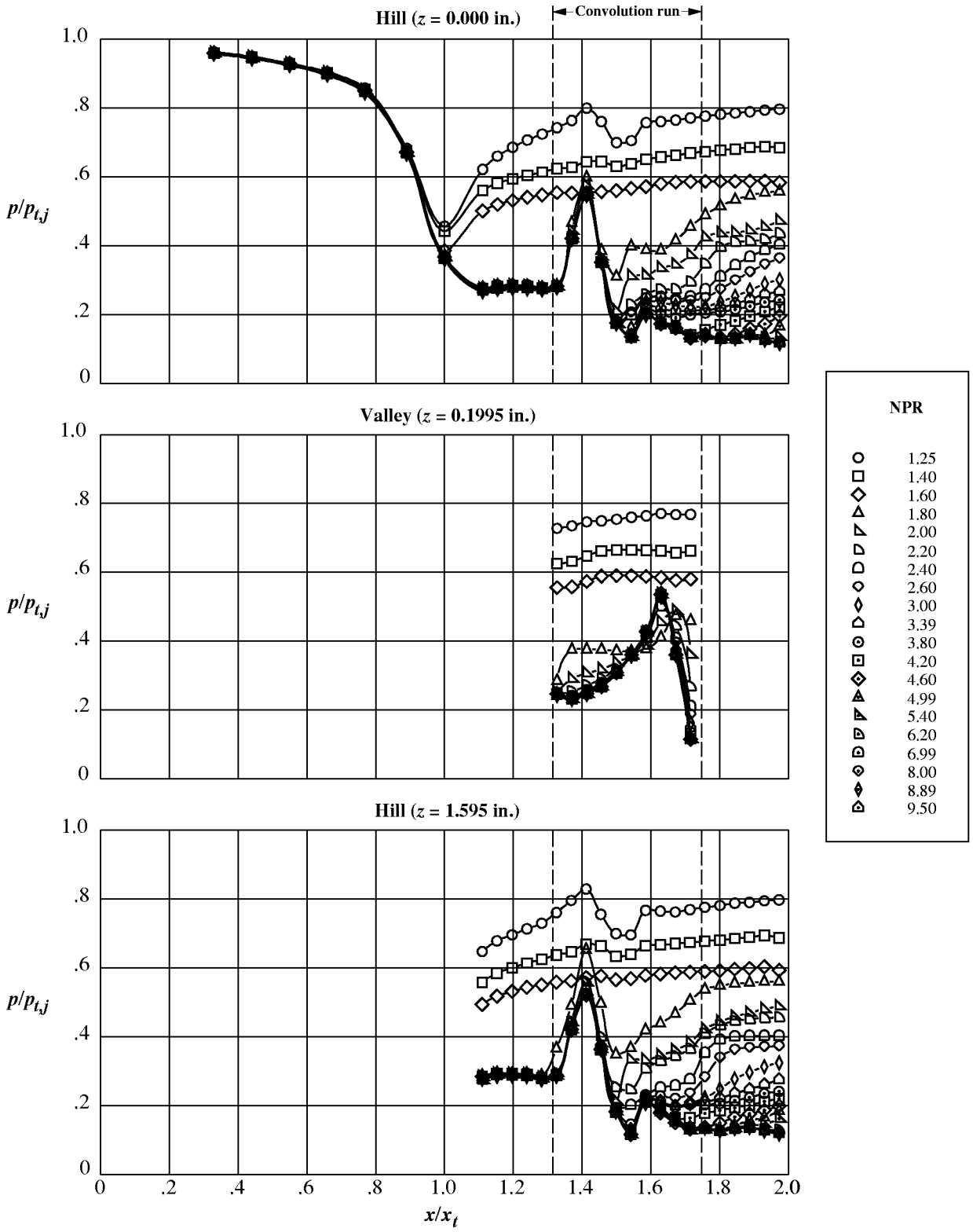

(d) Coarse convoluted configuration.

Figure 23. Concluded.

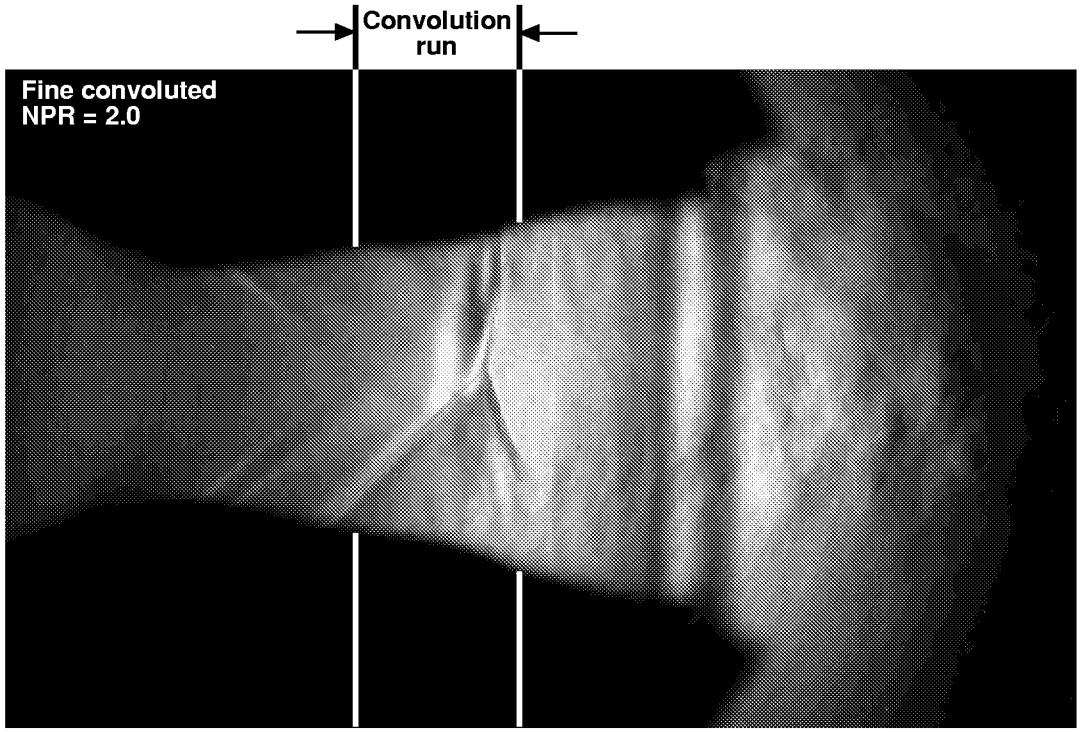

(a) Fine convoluted configuration.

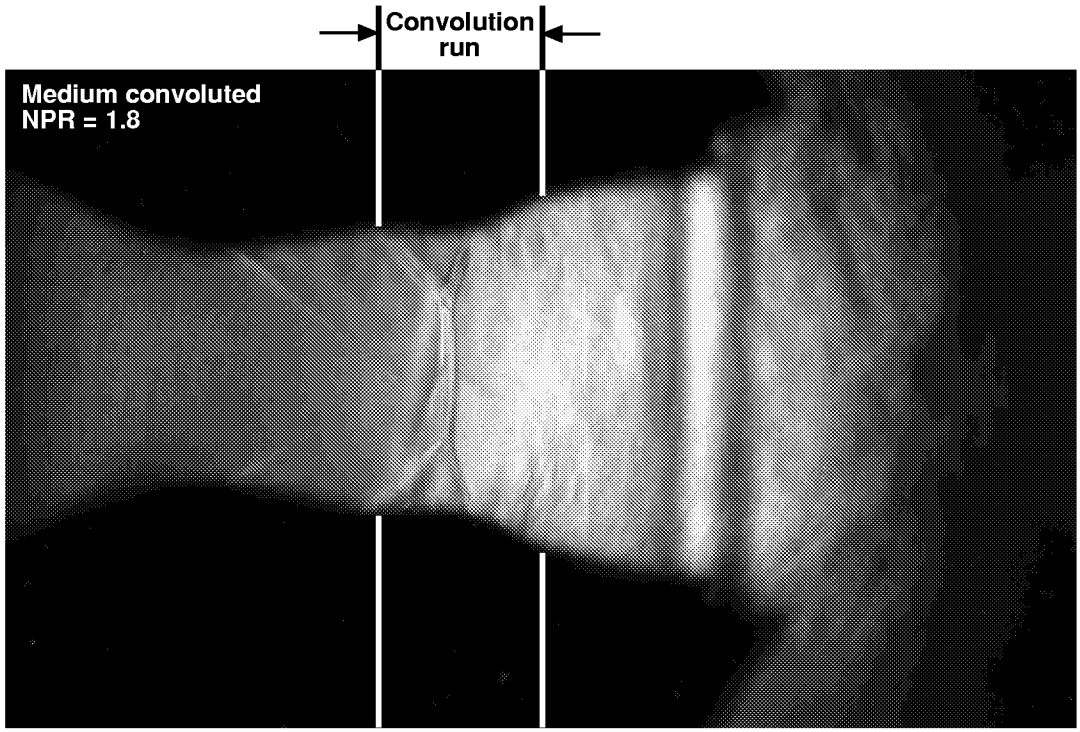

(b) Medium convoluted configuration.

Figure 24. Focusing schlieren flow visualization for convoluted configurations showing nozzle shock upstream of convolution run.

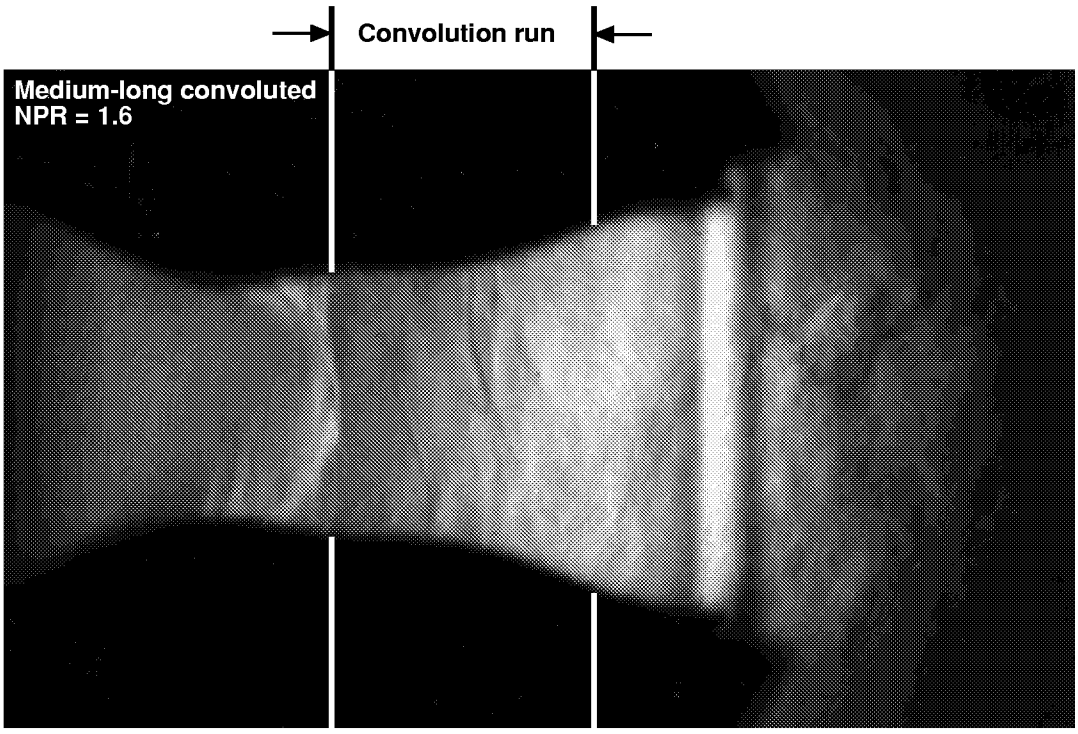

(c) Medium-long convoluted configuration.

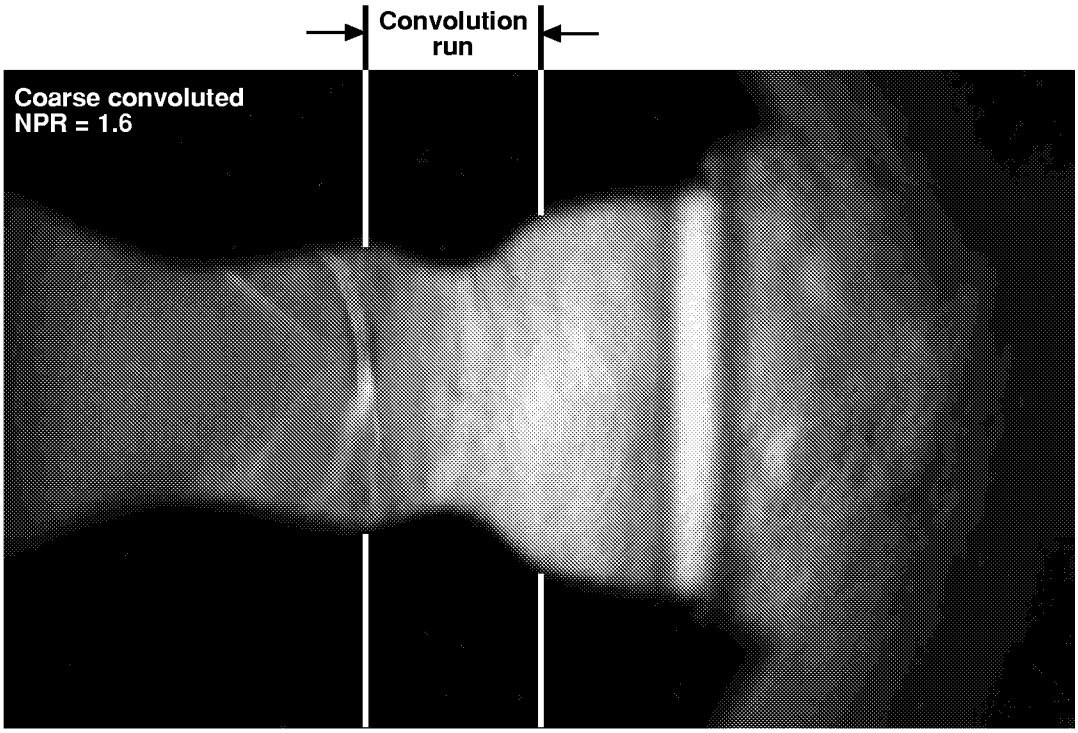

(d) Coarse convoluted configuration.

Figure 24. Concluded.

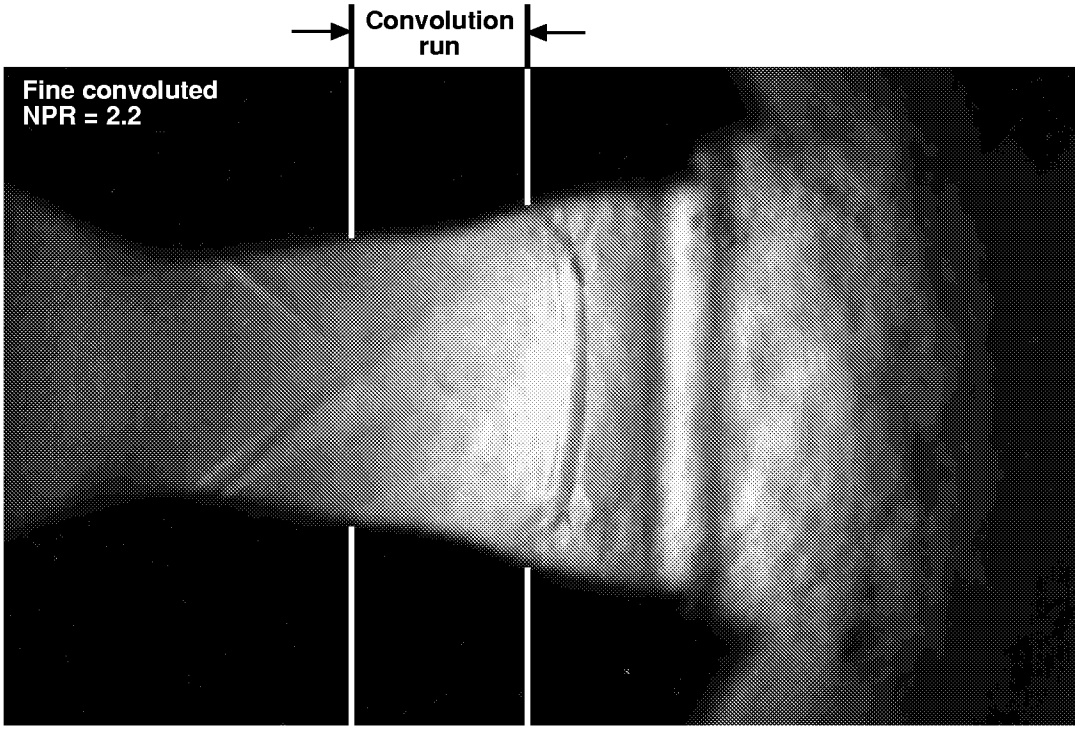

(a) NPR = 2.2.

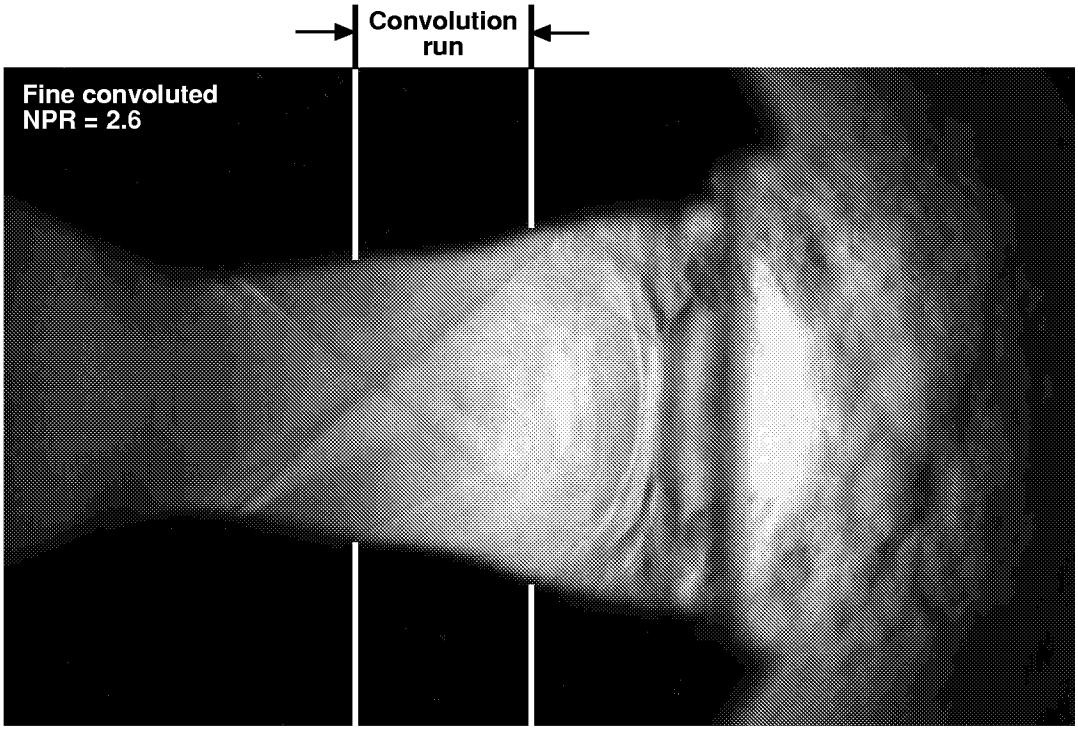

(b) NPR = 2.6.

Figure 25. Focusing schlieren flow visualization at NPRs of 2.2 and 2.6 for the fine convoluted configuration.

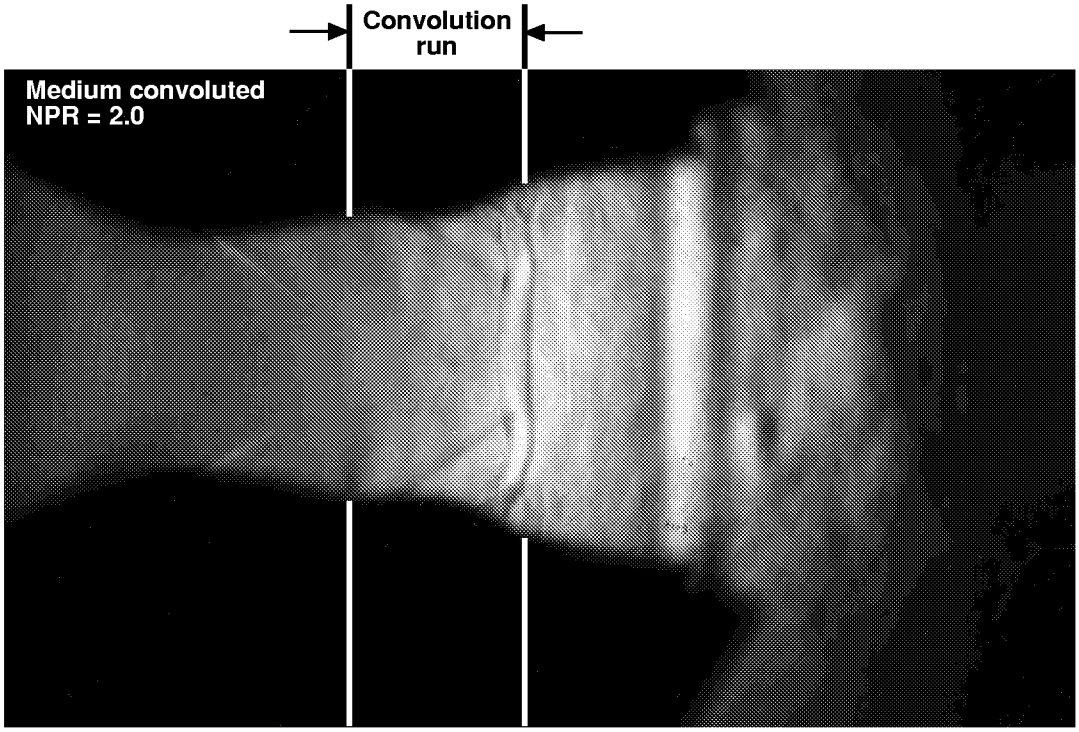

(a) NPR = 2.0.

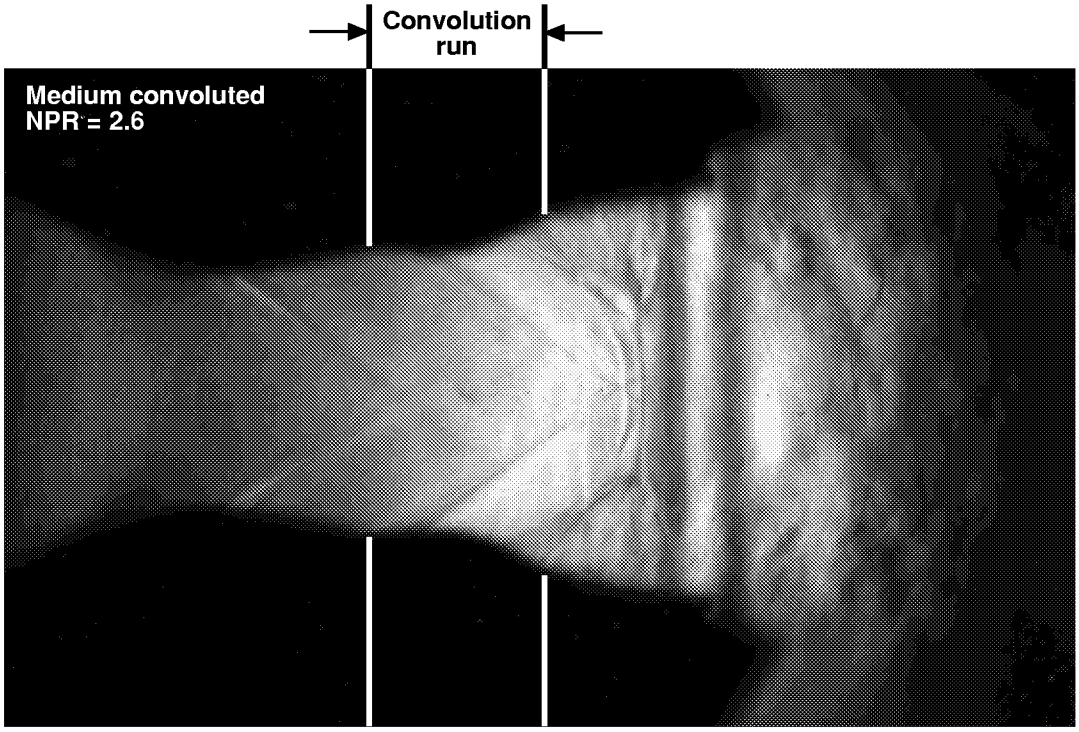

(b) NPR = 2.6.

Figure 26. Focusing schlieren flow visualization at NPRs of 2.0, 2.6, and 3.0 for the medium convoluted configuration.

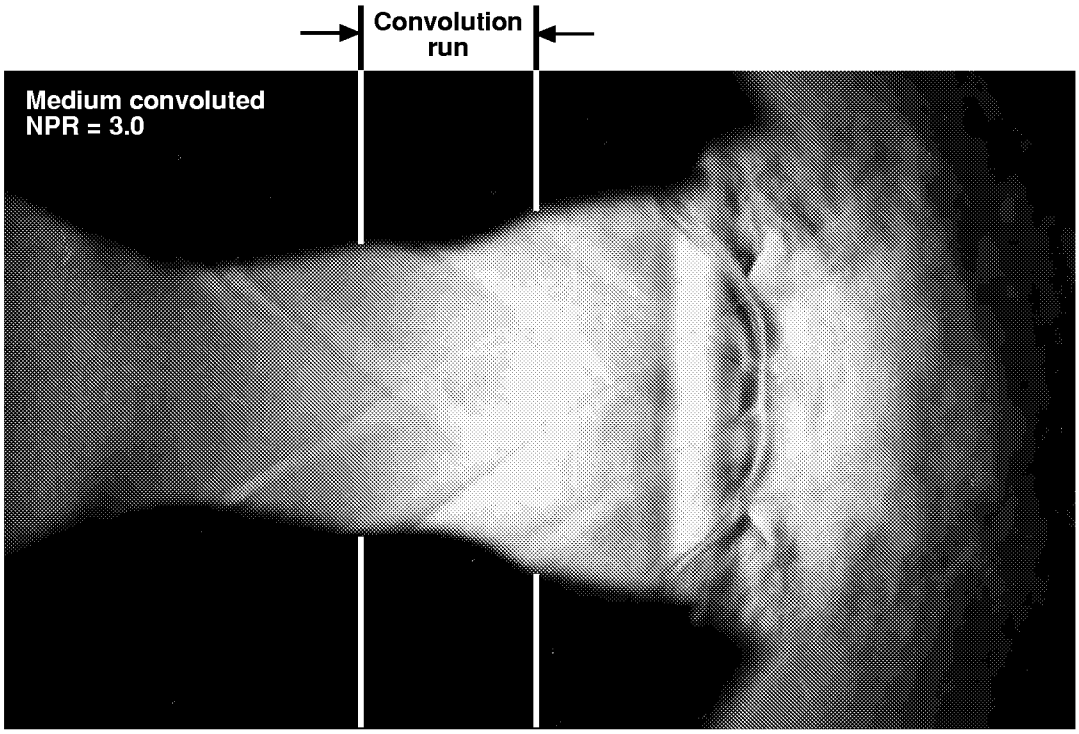

(c) NPR = 3.0.

Figure 26. Concluded.

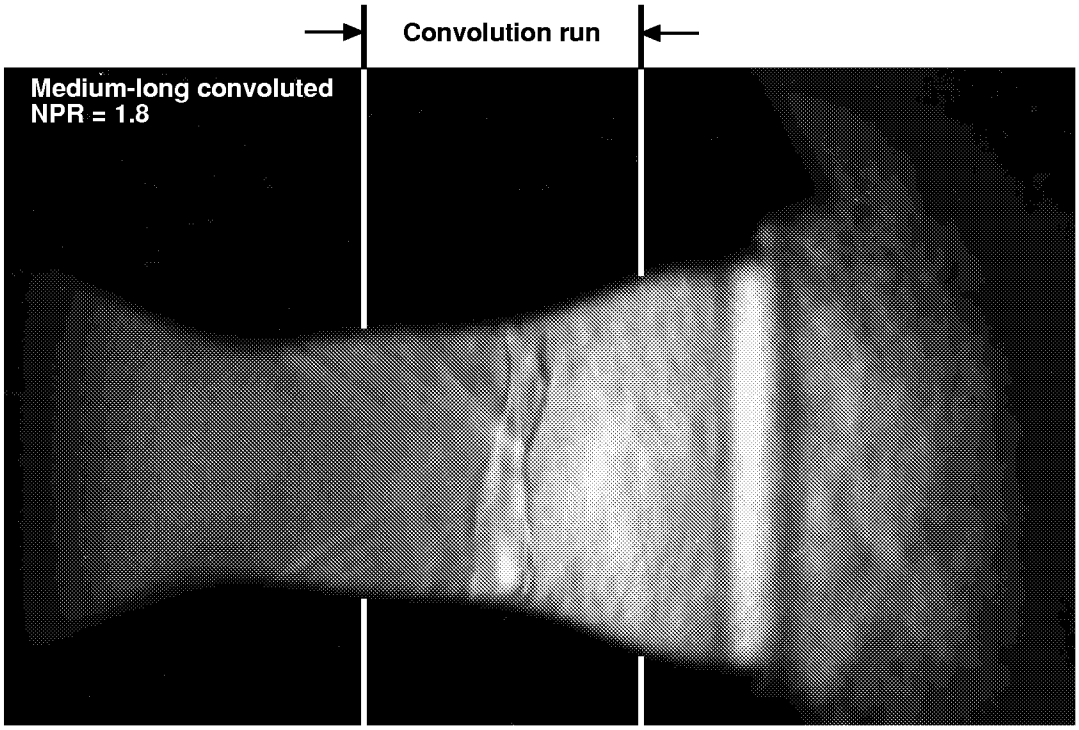

(a) NPR = 1.8.

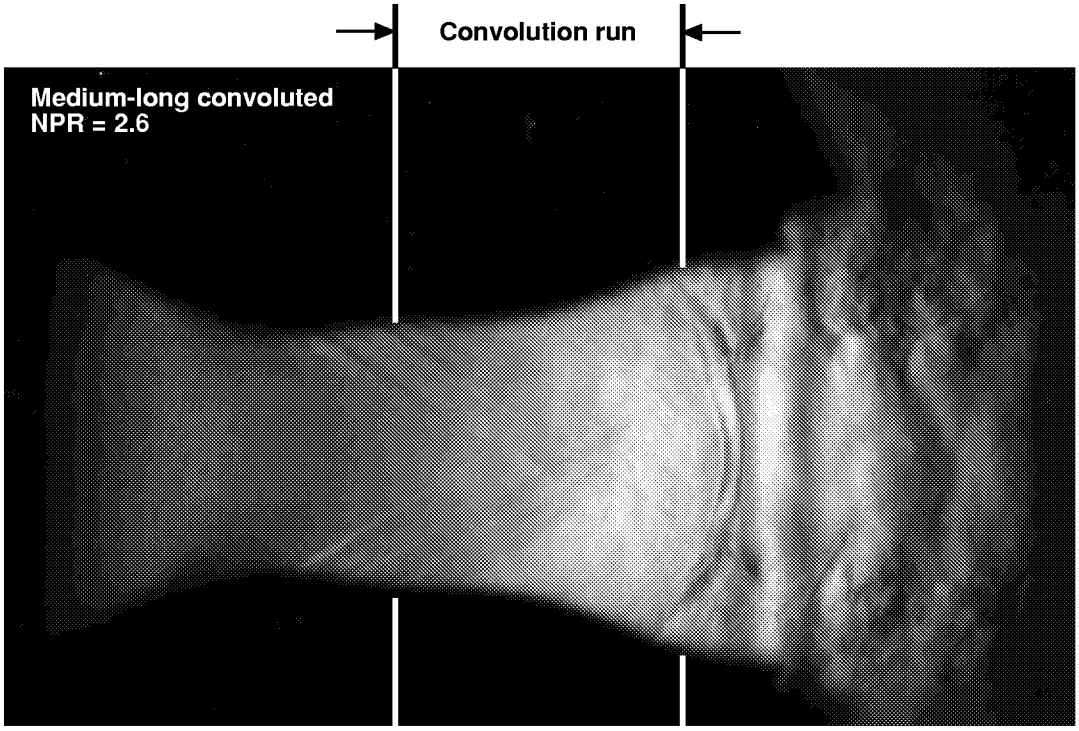

(b) NPR = 2.6.

Figure 27. Focusing schlieren flow visualization at NPRs of 1.8 and 2.6 for the medium-long convoluted configuration.

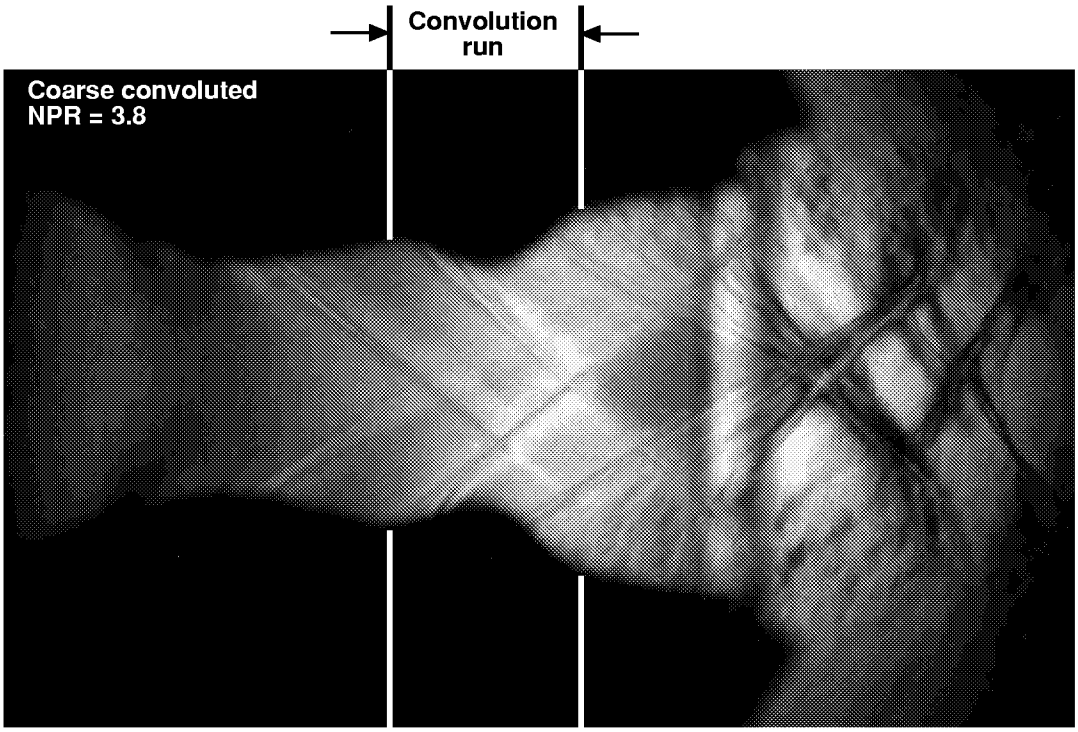

(a) NPR = 3.8.

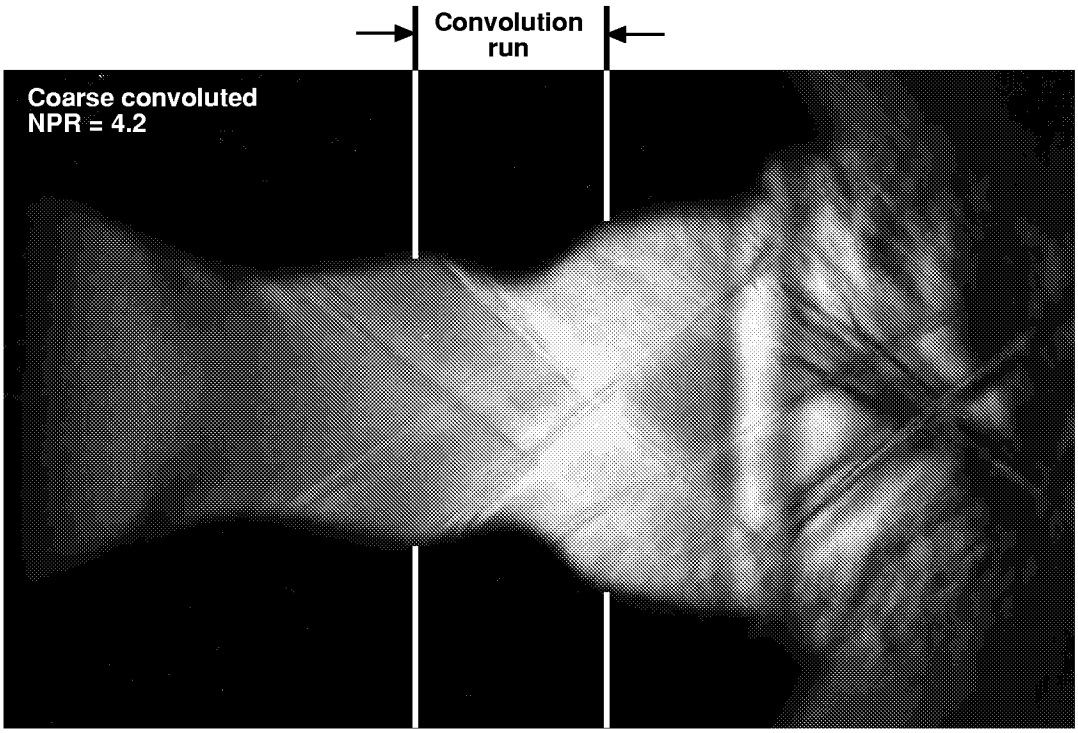

(b) NPR = 4.2.

Figure 28. Focusing schlieren flow visualization at NPRs of 3.8 and 4.2 for the coarse convoluted configuration.

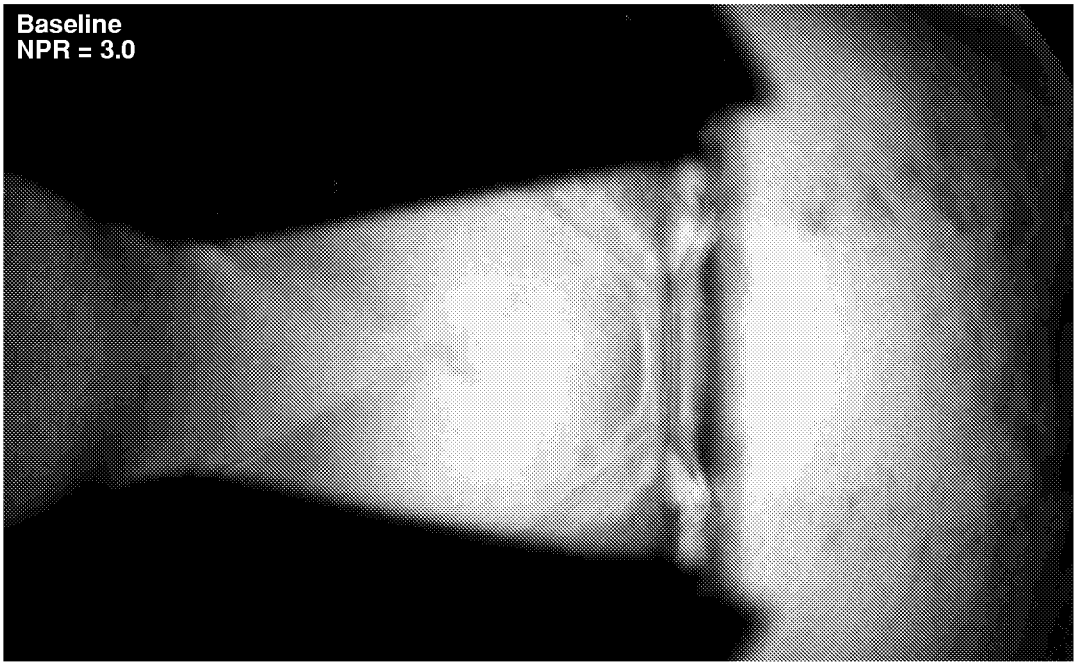

Figure 29. Focusing schlieren flow visualization at NPR = 3.0 for the baseline configuration.

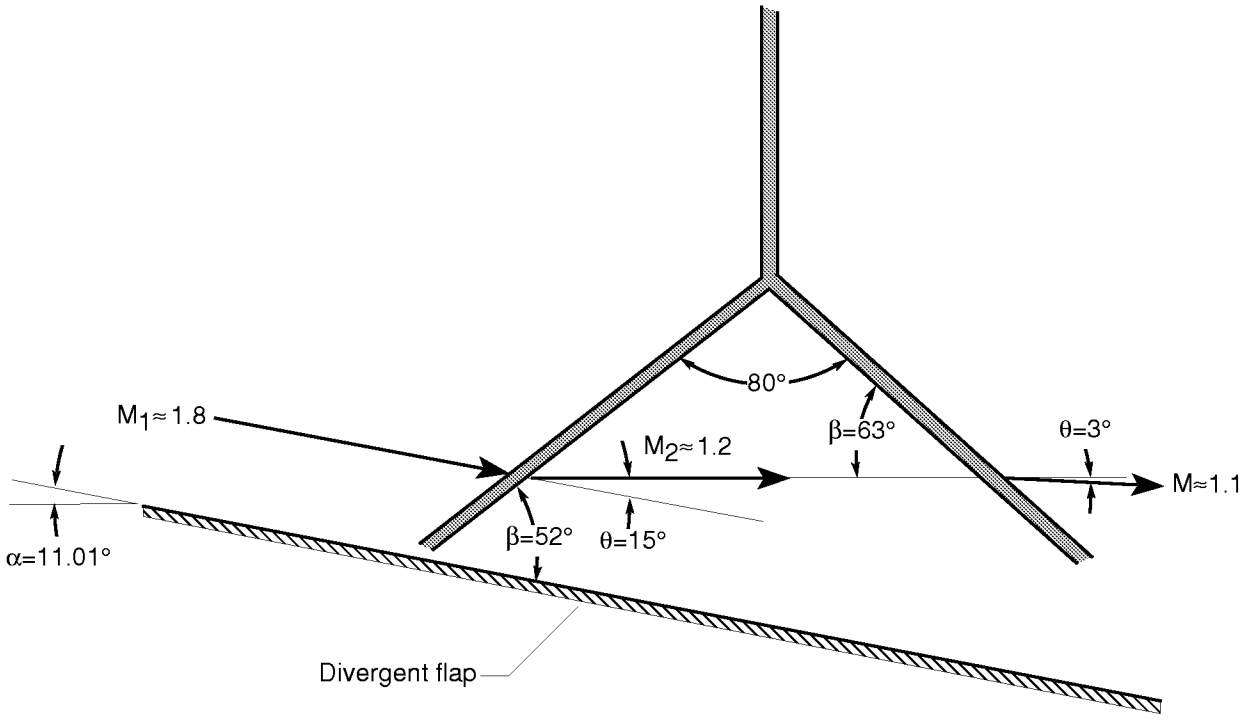

Figure 30. Sketch showing shock-boundary layer interaction lambda foot structure at NPR = 3.0 for the baseline configuration.

REPORT DOCUMENTATION PAGE

Form Approved
OMB No. 0704-0188

1. AGENCY USE ONLY (*Leave blank*)	2. REPORT DATE	3. REPORT TYPE AND DATES COVERED
	February 1999	Technical Publication

4. TITLE AND SUBTITLE
Effects of Convoluted Divergent Flap Contouring on the Performance of a Fixed-Geometry Nonaxisymmetric Exhaust Nozzle

5. FUNDING NUMBERS
WU 538-14-12-01

6. AUTHOR(S)
Scott C. Asbury and Craig A. Hunter

7. PERFORMING ORGANIZATION NAME(S) AND ADDRESS(ES)
NASA Langley Research Center
Hampton, VA 23681-2199

8. PERFORMING ORGANIZATION REPORT NUMBER
L-17696

9. SPONSORING/MONITORING AGENCY NAME(S) AND ADDRESS(ES)
National Aeronautics and Space Administration
Washington, DC 20546-0001

10. SPONSORING/MONITORING AGENCY REPORT NUMBER
NASA/TP-1999-209093

11. SUPPLEMENTARY NOTES

12a. DISTRIBUTION/AVAILABILITY STATEMENT
Unclassified-Unlimited
Subject Category 02 Distribution: Standard
Availability: NASA CASI (301) 621-0390

12b. DISTRIBUTION CODE

13. ABSTRACT *(Maximum 200 words)*

An investigation was conducted in the model preparation area of the Langley 16-Foot Transonic Tunnel to determine the effects of convoluted divergent-flap contouring on the internal performance of a fixed-geometry, nonaxisymmetric, convergent-divergent exhaust nozzle. Testing was conducted at static conditions using a sub-scale nozzle model with one baseline and four convoluted configurations. All tests were conducted with no external flow at nozzle pressure ratios from 1.25 to approximately 9.50. Results indicate that baseline nozzle performance was dominated by unstable, shock-induced, boundary-layer separation at overexpanded conditions. Convoluted configurations were found to significantly reduce, and in some cases totally alleviate separation at overexpanded conditions. This result was attributed to the ability of convoluted contouring to energize and improve the condition of the nozzle boundary layer. Separation alleviation offers potential for installed nozzle aeropropulsive (thrust-minus-drag) performance benefits by reducing drag at forward flight speeds, even though this may reduce nozzle thrust ratio as much as 6.4% at off-design conditions. At on-design conditions, nozzle thrust ratio for the convoluted configurations ranged from 1% to 2.9% below the baseline configuration; this was a result of increased skin friction and oblique shock losses inside the nozzle.

14. SUBJECT TERMS	15. NUMBER OF PAGES
Convoluted Contouring, Exhaust Nozzles, Nonaxisymmetric Nozzles, Nozzles	75
	16. PRICE CODE A04

17. SECURITY CLASSIFICATION OF REPORT	18. SECURITY CLASSIFICATION OF THIS PAGE	19. SECURITY CLASSIFICATION OF ABSTRACT	20. LIMITATION OF ABSTRACT
Unclassified	Unclassified	Unclassified	UL